Optimization and Characterization of Electrospun Untreated and Bio-cleaned Lignin-based Carbon Nanofibers

by

Jiawei Chen

A thesis submitted in partial fulfillment of the requirements for the degree of

Master of Science

Department of Mechanical Engineering

University of Alberta

Abstract

Carbon fibers are reinforcing materials extensively used in composite applications. Since their conventional petroleum-based precursors are high-priced and unsustainable, demand on alternative green precursor has spawned substantial research works on lignin.

This study reports on production and characterization of carbon nanofibers based on untreated lignin (KLA, KLB) and lignin purified with a bio-cleaning process (Bio-KLA, Bio-KLB). Small amounts of PEO were used for improving spinnability of lignin. The production parameters optimized for generating random fibers were electric field, lignin/PEO ratio, and molecular weight of PEO. The electrospinning parameters optimized for aligned fibers were electric field, flow rate, and rotating speed of collector. Spinnability test showed the transformation from uniform fibers to ribbon-like fibers as the total solid concentration increased. At higher total solid concentration, less PEO fraction was required to attain continuous spinning. Increase in lignin fraction embrittled the fiber mats. The optimization was conducted in order to obtain fibers with small diameter and good mechanical properties. Optimal condition for generating random KLA fibers occurred at electric field of 50 kV/m, lignin/PEO ratio of 95/5, and 1000 kDa PEO. Defects were detected when optimal condition was not met. Random KLA and Bio-KLA fibers were thermostabilized and carbonized at this optimal condition. Bio-cleaning improved the properties of random KLA carbon nanofibers by decreasing fiber diameter to 70%, increasing tensile strength by 2.1 times and elastic modulus by 2.7 times. The mechanical properties of random KLA carbon nanofibers achieved at optimal condition were as follows: average fiber diameter of 663.17±64.51 nm, tensile strength of 5.52±4.05 MPa, and elastic modulus of 886.29±471.47 MPa.

Applying optimized solution condition (22 wt% total solid concentration, 95/5 lignin/PEO ratio) for random fibers, electric field of 80 kV/m, flow rate of 440 nl/s, and rotating speed of 2000

rpm were found to be the optimal condition for generating aligned KLA fibers. Some aligned fibers exhibited strong adhesion to aluminum foil, so release agent was used to assist with removal. Release agent posed a risk of weakening the mechanical properties of the fabricated fibers, but it preserved the integrity of the fiber mats for further characterizations. Aligning fibers increased the tensile strength and elastic modulus of KLA fibers by 16.7 times and 10.6 times respectively, compared to random fibers with release agent. Aligned KLA carbon nanofibers possessed average fiber diameter of 697.07±96.41 nm, tensile strength of 23.65±7.70 MPa and elastic modulus of 3960.98±1155.67 MPa.

KLB produced gel-like solution with high viscosity, which was by itself not spinnable. Bio-cleaning converted KLB to spinnable substance. Random Bio-KLB carbon nanofibers showed average fiber diameter of 278.95±49.89 nm, tensile strength of 16.72±5.21 MPa, and elastic modulus of 1532.87±439.63 MPa when using optimal condition for random KLA fibers. Bio-KLB was incapable of producing testable fibers at optimal condition for aligned KLA fibers.

In summary, this work demonstrates the feasibility of using bio-cleaning as a purification method to yield lignin-based carbon fibers. Bio-cleaning and aligning fibers can extensively enhance the mechanical properties of the lignin-based carbon fibers while adopting a greener manufacturing approach.

Preface

The research conducted herein was under the co-supervision of Dr. Cagri Ayranci and Dr. Tian Tang in Department of Mechanical Engineering at University of Alberta. The bio-cleaning of lignin samples and SEM imaging were performed by Dr. Tanushree Ghosh[1] in Chapter 2. Electrospinning in Chapter 2 was a collaborative work conducted by Dr. Ghosh and me. The literature review in Chapter 1, characterization of mechanical properties, DOE analysis, image processing, and data processing in Chapter 2-5 were my original work. A version of Chapter 3 has been published as T. Ghosh, J. Chen, T. Tang, and C. Ayranci, "Bio-cleaning improves mechanical properties of lignin-based carbon fibers," *RSC Advances*, 2020, **10**, 22983-22995. The manuscript compilation was prepared by Dr. Ghosh and me. Chapter 4 and Chapter 5 will be composed into a manuscript for publication.

[1] Dr. Tanushree Ghosh is a post-doctoral fellow working in this project.

Acknowledgement

I would like to express my deepest appreciation towards my supervisors, Dr. Ayranci and Dr. Tang, for their support and advice through my degree. Without their guidance and persistent encouragement for me to continue my study, I would have given up pursuing my academic career long ago. Dr. Ayranci always has a great insight in research and a sense of humor, making the research work delightful, informative, and productive. Dr. Tang is a role model for me. She is patient, professional, highly efficient at work and very considerate for every student. Both of my supervisors have provided me guidance as mentors and friends.

I would express my gratitude towards my parents and friends accompanying me during all my hard times. They make my graduate life diversified and joyful. They are always there when I need them. They really bring out the best in me.

Table of Contents

List of Tables

List of Figures

List of Symbols

SW = Softwood

HW = Hardwood

OL = Organosolv Lignin

SL = Sulfite Lignin

SEL = Steam-exploded Lignin

SDL = Soda Lignin

AL = Alkali Lignin

KL = Kraft Lignin

KLA = Kraft Lignin A

KLB = Kraft Lignin B

Bio-KLA = Bio-cleaned Kraft Lignin A

Bio-KLB = Bio-cleaned Kraft Lignin B

KLA-R = As-spun Random Kraft Lignin A Fibers

KLA-A = As-spun Aligned Kraft Lignin A Fibers

Bio-KLA-R = As-spun Random Bio-cleaned Kraft Lignin A Fibers

Bio-KLA-A = As-spun Aligned Bio-cleaned Kraft Lignin A Fibers

Bio-KLB-R = As-spun Random Kraft Lignin B Fibers

KLA-R-CNF = Carbonized Random Kraft Lignin A Nanofibers

KLA-A-CNF = Carbonized Aligned Kraft Lignin A Nanofibers

Bio-KLA-R-CNF = Carbonized Random Bio-cleaned Kraft Lignin A Nanofibers

Bio-KLA-A-CNF = Carbonized Aligned Bio-cleaned Kraft Lignin A Nanofibers

Bio-KLB-R = Carbonized Random Kraft Lignin B Nanofibers

PEO = Poly(ethylene oxide)

PVA = Polyvinyl Alcohol

DMF = *N,N*-dimethylformamide

CF = Carbon Fiber

Carbon Nanofiber = CNF

PAN = Poly(acrylonitrile)

SEM = Scanning Electron Microscopy

MW = Molecular Weight

F_∞ = Electric Field

$r_{L/P}$ = Lignin/PEO Ratio

W = Molecular Weight of PEO

Q = Flow Rate

Ω = Rotating Speed

D = Fiber Diameter

E = Elastic Modulus

σ = Tensile strength

Subscript a = Actual Value

Subscript c = Coded Value

RT = Room Temperature

RH = Relative Humidity

2FI = Two-Factor-Interaction

ANOVA = Analysis of Variance

DOE = Design of Experiment

CCD = Central Composite Design

CCC = Circumscribed Central Composite

Chapter 1. Introduction

Alternative sustainable precursor for carbon fibers is requisite to replace their conventional eco-unfriendly precursor, reduce the production cost, and still maintain the advanced properties of carbon fibers. The feasibility to use lignin as a carbon fiber precursor via electrospinning is examined in this thesis. Mechanical properties and fiber morphology are characterized to compare untreated and bio-cleaned lignin. An outline of the thesis is summarized below.

Chapter 1 provides a literature review describing the background for this work. Chapter 2 outlines all the experimental works conducted in the research. Chapter 3 summarizes the optimization of the experimental conditions for electrospinning KLA random fibers, preparation of carbon fibers, characterization of the fiber morphology and the mechanical properties, and comparison with Bio-KLA fibers. Chapter 4 describes optimization and characterization results similar to Chapter 3 but for aligned KLA and Bio-KLA fibers. The feasibility of electrospinning random fibers for Bio-KLB is reported in Chapter 5. Chapter 6 presents the conclusion for the research and lists potential future works.

By analyzing the results above, developing low-cost carbon fibers with lignin as precursor is demonstrated to be achievable. Economically viable lignin increases renewability of end product, broadens industrial demand and market supply of carbon fibers. One of the disadvantages of lignin-based carbon fiber is its feeble mechanical properties. Purification of lignin by bio-cleaning is a promising method to enhance the mechanical properties. Together, this work demonstrates enormous potential of bio-cleaned lignin as alternative carbon fiber precursor.

1.1. Carbon Fiber

Carbon fibers (CFs) contribute imperatively to the evolution of advanced structural materials. In applications requiring great fatigue resistance, high stiffness and strength-to-weight ratio, CF is an auspicious candidate reinforcing material. CFs were first fabricated unwittingly as filaments for light bulb by Thomas Edison[1,2]. Conventional commercial CFs are anisotropic fibers consisting of more than 92 wt% carbon. They possess both crystalline and amorphous regions. Crystalline regions are composed of stacked carbon layers with crystallites mostly aligned towards the fiber axis, leading to higher longitudinal modulus than transverse modulus. Amorphous domains include disordered carbon layers[3].

CFs can be categorized into various grades, in terms of tensile strength: low-strength (~1.0 GPa)[4], high-strength (>3.0 GPa), ultrahigh-strength (>4.5 GPa)[5]; and in terms of elastic modulus:

low-modulus (<100 GPa), intermediate-modulus (200-350 GPa), high-modulus (350-450 GPa), and ultrahigh-modulus (>450 GPa)[6]. Low tensile strength and elastic modulus correspond to general purpose (GP) grade, while high tensile strength and elastic modulus belong to high performance (HP) grade[4]. Their high mechanical properties, electrical conductivity, low thermal expansion coefficient, and high thermal conductivity make them widely applicable in aerospace, construction, electronics, robotics, and thermal control[7]. The annual demand for CFs is expected to increase from 46,000 tons to 140,000 tons worldwide with a threefold increase in sales revenue from 2011 to 2020[8].

Carbon nanofibers (CNFs), synthesized with diameter in the submicron to nanoscale range (<1 µm)[9], have drawn rapidly growing research interest for their large surface area and high aspect ratio. These features provide them unique properties suitable for broader applications, such as filtration, drug delivery, catalyst, wound dressing, and tissue scaffolds[10].

1.2. Carbon Fiber Precursor

Various applications demand the properties of CFs to be tailorable. One of the predominant factors influencing the properties of CFs is the precursor material. CFs can be fabricated from various precursors, including but not limited to poly(acrylonitrile) (PAN), rayon, coal-based or petroleum-based pitch, acrylic[11], and lignin. Some are exploited for their good mechanical properties, high carbon content, or highly oriented molecular structures. Some are acknowledged for their degradability or reusability. The common precursors for CFs or CNFs are summarized below.

1.2.1. PAN

PAN is one of the most prevalent CF precursors because of its high carbon content and high molecular weight (MW). In the global CF market, 90% of CF precursors are PAN-based[12]. PAN-based precursors produce commercial CFs with different grades. For instance, commercial PAN-based CFs produced from Toray Industries feature adjustable mechanical performance, ranging from TORAYCA T300G (GP grade) with tensile strength of 3.6 GPa and elastic modulus of 230 GPa, to TORAYCA T1100G (HP grade) with tensile strength of 6.6 GPa and elastic modulus of 324 GPa[13,14]. However, fabrication of CNFs with high properties was challenging. Zussman et al. fabricated highly oriented PAN-based CNFs at carbonization temperature of 250-1100 °C with diameter of 50-250 nm, bending modulus of 63±7 GPa, and 63% failure rate at strength of 0.64 GPa[15]. The authors ascribed mechanical properties lower than commercial CFs to

the lack of optimization and copolymer. Arshad et al. improved the fabrication process and yielded PAN-based CNFs with diameter of 150-500 nm, tensile strength of 3.5±0.6 GPa, and elastic modulus of 172±40 GPa at carbonization temperature of 1400 °C[16]. Further increase in carbonization temperature improved elastic modulus of the resulted CNFs, but showed reduction in tensile strength. Even though mechanical properties of PAN-based CFs or CNFs were high, more than 50% of PAN-based CF cost was precursor cost (Figure 1.1). Cost of PAN-based CF is around $15-30/kg[17,18], highly sensitive to oil price. Fossil-based PAN generates a host of environmental concerns. Therefore, replacement materials should be considered to address these issues.

PAN-based CF Cost

■ Precursor Fiber ■ Stabilization
■ Carbonization ■ Post-treatment
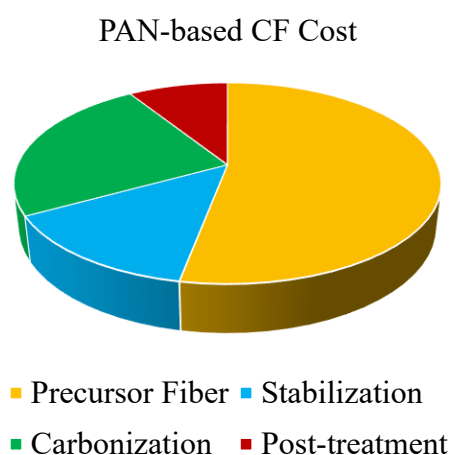
Figure 1.1. Chart illustration of PAN-based CF cost breakdown[19].

1.2.2. Pitch

Pitch can be produced from petroleum residue or coal tar. Infusible composition within pitch originated from coal tar impedes its spinnability and its low softening point causes fiber stabilization to be challenging if no purification or treatment is adopted[20]. CFs from petroleum-based pitch are more favored as they possess higher carbon yield[21]. Pitch can be classified into anisotropic or isotropic pitch[5]. Mesophase pitch is mainly anisotropic with high MW, synthesized by heat treatment[22]. CFs from mesophase petroleum-based pitch contain more homogenous structure, while PAN-based CFs show more oriented crystallites at the fiber surface (skin)[23]. Due to their structural differences, mesophase pitch precursor generally yields CFs with higher thermal conductivity[7], higher elastic modulus, but lower tensile strength. Ko et al. managed to produce pitch-based CFs at 1700 °C with tensile strength of 2.1 GPa, elastic modulus of 212 GPa, and diameter of ~11 μm[24]. The commercial pitch-based CFs feature tailorable properties including low

to ultrahigh elastic modulus (41-940 GPa), high ductility (2.82%), and low to high tensile strength values (1.10-3.46 GPa)[25]. However, cost of pitch-based CF ($22-90/kg) is even higher than PAN-based CF, especially for mesophase pitch[3]. Exploring low-cost alternative is essential for CF production.

1.2.3. Natural Sources

PAN and pitch-based CFs exhibit superior mechanical properties. However, they are expensive and nonrenewable polymers (i.e. petroleum based), resulting in growing environmental and economic concerns for CF production[26]. Recent studies addressing these drawbacks have focused on either developing chemical techniques to recycle CFs[27], or exploring inexpensive biodegradable alternatives for precursor materials[26,28]. Rayon (cellulose fiber) was employed to fabricate CFs, but their mechanical properties were much poorer than PAN or pitch based CFs[29]. Rayon-based CFs were first patented in 1973[30]. After graphitized at 2800 °C, fabricated rayon-based graphite fibers showed tensile strength of ~1 GPa and elastic modulus of ~160 GPa[30]. Cellulosic fibers require substantial stretching and heat treatment at high temperature. Later studies also reported tensile strength of 0.6-2.8 GPa and elastic modulus of 33-710 GPa for rayon-based graphite fibers[22,29]. But high cost (~£ 1000/kg or ~$1400/kg) of rayon based CFs due to expensive heat treatment and stretching process reduces market demand of rayon-based CFs[31].

Another commercial cellulose fibers, Lyocell, show improvement in mechanical properties with tensile strength almost doubling that of rayon-based CFs[32]. However, the commercial production of cellulose-based CFs is limited due to their insufficient mechanical properties for aerospace or automotive applications. Another natural source, lignin, has been proposed as an alternative CF precursor. Its low-cost and renewability facilitate sustainable industrial production of CFs at reduced price.

1.3. Lignin

Lignin is a renewable amorphous biopolymer mainly encompassing cross-linked phenylpropanoid units of *p*-hydroxyphenyl (H), guaiacyl (G) and syringyl (S). These three units correspond to monolignols of *p*-coumaryl alcohol, coniferyl alcohol, and sinapyl alcohol (Figure 1.2) respectively[33]. Lignin is the second most abundant biomass in nature, transcended only by cellulose. It was first introduced in 1960s as the precursor for CFs by dry and wet spinning[34]. Extraction of lignin can be conducted by recovering black liquor, a byproduct from pulp and paper mills, since lignin causes coloration and negative impacts on the quality of the products. Removal

of lignin can increase the overall pulping production[35]. Lignin can either be recycled as fuel or used for other applications, such as adhesive, resin or CF precursor[36]. As a byproduct, lignin can significantly reduce the manufacturing cost of CFs since majority of CF production cost is on the precursor. Its advantages in low-cost and sustainability are accompanied by sacrifice in mechanical properties of CFs. Researchers have attempted to enhance the mechanical properties of lignin-based CFs by experimenting on sources of lignin[37], improving lignin purity, and optimizing manufacturing process. The sources of lignin include softwood (SW), hardwood (HW), and grass. Softwood lignin is predominantly constituted of G units. Hardwood lignin contains mostly S and G units. Grass lignin generally consists of H units[38,39]. Based on sulfur contents, lignin can be divided into sulfur-free lignin and sulfur-containing lignin. Sulfur-free lignin includes organosolv lignin (OL), steam exploded lignin (SEL) and soda lignin (SDL), whereas common sulfur-containing lignin is kraft lignin (KL) and sulfite lignin (SL)[40]. These classifications of lignin depend on the pulping processes where lignin is extracted.
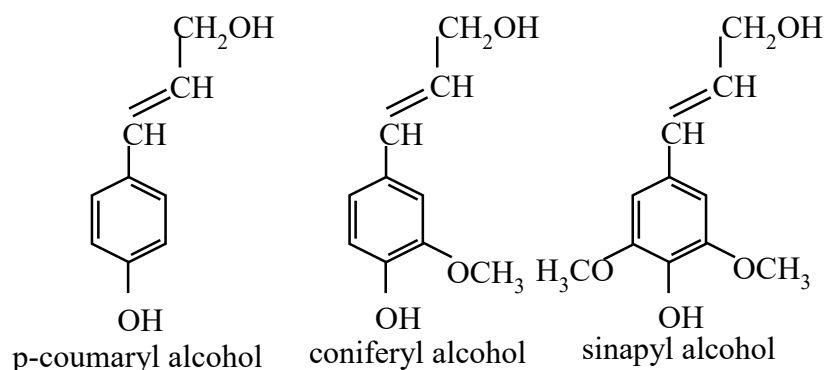
Figure 1.2. Structures of common monolignols[33].

1.3.1. Organosolv Lignin

OL is extracted from organosolv pulp where organic solvent is used as cooking liquor to treat wood chips. Distilled water is typically used to retrieve lignin after organic acid solvent solubilizes it. Common organic acids for organosolv process include formic acid and acetic acid[36]. Watkins et al. used a mixture of organic acids to extract lignin from different sources[41]. They concluded that after treatment with organosolv process, high lignin yield was achieved from alfafa while lignin with high thermal stability was attained from wheat straw. Xu et al. also reported use of hydrochloric acid as the catalyst, where better isolation of lignin from wheat straw was achieved using organic acids than organic alcohols like methanol and ethanol[42]. Alcell, a type of organosolv process, employs aqueous ethanol to extract lignin. Lallave et al. managed to electrospin hollow

fibers from Alcell lignin for CNFs with co-axial and tri-axial spinneret[43]. Oroumei et al. also fabricated CNFs from hardwood organosolv lignin (HW-OL) with PAN as the binder[44]. Even though MW of HW-OL was low, it produced fibers with average diameter of 61-2277 nm prior to carbonization and higher carbon yield (49-70%) than PAN-based CNFs (37%).

1.3.2. Sulfite Lignin

Sulfite pulping process treats wood chips via ion exchange with bisulfite ions[45]. SL, or Lignosulfonate salt, is extracted from sulfite process and is water-soluble. Yen and Chang optimized the manufacturing parameters for hardwood sulfite lignin (HW-SL) to produce CNFs with average diameter of 292 nm and low carbon yield (<10%)[46]. Xia et al. achieved CFs with decent mechanical properties by esterification of SL and co-polymerization with Acrylonitrile[47]. The fabricated CFs possessed average fiber diameter of 12 μm and tensile strength of 1100 MPa. Even though their mechanical properties were lower than commercial PAN-based CFs, they demonstrated the feasibility of obtaining lignin-based CFs with high tensile strength.

1.3.3. Steam-exploded Lignin

Steam explosion is another pulping process requiring significant amount of energy. It steams wood to ~200 °C and subsequently decompresses acceleratedly to blast treated wood into fibers[48]. Organic alcohols like ethanol or methanol are generally used to isolate lignin since they can achieve higher yield than acid recovery. As the process involves low amount of chemicals, SEL is considered as an environment-friendly product with lignin purity of 85.3%[49]. Sudo and Shimizu modified SEL via hydrogenation followed by extraction to discard compounds with low MW[48]. They manufactured general grade CFs from SEL by melt spinning. The SEL-based CFs had diameter of 7.6±2.7 μm, tensile strength of 660±230 MPa, and elastic modulus of 40.7±6.3 GPa.

1.3.4. Soda Lignin

SDL is separated from soda pulping process, which uses sodium hydroxide as cooking liquor. SDL has high purity (~2 wt% ash) and high thermal stability[50]. SDL can be used to fabricate carbon sheet for high-capacity batteries[51]. Awal and Sain melt-spun hardwood soda lignin (HW-SDL) into CFs with good mechanical properties and characterized rheological properties of SDL[52]. They reported that SDL solution exhibited non-Newtonian feature and shear-thinning. To further improve the mechanical properties, Zhang et al. mixed SDL with PAN at a ratio of 1/0.25 (PAN/lignin)[53]. CNFs fabricated from the blend exhibited improved mechanical properties with

higher ductility than CNFs from pure PAN. The SDL/PAN-based CNFs showed average diameter of 177 nm, tensile strength of 142±8 MPa, and elastic modulus of 10.0±0.4 GPa.

1.3.5. Kraft Lignin (KL)

As a prevalent pulping process in papermaking industry, kraft process produces wood pulps using sodium hydroxide and sodium sulfide. Over 65 million tons softwood kraft pulps are produced annually[54]. Softwood kraft lignin (SW-KL) is typically preferred over hardwood kraft lignin (HW-KL) for its higher reactivity and more uniform structure[54]. CFs from SW-KL were patented in 2010, where SW-KL underwent filtration, acid precipitation at 80 °C and acetylation to become spinnable and thermally stabilizable[55]. In solvent like *N,N*-dimethylformamide (DMF), KL is in spherical form[56]. Using DMF as solvent, organic-fractionated SW-KL exhibits shape memory behavior to moisture after thermostabilization[57].

Alkali lignin (AL) refers to either SDL or KL. Different types of lignin, including acid OL, ethanol OL, and AL were compared in a study[58]. Ethanol OL could not maintain fiber form after carbonization. AL-based CFs showed tensile strength of 15.58±2.10 MPa and elastic modulus of 24.54±3.29 GPa. Mechanical properties, yield of carbonization (41.60%), and carbon content (98.41%) of AL-based CFs surpassed acid OL-based CFs.

1.4. Purification of Lignin

On account of lignin's heterogeneous structure, limitations are posted on current methods to remove impurities in lignin, such as ash, sulfur, cellulose, hemicellulose, etc. These contaminations originate from extraction of black liquor. Impurities cause uneven distribution of carbon atoms and formation of localized heterogeneous structures such as voids in lignin-based CFs[59]. As such, the impurities introduce defects in lignin-based CFs and negatively influence the mechanical properties. Lignin with high MW and high purity is desirable to the fabrication process for CFs. Purification can be achieved through acid treatment[60], filtration[61], fractional separation with organic solvents[62], and biodegradation without compromising the structure of lignin[63]. Depending on sources and types of lignin, different purification methods need to be adopted.

1.4.1. Acid Treatment

Acid treatment is a prevailing purification method for AL. Acid treatment involves addition of mineral acids like sulfuric acid (H_2SO_4)[64,65] and hydrochloride acid (HCl)[66], carbon dioxide (CO_2)[67], or a mixture of organic acid and ionic liquids[68] to precipitate lignin from the solution. For CO_2 treatment, it can only reduce pH level to ~10 and precipitation of lignin is low. It is normally

used to alleviate the amount of strong acids used in the treatment. For mineral acids treatment, HCl can achieve lignin with higher MW[69], but H_2SO_4 is typically favored over HCl due to lower cost[70]. Acid participation is followed by filtration and DI water washing. DI water increases purity of lignin but induces lower lignin yield since small amount of lignin is water-soluble. Gilarranz et al. reported that precipitation of silica occurred first during acid treatment of SDL[70]. Suspended impurities and silica could be removed via centrifugation. As pH further dropped, lignin precipitated from the solution. Garcia et al. investigated the properties of SDL when adding H_2SO_4 to reduce pH from 12.64 to 0.72[64]. MW of SDL (3501 Da) at pH of 0.72 was similar to commercial AL (MW 3135 Da). At pH higher than 2.57, substantial amount of impurities like silicate and hemicellulose remained.

1.4.2. Membrane Filtration

Microfiltration, ultrafiltration, and nanofiltration are membrane separation techniques with pore size in the scale of 10^{-1} μm, 10^{-2} μm, and 10^{-3} μm respectively to isolate lignin based on MW. Ziesig et al. utilized microfiltration and ultrafiltration to achieve highly-purified lignin with reduced carbohydrate and inorganic contents, but also lower lignin yield[71]. Toledano et al. included microfiltration, ultrafiltration, nanofiltration, and reverse osmosis to purify lignin. The authors demonstrated processes up to the stage of ultrafiltration were enough to remove the impurities and yield lignin MW of 3544 Da[61]. Jonsson et al. employed ultrafiltration and nanofiltration to isolate KL from both HW and SW kraft pulp black liquor by selective removal of fractions with low molecular size[72]. Carbohydrates, ash, and lignin with low MW were extracted by sequential purification procedures at elevated temperature. Ultrafiltration and nanofiltration produced lignin yield of 75% from original black liquor with significant decrease in hemicellulose content.

1.4.3. Biodegradation

Biodegradation is defined as the decomposition of compounds using microorganism. Biodegradation is a green method to purify lignin with minimal environment contamination. It is less efficient than other purification methods and more challenging to control due to inconsistent microbial growth. However, its non-engagement in chemical reaction and diversity of microorganisms make biodegradation a prominent purification method for research. A comparison of microorganisms, including bacteria, fungi, and laccase enzyme, was conducted on their ability to degrade KL[73]. After 54 days of incubation, substantial mineralization of lignin was achieved by fungi. Bacteria managed degradation of lignin. Oxidative cross-linked repolymerization of lignin

occurred for enzyme treatment rather than depolymerization. The ineffective enzymatic depolymerization caused by heterogeneous structure of lignin was also captured by Reid[74]. His paper further identified two categories of fungi, white-rot and brown-rot. White-rot fungi could break down and mineralize lignin, while brown-rot fungi were capable of extracting carbohydrates and leaving most lignin structure intact.

1.4.4. Fractionation

Fractionation is the separation of lignin with particular MW from black liquor. Membrane filtration, organosolv treatment, acid treatment, biodegradation can all achieve fractionation of lignin. These treatments can be used in sequence to yield lignin with specific purity or properties. For instance, a two-step fractionation of acid treatment (H_2SO_4) and organosolv process (ethanol) could obtain lignin with MW of ~2060 Da from oil palm trunk fiber pulping[75]. Li et al. fractionated water-insoluble lignin by biodegradation (enzyme treatment) and membrane filtration to obtain lignin fraction with high MW (~20000 Da) and more uniform molecular structure. High MW increased crystallinity and enhanced the mechanical properties of the fabricated CFs. The elastic modulus of lignin-based CFs was 21.7 GPa, higher than PAN-based CFs (20.6 GPa) manufactured under the same condition[76].

1.4.5. LignoBoost®/LignoForce System™

Conventional KL extraction occasionally encounters plugging in filtration. To address this issue, LignoBoost, a well-developed industrial lignin extraction method, is widely used for higher lignin yield, less sulfur content, low ash and carbohydrate content[77]. Instead of performing DI water washing right after acid treatment and filtration, KL solid is re-submerged in liquid. Further acid treatment with H_2SO_4 is applied, followed by filtration and washing. Recycling KL to re-participate in the LignoBoost process loop can mitigate loss of lignin. LignoForce is another industrial process based on traditional KL recovery[78]. It inserts an additional step of oxidation before acid treatment to increase the filterability of KL and have a pronounced effect on reducing sulfur content.

1.5. Fiber Production Methods

Various fiber spinning techniques are utilized to convert lignin or other precursors into fibers prior to the formation of CFs. These techniques can be sorted into wet spinning[79], dry spinning[80], dry jet wet spinning[81], melt spinning[82], and electrospinning[83–85]. Majority of these techniques are well established techniques in the centuries of old textile industry.

1.5.1. Dry Spinning

Dry spinning (Figure 1.3a) has been an industrial approach to fabricate fibers for almost a century[86]. It is also called solvent spinning, since it only involves extrusion of solution under convective environment. Dry-spun acetylated SKL fibers for CFs preparation were experimented by Zhang and Ogale[80]. Acetylation of SKL at low amount increased the spinnability without inducing thermal fusion in carbonization. Acetylated SKL was dissolved in acetone and extruded into filaments in flowing air. As solvent evaporated, lignin fibers extruded from dry-spinning exhibited non-circular cross-sections at the operating temperature of 25-50 °C. The presence of notches resulted in defects in the structure of CFs but increased the surface area at the same time. The carbonized dry-spun SKL showed fiber diameter of approximately 7 μm, tensile strength of 0.79-1.06 GPa and elastic modulus of 50-52 GPa[80,87]. Dry spinning yields lignin-based CFs with decent mechanical properties, but it requires post-spinning stretching, recycling of solvent at industrial scale, achieves fibers with large average diameter and unsmooth surface[87].

1.5.2. Wet Spinning

Similar to dry spinning, wet spinning (Figure 1.3b) undergoes dissolution in solvent and fiber extrusion. Rather than solvent evaporation in air, the extruded solvent goes through a coagulation bath with solvent and water. Diffusion of solvent from jet to coagulation bath and water from bath to jet solidify the fibers. Using wet spinning, Jin and Ogale spun a mixture of SKL and PAN through coagulation bath at 80 °C. Fibers were elongated again in water bath. The wet-spun fibers showed reduced sharp notch than fibers obtained from dry spinning. Tensile strength, elastic modulus, and average fiber diameter of the resulted CFs were 1.2±0.1 GPa,130±3 GPa, and ~7 μm respectively[88]. Hollow fibers can also be produced from wet-spinning by changing the concentration of solvent or chemicals in coagulation bath to control solvent diffusion[89]. In comparison to dry spinning, wet spinning does not require elevated temperature for rapid drying. However, it is challenging to produce void-free fibers via wet spinning. Most researches were conducted on wet spinning of lignin/PAN blend and limited researches were found on pure lignin.

1.5.3. Dry Jet Wet Spinning

Dry jet wet spinning (Figure 1.3c) is a combined process of dry and wet spinning. There is an air gap between the extruded jet and the coagulation bath. The air gap needs to be optimized for different precursors[90]. Mixture of KL and cellulose could produce CFs with tensile strength of 780 MPa and elastic modulus of 68 GPa via dry jet wet spinning process[91].

1.5.4. Melt Spinning

Melt spinning (Figure 1.3d) is an inexpensive fiber spinning method. The polymer is melted and fed through rollers to spin into fibers. The rheological characteristics of the polymer determine its spinnability. Nordstrom et al. discovered SKL permeate after ultrafiltration could be melt-spun continuously into fibers for production of CFs[82]. SKL could not be extruded as it caused foaming in melt spinning. This problematic situation was alleviated by re-extrusion to discard volatile compositions in first extrusion. However, SW-KL was incapable of being melt spun into uniform fibers. The authors reported adding HW-KL permeate as a softening substance could make SKL spinnable[82]. Baker et al. also encountered the obstacle that HW-KL was foaming during melt spinning. However, HW-OL yielded smooth fibers after melt-spinning, and subsequently carbonized into CFs. Obtained CFs had average fiber diameter of 11 μm, tensile strength of 0.51 GPa, and elastic modulus of 28.6 GPa[92]. Melt spinning does not require solvent but its heat control is challenging.

1.5.5. Electrospinning

Electrospinning (Figure 1.3e) is a versatile process to fabricate fibers with submicron to nanoscale diameters. It generates a jet of polymer solution from a spinneret to a collector by applying a high voltage electric field to the apparatus. The voltage causes the solutions to overcome the surface tension and form Taylor cone at the nozzle[93]. As the solvent evaporates, the elongated solution whips due to jet instability. The jet solidifies as ultrafine fibers at the collector. The mechanism of electrospinning is a balance between surface tension and electrostatic force. If the electric field and Coulomb repulsive force do not surpass surface tension, the jet form of the solution cannot be maintained. Three stages of jet instabilities, Rayleigh instability, bending instability, and whipping instability, are affected by different parameters, such as surface tension of solution, electric field, and net charge density[94]. In the research conducted by Teng et al., fractionated SKL could yield CNFs with diameter of 639±75 nm, tensile strength of 45.03±9.93 MPa, and elastic modulus of 6238.35±1307.74 MPa[95]. Most lignin-based CNFs from electrospinning may acquire poorer mechanical properties than CFs produced from other spinning methods. However, fine fiber diameter achieved in electrospinning and the ability to control the end product via various processing parameters demonstrate the research potential of electrospinning. With further analysis into process optimization, properties of lignin, binding

polymer, and solvent, it is plausible to yield electrospun lignin-based CNFs with improved mechanical properties.
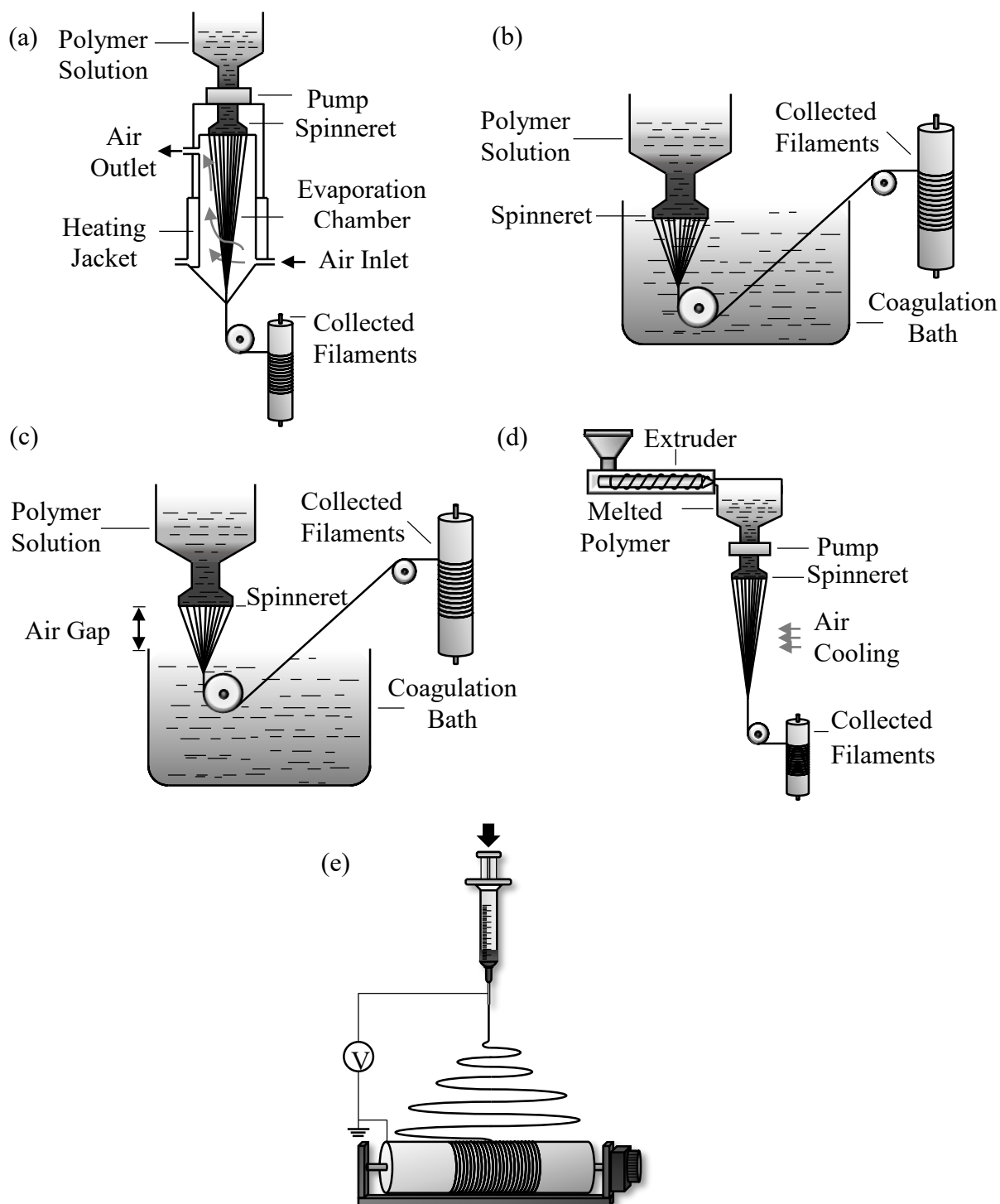
Figure 1.3. Schematic of (a) drying spinning, (b) wet spinning, (c) dry jet wet spinning, (d) melt spinning, and (e) electrospinning with rotating drum.

1.6. Electrospinning Setups

Electrospinning is adopted in this thesis since it provides great control over the fabricated fibers. Versatile electrospinning setups offer adjustable properties of produced fibers. Different types of electrospinning setups are shown below for both random and aligned fibers.

1.6.1. Random

Stationary collector is employed for depositing random fibers. Some setups for fabricating random fibers are summarized in Table 1.1.

1.6.2. Aligned

Aligned fibers normally provoke more research interest since aligning fibers renders more oriented molecular chains and enhanced mechanical properties. The electrospinning setups for aligned fibers are shown in Table 1.2.

1.6.3. Mass Production

Due to industrial demand to scale up fiber production via electrospinning, novel methods have been proposed to accommodate electrospinning setups for mass production. These setups are discussed in Table 1.3.

Table 1.1. Electrospinning setups for collecting random fibers
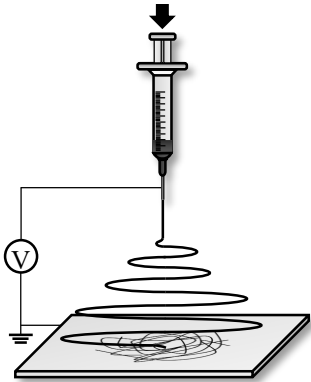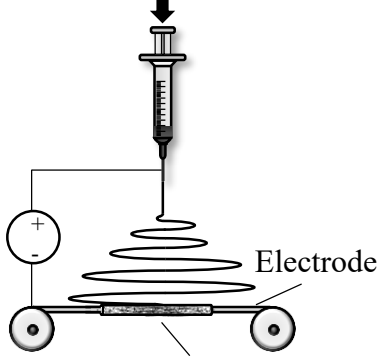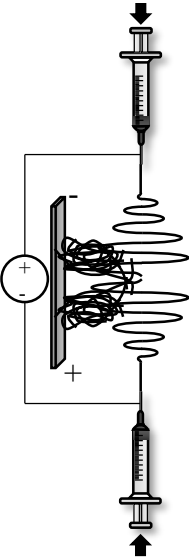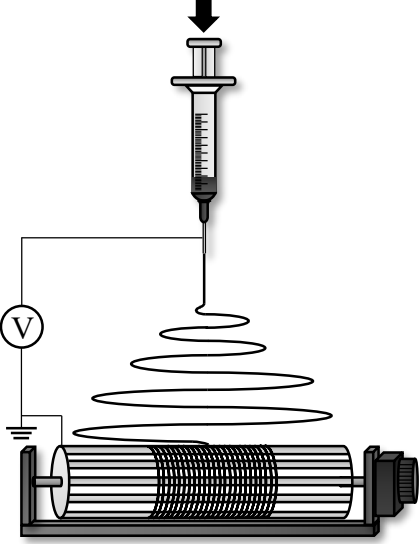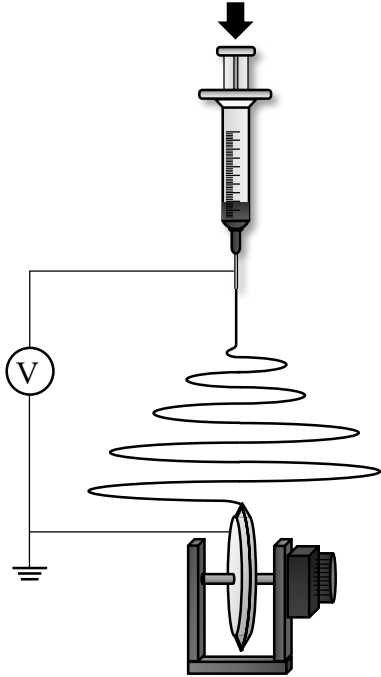
Setup	Description	Ref
Plate collector 	A grounded stationary plate is used to collect fibers extruded from syringe with high voltage exerted on the needle. The plate is either flat or bowl-shape. The spherical surface can increase uniformity and charge capacity of the resulted fibers.	96
Line electrode Electrode Supporting Tube and Collected Fibers	Copper line electrode is fixed with stationary rollers and connected to negative voltage. Supporting tube is wrapped around the electrode to collect random fibers from positively charged syringe. It is an efficient process to produce highly porous mats like filtration membrane.	97
Dual nozzle 	Two syringes with opposite charges are spinning towards each other. If no collector is placed in between, a spool of entangled fibers is collected in air. If a plate is placed close to and parallel to the field, the two ends of the plate experience opposite charges. The fibers extruded from the positive syringe are attracted to the negatively-charged part of the plate, and vice versa. The fibers can be twisted into a yarn for collection.	98

Table 1.2. Electrospinning setups for collecting aligned fibers

Setup	Description	Ref
Rotating Drum or wire drum 	Fibers are aligned on a rotating drum with a uniform surface or wire-frame. Either negative voltage or grounding is applied to the drum. Single or dual syringes can be used for solution ejection. Dual syringes with same charge facing toward the drum or dual syringes with opposite charges facing each other can be accommodated depending on the desired properties of the resulted fibers. Rotating drum possesses large deposition area. Curved electrode around the surface of the drum can be utilized to control the electric field.	99–103
Rotating disk 	Rotating disk is similar to rotating drum except the fibers are collected across the thin edge of the disk. The sharpened edge is designed to strengthen fiber attraction.	104

Rotating ring
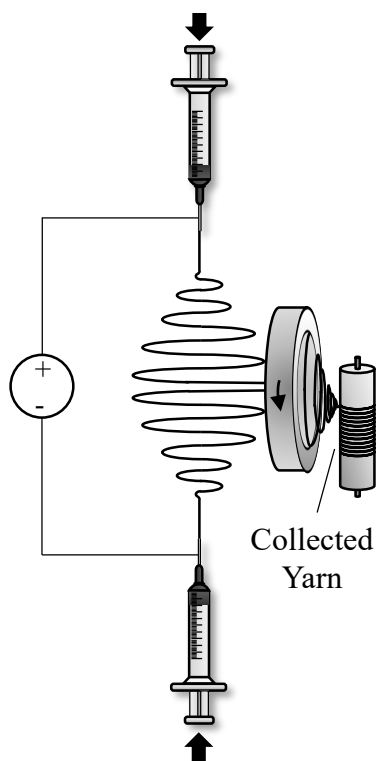
When dual spinnerets with opposite charges are used, a rotating ring can be placed between the spinnerets and a drum for spinning the fibers into yarn. It assists with fiber twisting for yarn collection. [105]

Collected Yarn
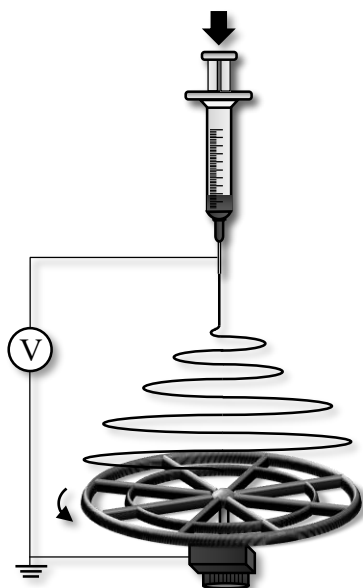
Rotating grid

Rotating grid is a hollow disk bearing resemblance to a gear wheel. Instead of collecting fibers across the thickness, the fibers are ejected towards the disk face. The fiber alignment is slightly weaker compared to other rotating collectors. [106]

Gap spinning

Electrode or
Cylinder
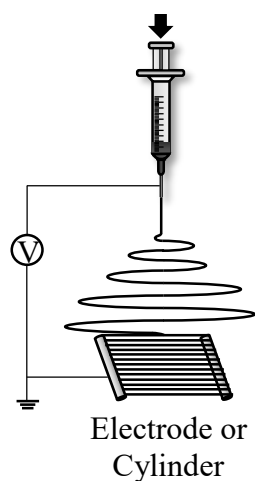
When electrodes or conductive cylinders are placed in parallel, the charged solution jet tend to form fibers across the gap in between the [107,108] collectors. The fibers are naturally aligned over the gap.

Magnetic

Collector
with Magnets
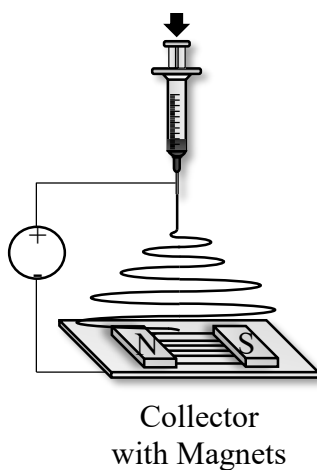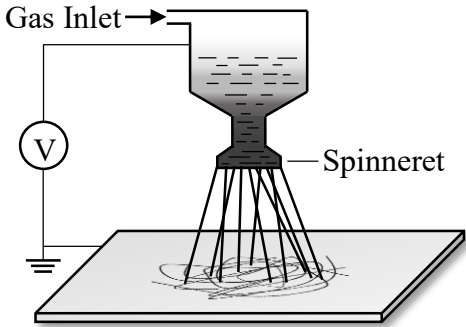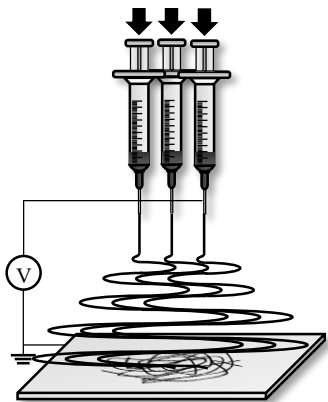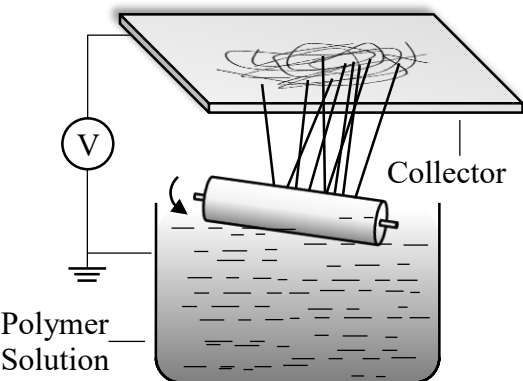
By placing magnets on the negatively charged collector, the magnetic field aligns the fibers on the [109] collector.

3D
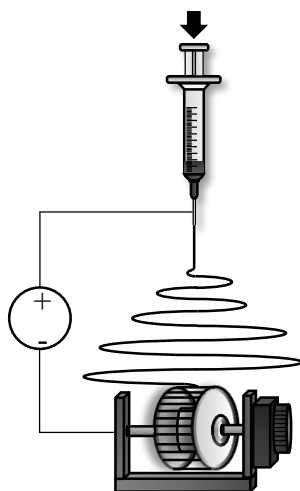
3D spinning of aligned fibers can be achieved through specific setups, such as spinning across gap of spool, rotating intersected rectangular plates, or customized shapes. The spatial structure of fibers makes 3D scaffolds feasible. [110–112]

Table 1.3. Electrospinning setups designed for mass production

Setup	Description	Ref
Bubble spinning	Bubble spinning combines electrospinning with gas spinning. The charged aerated solution is extruded into multiple jets under electric field and gas pressure. The process is fast but hard to control.	[113]
Multi-spinnerets	Multiple spinnerets are placed in a row or in certain layouts to electrospin fibers at the same time. It increases the production of the fibers but also makes control of fiber morphology more challenging.	[114]
Needleless	A commercial patented electrospinning setup named "nanospider" uses a rotating cylindrical device to spatter charged solution to into thin jets which subsequently land on the collector. The setup does not require needle, so its production can be expanded to industrial scale. Another splash electrospinning setup is also needless where solution is dispensed on positively charged rotating cylinder. The spinning of the cylinder ejects solution jets, which solidify as fibers at the collector.	[115]

1.7. Potential Defects from Electrospinning

Electrospun fibers may exhibit defects due to unoptimized solution concentration, polymer purity, electrospinning parameters, or ambient conditions. The defects may induce poor mechanical properties in CNFs. It is compelling to characterize the mechanisms that cause these defects to mitigate defect generation. Some general defects encountered in electrospinning are shown below.

1.7.1. Bead/BOAS

Bead or beads-on-a-string (BOAS) structure is one of the most common defects in electrospinning, which decreases the specific surface area of fibers. Beads are mostly caused by Rayleigh instability or bending instability, which induces variation in jet diameter due to high surface tension at low electric field or charge repulsion at high electric field[94,116]. If jet instability reduces the elongation force or solution viscosity is low, the jet may break. This phenomenon is called capillary breakup. Surface tension favors spherical shape, so the breakup generates beads. The jet in between beads regains stability and maintains the fiber shape. In this way, BOAS structure forms. Most beads exhibit round and smooth surface. If beads show collapsed shapes, it is caused by trapped solvent evaporating after bead formation[117]. Low viscosity, low net charge density, and strong surface tension tend to induce bead formation[118]. Solution viscosity is affected by polymer concentration. Net charge density can be increased with applied electric field. Properties of solvent and polymer, such as dielectric coefficient or viscoelastic properties, affect all three factors.

1.7.2. Ribbon Structure

Besides distinctive defects like BOAS, irregular shapes of fibers can also be considered as defects. Uniform fibers show circular cross sections, while defective fibers do not exhibit cylindrical features. Baji et al. ascribed it to incomplete solvent evaporation during the travel of the jet[94]. As the residual solvent evaporates afterwards, the fiber loses the circular shape and becomes flattened. Trapping of solvent can be caused by insufficient spacing between the spinneret and the collector since the applied voltage charges the jet but the distance is not enough for the solvent to escape. Koombhongse et al. summarized several forms of irregular fibers[119]. Fibers with porous surface, wrinkled features, elliptical, flat, and ribbon-like cross sections, are all generated by solvent evaporation via diffusion. Ribbon-like fibers have two tubular sides with flattened

portion linking them. The two ends tend to get in contact due to cohesive force, therefore, ribbon-like fibers are typically twisted[119].

1.7.3. Fusion

To prevent lignin fibers from forming non-uniform structure with large diameters or generating beads, binding polymer such as poly(ethylene oxide) (PEO)[120] is mixed with lignin to enhance its spinnability. Fiber fusion, characterized as the merging of junctions when fibers overlap, occurs at high PEO concentration due to low glass transition temperature of PEO. Kadla et al. reported PEO with concentration higher than 5% could cause instability and inter-fiber fusion during heat treatment for HW-KL[120]. Dallmeyer et al. considered fusion to be defective for electrospun lignin fibers[57], while Ding et al. claimed fusion had positive effects on the mechanical properties of the fiber mats after carbonization because of reinforced bonding[84]. However, fiber fusion does prevent nanofibers from maintaining fiber forms after carbonization[121], and therefore poses obstacles in achieving uniform lignin-based CNFs.

1.8. Parameters Affecting Electrospining

Parameters in electrospinning can have significant impact on morphology, mechanical and chemical properties of the fabricated fibers. Alteration of certain parameters may cause failure in electrospinning or defects in collected fibers. In order to obtain high-quality fibers without defects, it is crucial to analyze the role of each parameter and optimize the electrospinning process. Some of the parameters that have major effect on electrospinning are briefly discussed below.

1.8.1. Electric Field

Strength of electric field is defined to be the ratio between applied voltage and tip-to-collector distance. Higher electric field imposes stronger stretching force to produce lower fiber diameters[122], which is in agreement with theoretical model[123]. However, the intricate electrospinning conditions make implement of the theoretical prediction complicated, especially when the individual effects of voltage and distance are analyzed. Longer distance was found to facilitate solvent evaporation and jet branching[124]. Therefore, distance has a complex relationship with fiber diameter[125,126]. Applied voltage, on the contrary, mostly exhibits a stable negative correlation to fiber diameter[122]. Stronger electric field forms finer fibers, but increasing electric field after a certain threshold causes unstable Taylor cone or electrospraying of droplets[127]. A study of the polarity test confirmed that applying positive voltage on spinneret and grounding collector had higher yield than applying positive voltage on collector and grounding spinneret[128].

1.8.2. Humidity & Temperature

Ambient conditions also have sophisticated effects on electrospinning. In a study conducted by Verieze et al., both humidity and temperature were found to have opposite effects on electrospun fibers[129]. Dependent on the structure of polymer, high humidity can either suppress evaporation of solvent to lengthen the time for jet thinning, or accelerate the precipitation of polymer from solvent. These two outcomes lead to opposite effects, decreasing or increasing fiber diameters. Elevated temperature has similar effects. Higher temperature either causes faster evaporation rate or higher molecular chain mobility that decreases solution viscosity. The accelerated solidification increases fiber diameter while the lower solution viscosity decreases fiber diameter[129].

1.8.4. Flow Rate

Flow rate is an essential parameter in electrospinning. Zargham et al. characterized how flow rate affected the electrospinning behavior[130]. Discontinuous spinning occurs if the flow rate is either too low or too high. Lower flow rate decreases fiber diameter but makes Taylor cone unstable. Specifically, the jet inclines towards one side of the internal surface of the needle so that the jet loses Taylor cone shape. Instead of opposing surface tension of the solution, electric field needs to overcome the shearing force from the inner surface of the needle. This causes jet breakage as highly-charged jet is too thin. Reformation of Taylor cone later takes place. Repeated formation and collapse of Taylor cone induce high variation in fiber diameter distribution. On the other hand, if flow rate is too high, incomplete solvent evaporation occurs as high amount of solution is ejected, causing fibers to be fused. In addition, electric field cannot distribute electric charge over the solution. Uncharged droplets start dripping due to gravity, and defects are generated by the incomplete solvent evaporation[130].

1.8.5. Solution Properties

Solution viscosity and surface tension are controlled by multiple factors, such as solution concentration, temperature, chemical properties of polymer and solvent. Low solution viscosity makes jet behavior governed by surface tension, so discontinuous jet spinning like dripping likely occurs. High solution viscosity causes the adhesion between solution and needle tip to be so strong that electric field cannot stretch solution into jet[127]. Besides viscosity and surface tension, extensional properties of the solution also influence electrospinning behavior and fiber diameter. Dallmeyer et al. found that using PEO as plasticizer for electrospinning SW-KL increased solution

viscoelasticity and viscosity[131]. Higher SW-KL and PEO concentrations as well as larger PEO MW cause stronger exponential thinning and longer relaxation time. The exponential thinning behavior, where the solution under extensional stress is stretched into finer jet, determines the spinnability of the solution. Increase in relaxation time, or time for solution to be elongated into thin jet, causes larger fiber diameters[131]. The critical point for the solution to change from dripping to smooth spinning occurs when the relaxation time is higher than Rayleigh breakup time[132]. The threshold for transforming BOAS to bead-free fibers depend on both relaxation time and viscosity[133].

1.8.6. Solvent Properties

Large fiber diameters or defects arise from solvents with relatively high solubility since they tend to cause high evaporation rate and low dielectric constant. Solvent with high dielectric constant produces thinner fibers and increases porosity in mats without changing deposition mass. Increase in solvent dielectric constant demands higher applied voltage but it results in smooth and bead-free fibers[134].

1.9. Carbon Fiber Production from Lignin

The manufacturing process for CFs is called carbonization. It consists of two to three steps, including thermostabilization and carbonization. Other subsequent steps, graphitization or activation, only apply to production of graphite fibers or PAN-based CFs.

1.9.1. Thermostabilization

Thermostabilization is a significant step to ensure generation of uniform fibers after carbonization. Carbonization temperature far exceeds glass transition temperature of lignin, so thermostabilization prevents lignin from melting. Thermostabilization is achieved by oxidation of lignin in air at 200-250 °C where oxygen-derived radicals are introduced[135]. Crosslinking at slow heating rate increases glass transition temperature of lignin and avoids lignin softening during carbonization. Thermostabilized fibers show improved mechanical properties after carbonization than fibers without thermostabilization[136]. Three main parameters for thermostabilization are heating temperature, heating rate, and duration[50]. Other parameters such as gas flow rate and tension can also affect quality of thermostabilized fibers. During thermostabilization, volatile material is removed while hydrogen content greatly reduces. Oxygen composition increases due to oxidation of aliphatic groups. If the heating temperature is too high, formation of aromatic ring and other structures via condensation occurs. Depending on the heating rate, thermostabilization can cause either relaxation to increase mobility of molecular chain, or formation of cross-linked

structures to reduce molecule mobility[57]. Slow heating rate favors cross-linking, thereby increasing glass transition temperature of the fibers and inhibiting fiber fusion in carbonization. Even though thermostabilization improves mechanical properties of CFs, skipping the thermostabilization process can form interconnected fibers with enhanced electric conductivity[137].

1.9.2. Carbonization

Carbonization is the final step to transform lignin into carbon fibers. It is a process that heats lignin at a high temperature in an inert environment to remove substances other than carbon. Carbonization can be divided into three stages: at the first stage, amorphous carbon forms around 500-900 °C; at the second stage, intermediate entity between amorphous and graphitized carbon forms at 900-1400 °C; at the third stage, graphite forms above 1400 °C[138]. In a characterization of carbonization process, oxygenated compositions rapidly reduce while carbon-carbon structures remain[50]. The carbon content increases drastically when raising the temperature[139].

1.10. Mechanical Properties of Lignin-based Carbon Fibers

Recent studies have investigated mechanical properties of lignin fibers after electrospinning and carbonization. Table 1.4 provides a comparison of mechanical properties for electrospun lignin fiber mats and their CNFs reported by recent articles. The effects of electric field (F_∞), flow rate (Q), and binder polymer on tensile strength (σ), elastic modulus (E), and fiber diameter (D) for as-spun and carbonized fibers are summarized. If studies show different results for different parameters, only the best mechanical properties (highest σ and E) are included in the table. Smaller fiber diameter is desired as increased surface area and larger amount of tangled fibers result in better mechanical properties[140], as well as higher electrical conductivity for electronics applications[141]. From Table 1.4, it can be concluded that it is plausible to achieve lignin-based CNFs with average diameter lower than 100 nm, but consistent production of CNFs from various types of lignin is still challenging. In addition, recently reported lignin-based CFs and CNFs manufactured by electrospinning still possess mechanical properties much lower than commercial PAN or pitch-based CFs. There is immense research potential into methods to strengthen mechanical properties of lignin-based CNFs, such as embedded reinforcing fillers, purification methods, chemical modification of lignin, alternative sources of lignin, etc.

Table 1.4. Mechanical properties of lignin-based carbon fibers via electrospinning

Lignin	Binder	Electrospinning Conditions		As-spun Mechanical Properties			Carbonized Mechanical Properties			Ref
		F_∞ (kV/m)	Q	σ (MPa)	E (MPa)	D (nm)	σ (MPa)	E (GPa)	D (nm)	
SW-KL	PEO	67-100	0.01-0.03 mL/min	8.4*	702 MPa*	578±69	53.4 MPa*	6.9 GPa*	319±34	[136]
SW-KL	PEO	45-100	0.03 mL/min	N/A	N/A	875±111	32.0±9.0 MPa	4.8±0.6 GPa	634±87	[85,142]
OL, Butyrated OL (BOL)	PAN	75	5 µL/min	N/A	N/A	OL: 1920±150 BOL:1690±70	OL: 22±1 BOL: 83±17	OL: 2.4±0.2 BOL: 6.1±0.6	OL: 1069±97 BOL: 1016±65	[84]
HW-KL	PAN	60-73	0.85-10.5 µL/min	N/A	N/A	N/A	89.4±25.5	2.5±0.6 GPa	561.7±79.2	[143]
Sulfur-free SW-KL	PEO	70	420nl/s	N/A	N/A	809±26	32±9	N/A	N/A	[139]
SW-KL	PEO	83	0.03 mL/min	5.13 ±0.64	514.63 ±70.93	977±112	45.03±9.93	6.24±1.31	639±75	[95]
SW-KL, HW-KL, Sulfonated KL (SKL), HW-OL, Softwood Organosolv Lignin (SW-OL), Pyrolytic Lignin (PL), SL	PEO	45-100	0.03 mL/min	N/A	N/A	SW-KL: 1318±251 HW-KL: 1085±188 SKL: 702±186 SW-OL: 1517±415 HW-OL: 1135±171 PL: 912±176 SL: 1645±371	N/A	N/A	N/A	[142]
SW-KL	PEO	75	0.01-0.02 mL/min	N/A	N/A	~1200	N/A	N/A	N/A	[131]
OL	N/A	12/0.2-0.25	Ethanol: 0.06 mL/h Lignin: 0.8 mL/h	N/A	N/A	800-3000	N/A	N/A	400-1000	[83]
AL	PVA	104	1.2 mL/h	N/A	N/A	~140 - ~220	N/A	N/A	~100 - ~150	[144]
HW-OL	PAN	67-100	0.6-4 mL/h	N/A	N/A	61 (bead) - 2240	N/A	N/A	N/A	[44]

* Data were extracted from published graphs using GetData Graph Digitizer 2.26

1.11. Design of Experiment Methods

Design of experiment (DOE) methods are long-established approaches to analyze effects of parameters in experiments and optimize the experiments to increase efficiency or lower running cost. The following methods are some frequently adopted DOE methods for experiments containing 3 parameters and 3 levels. Level corresponds to the discrete numerical values of each parameter.

1.11.1. Full Factorial Design

A schematic of 3^3 full factorial design is shown in Figure 1.4a. The black dots on the cube illustration correspond to design points or test runs required to be conducted in the experiment. Each axis represents a parameter (A, B, C) with different levels. The advantages of full factorial design include analysis of interaction effects among parameters and more accurate prediction for the surface curvature of the model representation for response surface methodology. Meanwhile, it is expensive in cost. Paterakis et al. used 3^3 full factorial design as an optimization model with replicated center points[145]. The replications were conducted to estimate experimental error and confirm the reliability of the experiment. 2-level factorial design can reduce number of runs, but sacrifice of intermediate levels fails to achieve model accuracy[146].

1.11.2. Central Composite Design

Central composite design (CCD) in Figure 1.4b removes the intermediate runs in full factorial design but keeps the center point. Then it adds 4 data points lying at a distance of α away from the center point. The distance $\alpha = 2^{(n-p)/4}$, calculated from n parameters and p levels[147], can provide curvature prediction for data points with wider range. This type of CCD is Circumscribed Central Composite (CCC). Other CCD designs can modify α based on experimental requirement. CCD method is more efficient than full factorial design while preserving accurate model prediction[146]. Replication of center point is typically required to reduce error.

1.11.3. Box-Behnken Design

Box-Behnken design (Figure 1.4c) is another efficient method with fewer test runs. It includes data points only at the middle of each edge of the cube representation along with the center point. Box-Behnken design has even lower cost than CCD. Removing data points from cube corner prevents extreme experimental cases from compromising model validity[148]. It provides reliable estimation for quadratic model. Similar to CCD, it requires additional design points for more accurate model fitting. Full factorial design, CCD, and Box-Behnken design are all parts of

response surface methodology for identifying optimal parameters by analyzing the correlations between parameters and responses.
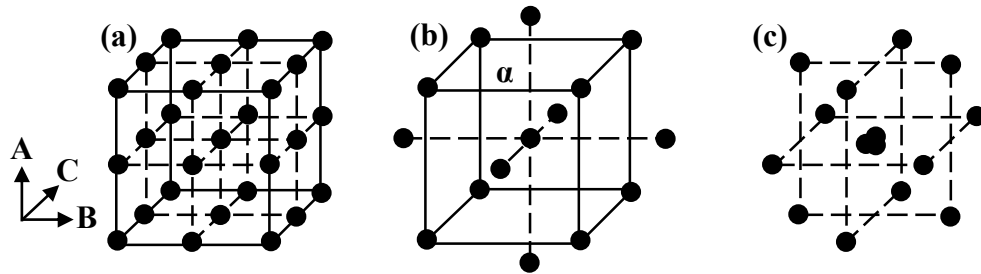
Figure 1.4. Design of experiment methods of (a) full factorial design, (b) central composite design, and (c) Box-Behnken design with 2 extra center points for 3 parameters (A, B, C) and 3 levels.

Chapter 2. Experimental

2.1. Materials

Kraft lignin was extracted from West Fraser Pulp Mill, Hinton, Canada. Kraft Lignin A (KLA) and Kraft Lignin B (KLB), referred to as Amallin^{TM} lignin at West Fraser, were provided by Innotech, Alberta. KLA was acidic and KLB was alkaline. The bio-cleaning process was conducted by Dr. Ghosh with *Pseudomonas Fluorescence* bacterium to cleave the bonds for carbohydrates and release sugar. Bio-cleaned KLA and KLB are named as Bio-KLA and Bio-KLB. After bio-cleaning, Bio-KLA and Bio-KLB showed 87-99% reduction in ash, 57-70% reduction in carbohydrate, 5-65% increment in lignin content and higher lignin MW[149]. Bio-KLB contains substantially higher acid-soluble content than Bio-KLA. Other chemicals were used without further purification. PEO (1000 kDa, 2000 kDa, 5000 kDa) and DMF were purchased from Sigma Aldrich, Canada. PEO was used to assist lignin with electrospinning. The electrospun lignin fiber mats and their CFs investigated in this study are summarized in Table 2.1.

Table 2.1. Abbreviations for lignin-based electrospun fibers and carbon nanofibers investigated in this study

Abbreviation	Lignin Samples
KLA-R	As-spun random KLA fibers
KLA-R-CNF	Random KLA carbon nanofibers
Bio-KLA-R	As-spun random Bio-KLA fibers
Bio-KLA-R-CNF	Random Bio-KLA carbon nanofibers
Bio-KLB-R	As-spun random Bio-KLB fibers
Bio-KLB-R-CNF	Random Bio-KLB carbon nanofibers
KLA-A	As-spun aligned KLA fibers
KLA-A-CNF	Aligned KLA carbon nanofibers
Bio-KLA-A	As-spun aligned Bio-KLA fibers
Bio-KLA-A-CNF	Aligned Bio-KLA carbon nanofibers

2.2. Solution Preparation

All prepared lignin powders (KLA, Bio-KLA, and Bio-KLB) were vacuum dried at 100 ℃ overnight to remove humidity prior to electrospinning. PEO was first dissolved in DMF at a stirring rate of 600 rpm and heating temperature of 80 ℃. These parameters were adopted from previous work[133]. After no particle was visible in the solution, lignin powder was added to the PEO-DMF mixture under the same stirring condition overnight (over 12 hours). Then the solution was cooled down to room temperature (RT). For KLA and Bio-KLA, the solution with total solid concentration of 22 wt% was reheated to 80 ℃ at 600 rpm stirring rate for 30 min and cooled to RT again prior to electrospinning to achieve homogeneous mixture. For solid concentration over 30 wt%, the solution was cooled to 60 ℃ instead of RT to increase the spinnability. The solution was barely spinnable at high solid concentration (≥30 wt%) without preheating. KLB without bio-cleaning formed a gel texture as shown in Figure 2.1. After bio-cleaning, the viscosity of the solution decreased significantly. Bio-KLB was still not spinnable after heating and stirring overnight under the same condition as KLA and Bio-KLA. However, it became spinnable after constant heating at 80 ℃ with stirring rate of 600 rpm for at least 4 days.
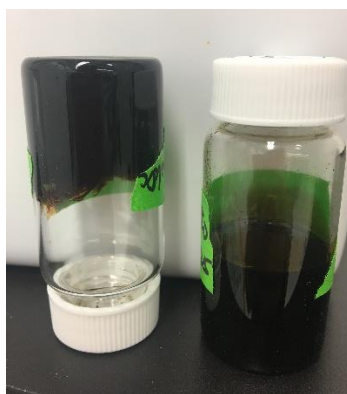
Figure 2.1. Solution of KLB (left) and KLA (right) showing the high viscosity of KLB solution.

2.3. Electrospinning

2.2.1. Random Fiber Mat

The static electrospinning system is shown in Figure 2.2. The solution was loaded into a BD 10 mL syringe with eccentric luer slip tip (Becton, Dickinson and Company, NJ, USA) equipped with 20G BD PrecisionGlide™ needle blunted by a rotary tool (DREMEL®, WI, USA). The syringe and the needle were purchased from Fisher Scientific, Canada. The syringe was driven by a dual syringe infusion pump (GENEQ Inc., Montreal, Canada). The feed rate was kept constant

at 420 nl/s. The randomly deposited lignin/PEO fibers were collected by a grounded metal plate covered with aluminum foil. The aluminum foil substrate was used to facilitate the removal of the fibers. An electric field (50-70 kV/m) was generated by attaching the needle with a power supply (GAMMA High Voltage, Ormond Beach, FL, USA). The tip-to-collector distance was 20 cm. To prevent the fiber from being collected on other surfaces, a piece of aluminum foil was pierced through the needle to concentrate the electric field toward the travelling direction of the fibers. The metal frames for the electrospinning setup was grounded and wrapped with non-conductive cover. The collection time for random fibers was 30 min. The electrospinning process was carried out at RT (19-22 °C) but relative humidity (RH) was not controlled. Most fibers were electrospun at RH of 3-4%.
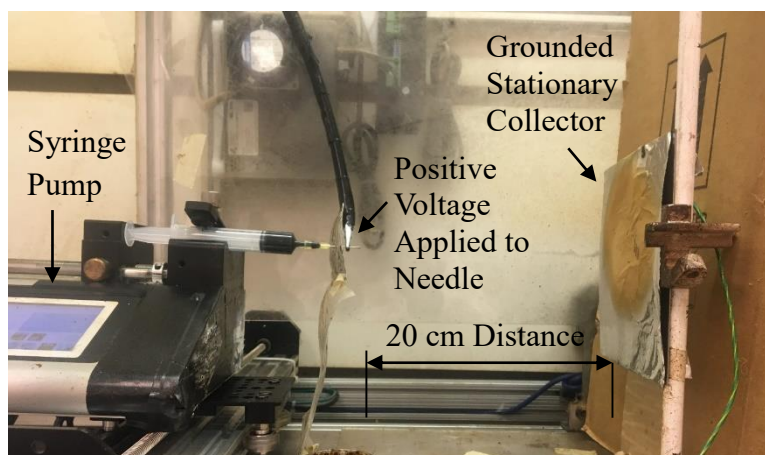
Figure 2.2. Electrospinning setup with static collector for preparing as-spun random fibers.

2.2.1. Aligned Fiber Mat

The electrospinning setup for collecting aligned fibers is shown in Figure 2.3. A rotating drum was used as the collector and was covered with aluminum foil. The needle was located 1 cm above and 20 cm apart horizontally from the top of the drum, where the drum was grounded by a brush. The solution condition was maintained the same as that for the random fibers. Applied electric field of 65-80 kV/m, rotating speed of 2000-3000 rpm, and feed rate of 420-460 nl/s were applied. The collection time was 60 min for aligned fibers. For most electrospinning conditions of aligned fibers, the fibers were not removable from the aluminum foil. Therefore, DuPont Silicone lubricant with Teflon® fluoropolymer (hereinafter referred to as release agent) was applied on the aluminum foil to aid the transfer of the fibers. The effects of release agent on the fibers were studied by comparing the mechanical properties and the fiber morphologies of the random fibers collected with and without release agent.
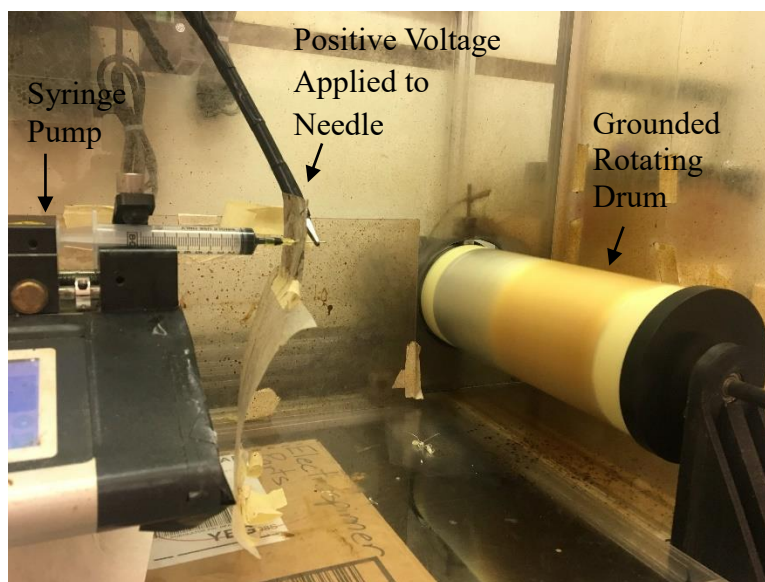
Figure 2.3. Electrospinning setup with rotating drum for preparing as-spun aligned fibers.

2.3. Thermostabilization

The as-spun fiber mats were cut into 40 mm X 70 mm specimens and placed on quartz plates or combustion boats. Then the specimens were slid into the chamber of a tube furnace (Lindberg/Blue M^{TM}). No tension was applied to the specimens otherwise tear or slit would be introduced as the specimen shrank during thermostabilization. The specimens were heated to 250 °C at a rate of 0.5 °C/min in air. The heating rate was optimized in a previous work[139] to prevent fusion. The target temperature was held constant at 250 °C for 1 hour and cooled to RT at a rate of 5 °C/min.

2.4. Carbonization

Argon gas was flowed into the tube furnace continuously for 3 hours to eliminate air inside the chamber. The thermostabilized specimen was heated to 250 °C at a rate of 0.5 °C/min and held isothermally for 1 hour under argon. Argon was used to prevent oxidation as temperature further increased. The specimen was then heated to 1000 °C at a rate of 5 °C/min and held for 1 hour. The temperature was cooled to RT at a rate of 5 °C/min. The weight of the specimen was measured before and after the carbonization process to calculate mass yield of carbonization. Wrinkled portions of the specimen were removed before tensile test.

2.5. SEM

For each as-spun and carbonized fiber mat, two small samples were cut from different locations for SEM (Zeiss EVO MA 10, Oberkochen, Germany). The specimens were laid on studs with carbon tape and gold-coated with Gold Sputtering Unit (DESK II, Denton Vacuum, Moorestown, USA). The SEM images were taken by Dr. Ghosh at accelerating voltage of 20 kV.

2.6. Analysis of Fiber Diameter and Orientation

Fiber diameter and orientation were obtained by manually measuring over 100 fibers with ImageJ/Fiji analysis software (NIST, version 1.52 p) from the SEM images. To quantify fiber orientation, an arbitrary reference line was first chosen and the angle between the axis of each measured fiber and the reference line was calculated. The angle distributions were then shifted so that the orientation with the highest probability was assigned 0° as the alignment direction. The distributions of the fiber diameter and orientation were analyzed by Descriptive Statistics in Excel. DiameterJ, a plugin of ImageJ, was initially utilized to automatically measure the fiber diameters. However, the histogram produced by DiameterJ contained substantial errors due to the incapability to exclude outliers and noise from the thresholding technique. Therefore, manual measurement was conducted instead.

2.7. Tensile Test

10 mm X 50 mm specimens were cut from three KLA, Bio-KLA, or Bio-KLB fiber mats. Aligned fiber specimens were cut along the alignment direction to ensure that the loading direction was in line with the alignment of the fibers. Each specimen was placed inside a C-shape paper holder with length of 50 mm and web thickness of 10 mm to reduce stress concentration, as shown in Figure 2.4. After clamping the specimen with the grippers, the tensile test was conducted by ElectroForce 3200 Series III tensile machine (Bose Corporation). The load cell was capable of going up to 250 g. The strain rate was 0.01 mm/s and the gauge length of the specimen was 30 mm. The ambient condition was maintained at ~25 °C with ~25 % RH. Strain was determined as the percentage ratio of the change in vertical deformation over the gauge length. Strain over 40 % could not be obtained due to extension limit. Mechanical properties were analyzed only for the specimens not fractured at the grippers, with 10 replications for as-spun fibers and 5-10 replications for CNFs.
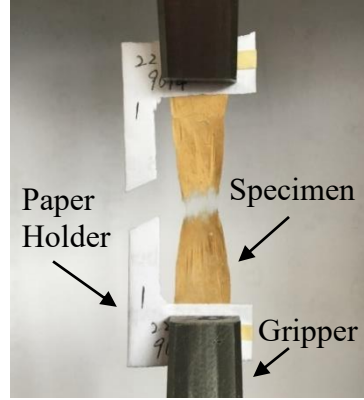
Figure 2.4. Tensile sample of KLA-R fractured in the middle.

The thickness of the fiber mats could not be measured accurately with the accessible equipment. So the load (g) reported by the tensile machine was converted to stress (MPa) by adopting a method assuming that the fiber mat was composed solely of lignin with bulk density (ρ) of 1.35 g cm^{-3} for as-spun fibers[56], and of carbon with ρ = 1.70 g cm^{-3} for CNFs[150]. The areal density of the fiber mat was obtained by[151],

$$\text{Areal density (g m}^{-2}) = \frac{\text{Mass (g)}}{\text{Width (m)}\times\text{Length (m)}}$$ [2.1]

The areal density was used to measure the specific stress,

$$\text{Specific Stress (g tex}^{-1}) = \frac{\text{Load (g)}}{\text{Width (mm)}\times\text{Areal density (g m}^{-2})}$$ [2.2]

The stress (MPa) was then calculated from the specific stress by multiplying it with the gravitational acceleration (g, in m s^{-2}) and density of lignin (ρ),

$$\text{Stress (MPa)} = \text{Specific Stress (g tex}^{-1}) \times \text{g} \times \rho$$ [2.3]

Since fraction of PEO was low (~1%), density of PEO was omitted in the calculations.

2.8. Optimization

2.8.1. Electrospinning Parameters

Effect of electrospinning parameters, including flow rate, preheating, collection time, voltage and distance (electric field) on the fiber diameter and the morphology was analyzed and optimized by the one-factor-at-a-time method. Flow rate was optimized to achieve minimum fiber diameter and uniform fiber morphology. Depending on the spinnability of the solutions, flow rate ranging from 400 nl/s to 500 nl/s was applied to determine how flow rate changed fiber morphology and diameter. Flow rates outside this range were tested but the solution either ceased

to form fibers or started severe electrospraying. For collection time, the as-spun fiber mats were collected with duration varying from 15 min to 30 min while fixing other parameters. To address the effect of preheating, the solution was preheated to 60 °C before the electrospinning process to analyze if elevated temperature affected the fiber diameter of the as-spun mats. Afterwards, the solution was not heated continuously and no insulation material was applied to the syringe during the electrospinning process. Therefore, the solution was naturally cooled to RT within the collection time. The individual effect of voltage (10-14 kV) and distance (20-22 cm) was studied.

2.8.2. Spinnability Test

The spinnability of the lignin solution was tested for the parameters as follows: total solid concentration of 22-35 wt%, lignin/PEO ratio of 95/5-99.9/0.1, and PEO MW of 1000-5000 kDa. These solution parameters were selected for random fibers based on previous work[152]. The physical characteristics and the ability to be electrospun were characterized for each condition.

2.8.3. Optimization for Random Fibers

After characterizing the spinnability of the lignin solution and analyzing the electrospinning parameters by one-factor-at-a-time listed in Section 2.8.1, three parameters (Table 2.2) were further optimized for the random fibers using the spinnable conditions. The parameters were electric field (F_∞, 50-70 kV/m), lignin/PEO ratio ($r_{L/P}$, 95/5-97/3), and MW of PEO (W, 1000-5000 kDa). Each parameter was expressed in coded values, -1, 0, and 1, corresponding to low, intermediate, and high levels. The responses were fiber diameter (D, nm), elastic modulus (E, MPa), and tensile strength (σ, MPa). The main parameter effects and the parameter interaction effects were inspected in a prediction model generated by Design Expert® (Stat-Ease, version 11). Three models were recommended to fit different parameters with $\hat{y}$ as the predicted response, β_i as the main effect of ith parameter, β_{ij} as the interaction effect between i^{th} and j^{th} parameters, and x_i as the value of the ith parameter. The regression equation for linear model was

$$\hat{y} = \beta_0 + \beta_1 x_1 + \beta_2 x_2 + \beta_3 x_3 \tag{2.4}$$

The regression equation for two factor interaction (2FI) model was

$$\hat{y} = \beta_0 + \beta_1 x_1 + \beta_2 x_2 + \beta_3 x_3 + \beta_{12} x_1 x_2 + \beta_{13} x_1 x_3 + \beta_{23} x_2 x_3 \tag{2.5}$$

The regression equation for quadratic model was

$$\hat{y} = \beta_0 + \beta_1 x_1 + \beta_2 x_2 + \beta_3 x_3 + \beta_{12} x_1 x_2 + \beta_{13} x_1 x_3 + \beta_{23} x_2 x_3 + \beta_{11} x_1^2$$
$$+ \beta_{22} x_2^2 + \beta_{33} x_3^2 \tag{2.6}$$

Data were fitted to suggested model for further analysis with response surface methodology and ANOVA analysis. The optimal condition was obtained with desirability function. To maximum or minimize a response with value y_i, the desirability d_i was computed using the following equations after assigning lower limit $(y_i)_{min}$, upper limit $(y_i)_{max}$, and weight w_i of the reponse[153],

$$d_i(\text{maximize}) = \begin{cases} 0, y_i < (y_i)_{min} \\ (\dfrac{y_i - (y_i)_{min}}{(y_i)_{max} - (y_i)_{min}})^{w_i}, (y_i)_{min} \leq y_i \leq (y_i)_{max} \\ 1, y_i > (y_i)_{max} \end{cases}$$

$$d_i(\text{minimize}) = \begin{cases} 1, y_i < (y_i)_{min} \\ (\dfrac{(y_i)_{max} - y_i}{(y_i)_{max} - (y_i)_{min}})^{w_i}, (y_i)_{min} \leq y_i \leq (y_i)_{max} \\ 0, y_i > (y_i)_{max} \end{cases}$$

[2.7]

For each response y_i, importance t_i ranging from + (1) to +++++ (5) can be assigned. Then the desirability for the combination of n responses is,

$$d = (\prod_{i=1}^{n} d_i^{t_i})^{\frac{1}{n}}$$

[2.8]

The default importance +++ (3) was assigned to all responses. The goal of the optimization was set to minimize fiber diameter, maximize tensile strength, and elastic modulus. Parameter condition with BOAS fiber morphology was not considered even though its desirability was high.

Table 2.2. Optimization parameters for random fiber with total solid concentration of 22 wt%

Factor	F_∞ (kV/m)			$r_{L/P}$			W (kDa)		
Level	Low	Center	High	Low	Center	High	Low	Center	High
Coded Value	-1	0	1	-1	0	1	-1	0	1
Actual Value	50	60	70	95/5	96/4	97/3	1000	2000	5000

2.8.4. Box-Behnken Optimization of Aligned Fibers

Box-Behnken design was adopted to optimize the parameters for aligned fibers. The Box-Behnken method was chosen since it could construct valid estimations in more efficient manners in comparison to central composite design or full factorial design[146]. Two extra center points were exploited to generate reproducible results in order to lower the experimental variability. The

optimized solution properties for random fibers, including the lignin/PEO ratio and MW of PEO, were employed for aligned fibers without modification. The parameters analyzed for aligned fibers were electric field (F_∞, 65-80 kV/m), flow rate (Q, 420-460 nl/s), and rotating speed (Ω, 2000-3000 rpm) in Table 2.3. The responses and the goal of optimization were the same as those for the random fibers. Due to utilization of release agent, higher electric field was required to yield uniform aligned fibers since release agent acted as a thin electric isolation layer for the collector. Therefore, the flow rate was also adjusted to accommodate the change in the electric field. Rotating speed higher than 3000 rpm was not feasible due to equipment limitation. The upper and lower limits of each parameter were designated to avoid solution dripping and electrospraying.

Table 2.3. Optimization parameters for aligned fiber

Factor	F_∞ (kV/m)			Q (nl/s)			Ω (rpm)		
Level	Low	Center	High	Low	Center	High	Low	Center	High
Coded Value	-1	0	1	-1	0	1	-1	0	1
Actual Value	65	72.5	80	420	440	460	2000	2500	3000

Chapter 3. Randomly Oriented KLA, Bio-KLA and Their CNFs

3.1. Random Untreated KLA

Effect of flow rate and collection time on fiber diameter was investigated for the electrospinning of random KLA fibers. The spinnability test was conducted for 63 combinations of solution properties. Optimization was conducted on three parameters, including electric field, lignin/PEO ratio, and MW of PEO. Characterization of the mechanical properties and the fiber diameter was performed for different combinations of these three parameters. Untreated KLA and Bio-KLA were electrospun into random fibers under the optimized condition and subsequently carbonized into CNFs. Their mechanical properties and fiber diameter are reported.

3.1.1. Effect of Flow Rate & Electric Field

An optimized flow rate was identified at around 420 nl/s where a stable Taylor cone shape was formed. As shown in Figure 3.1, flow rate of 450 nl/s and above induced fiber fusion. High flow rate caused incomplete solvent evaporation, therefore the partial solidified fibers merged at junctions. Fibers exhibited bead-free and uniform morphology at flow rate of 400 nl/s and 420 nl/s.

As shown in Figure 3.2, for flow rates higher than 420 nl/s, the fiber diameter increased due to insufficient electric field strength to elongate the solution. Similar trend was observed by Megelski et al. for as-spun polystyrene fibers and Zargham et al. for as-spun Nylon 6 fibers[130,154]. However, further increase in flow rate to greater than 450 nl/s did not induce more variation in the fiber diameter. Baumgarten and Inagaki et al. both considered the effect of flow rate on fiber diameters to be inapparent[155,156]. Zargham et al. reported higher flow rate caused wider deviations in the distribution of fiber diameters[130]. In the current study, a twofold increase was observed in standard deviation of fiber diameter for flow rate higher than 420 nl/s in comparison to flow rate at 420 nl/s. In general, there was no clear trend between fiber diameter and flow rate.
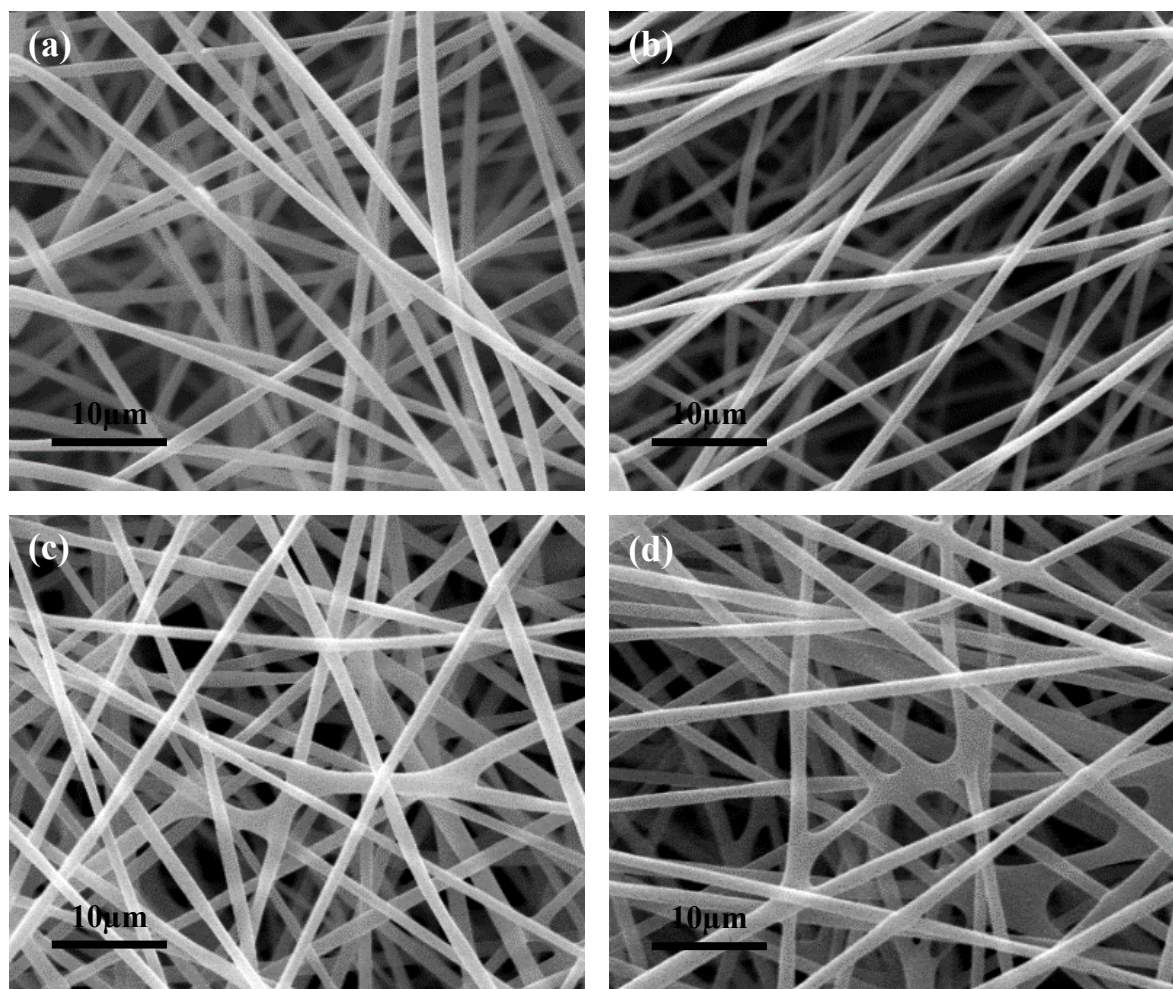
Figure 3.1. SEM images for KLA-R collected at flow rate of (a) 400 nl/s, (b) 420 nl/s, (c) 450 nl/s, (d) 500 nl/s, with PEO MW of 1000 kDa, lignin/PEO ratio of 96/4, solid concentration of 22 wt%, and collection time of 30 min.
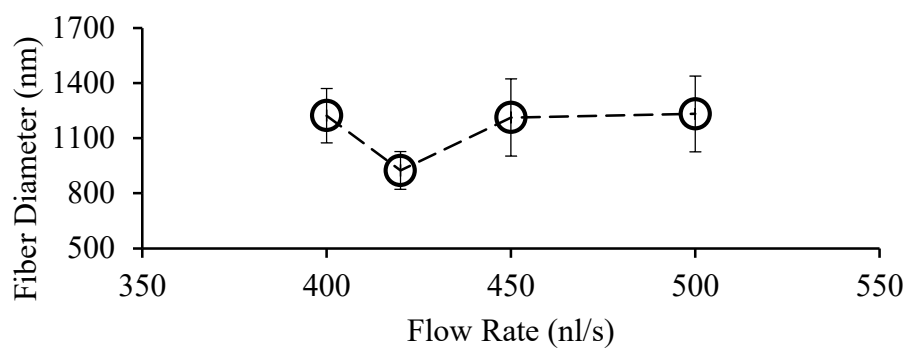
Figure 3.2. Average fiber diameter versus flow rate at PEO MW of 1000 kDa, lignin/PEO ratio of 96/4, solid concentration of 22 wt%, and collection time of 30 min.

Fridrikh et al. developed a method to estimate jet diameter in electrospinning[157]. The method was based on the assumptions that the solution was a Newtonian fluid, while elastic effects and evaporation of the solution were negligible. Rutledge and Fridrikh improved the method to consider that the jet reached asymptotic regime when the distance from the spinneret to the collector was more than 30 times the inside diameter of the needle. Fiber diameter D was estimated from solution density ρ_s, applied electric field strength F_∞, flow rate Q, current I, and axial coordinate z by[123],

$$ D = \left(\frac{Q^3 \rho_s}{2\pi^2 F_\infty I} \right)^{\frac{1}{4}} z^{-\frac{1}{4}} \tag{[3.1]} $$

The experimental data was compared to the model in equation [3.1]. The model predicted the fiber diameter to be directly proportional to the flow rate raised to the power of 3/4 assuming other parameters were constant. The axial distance was 20 cm from the needle tip to the collector. The solution density was consistent but the current (<1 μA) was too low to be captured by the voltage supplier. Fiber diameter is plotted in terms of electric field in Figure 3.3. Both the experimental data and the model concluded a negative relationship between fiber diameter and electric field. The curve fitting suggested that average fiber diameter was approximately proportional to electric field to the power of -9/10 instead of -1/4 indicated by Rutledge and Fridrikh's model. Nevertheless, the standard deviation in fiber diameter was too large to conduct curve fitting with statistical significance.
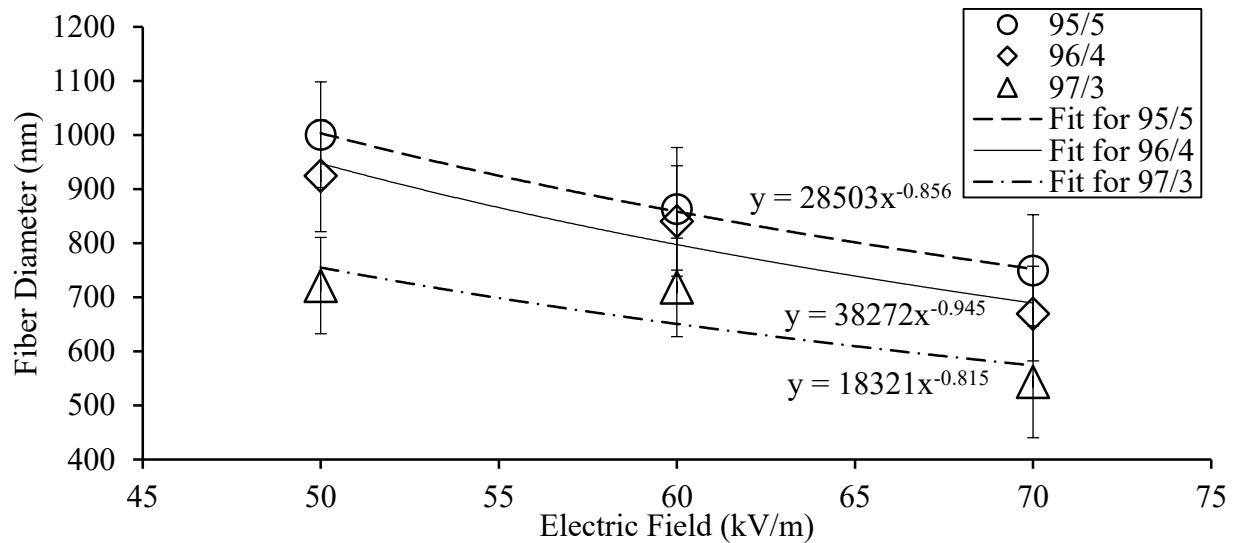
Figure 3.3. Average fiber diameter versus electric field at solid concentration of 22 wt%, PEO MW of 1000 kDa, flow rate of 420 nl/s and collection time of 30 min.

3.1.2. Effect of Collection Time

KLA-R were collected for different durations. The average fiber diameter versus collection time is shown in Figure 3.4. There was no apparent relationship observed between fiber diameter and collection time. Katta et al. reported that fiber diameter increased with collection time due to reduction in electric strength as the thickness of the fiber mat increased[99]. The range of collection time investigated here might be too short to trigger the effect of collection time on fiber diameter.
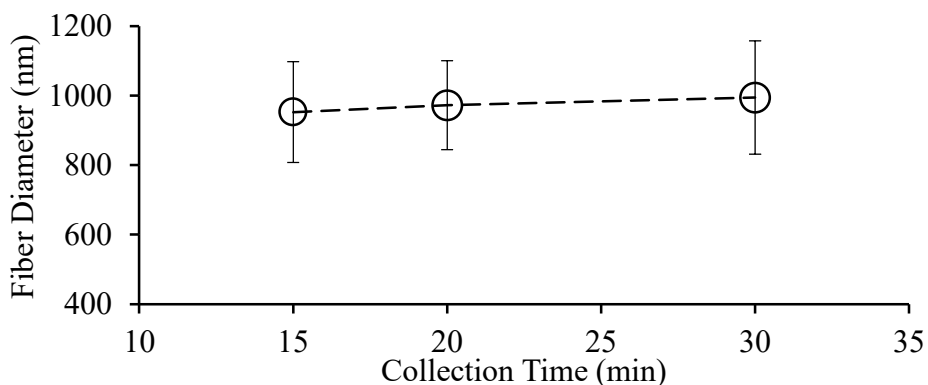
Figure 3.4. Average fiber diameter versus collection time at PEO MW of 1000 kDa, lignin/PEO ratio of 96/4, solid concentration of 22 wt%, flow rate of 450 nl/s and electric field of 45.5 kV/m.

3.1.3. Effect of Preheating

As shown in Figure 3.5, preheating to 60 °C demonstrated substantial effect on reducing the average fiber diameter. However, since the heating profile of the solution could not be maintained constant, preheating was not applied unless the spinnability of the solution was an issue.
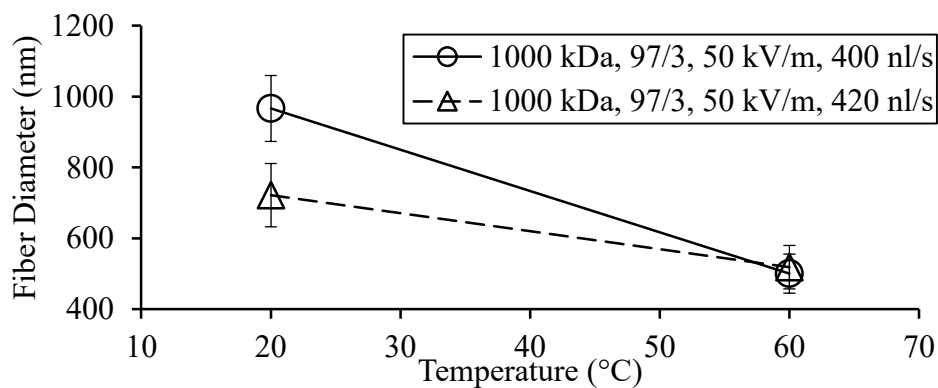
Figure 3.5. Average fiber diameter versus preheating temperature at PEO MW of 1000 kDa, lignin/PEO ratio of 97/3, solid concentration of 22 wt% and electric field of 50 kV/m.

3.1.4. Effect of Voltage & Distance

As shown in Figure 3.6, fiber diameter was inversely correlated to the applied voltage. Higher electric field elongated the jet into finer fibers. The average fiber diameter versus tip-to-collector distance is illustrated in Figure 3.7, which either showed positive or no correlation to change in distance.
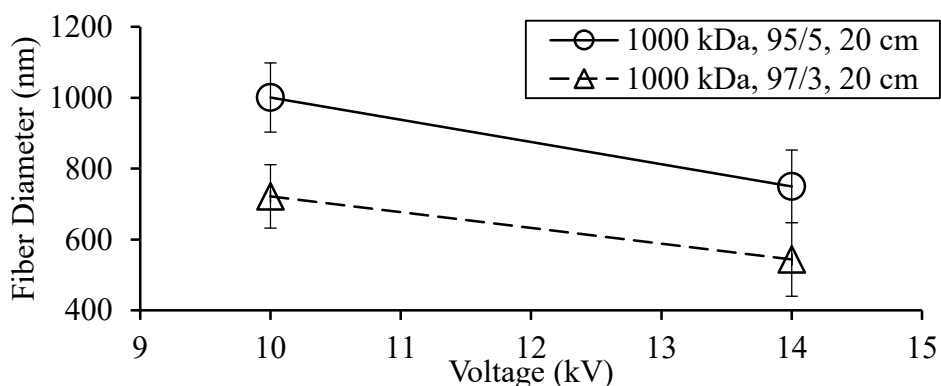
Figure 3.6. Average fiber diameter versus applied voltage at PEO MW of 1000 kDa, flow rate of 420 nl/s, distance of 20 cm, and solid concentration of 22 wt%.
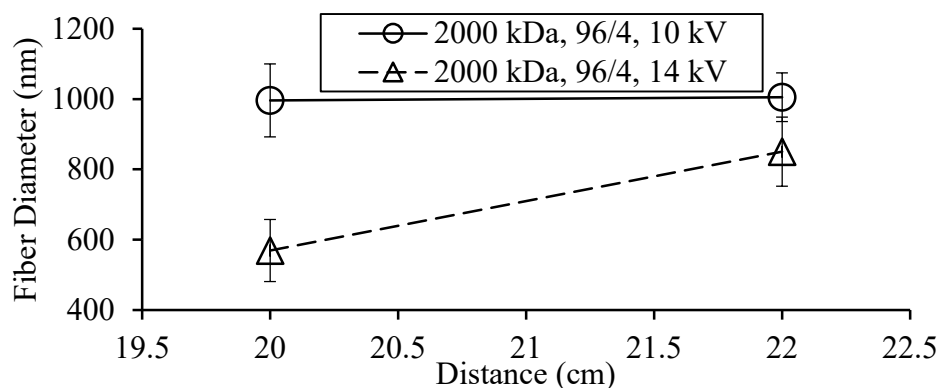
Figure 3.7. Average fiber diameter versus distance at PEO MW of 2000 kDa, flow rate of 420 nl/s, lignin/PEO ratio of 96/4 and solid concentration of 22 wt%.

3.1.5. Fiber Morphology

Different fiber morphologies for KLA-R are shown in Figure 3.8. Uniform, cylindrical and smooth fibers (Figure 3.8a) were observed at solid concentration of 22 wt%. Ribbon-like fibers with inconsistent diameter were flat and twisted at solid concentration of 30 wt% (Figure 3.8b) and 35 wt% (Figure 3.8c). The ribbon shape was due to the inability to maintain circular cross section when sudden evaporation of solvent trapped inside fibers took place. It mostly occurs when solution shows low relaxation time[131].

The typical defects detected in fiber morphologies including BOAS, fusion, porous mat, and branching are depicted in Figure 3.9. Continuous spinning, dripping, and electrospraying occurred during the electrospinning process. Dripping reduced the thickness of the collected fiber mat. It was caused by loss of Taylor cone shape, deficient solution discharge, or lacking of electric field to elongate solution into jet form. Electrospraying led to deposition of solution with trapped solvent on the collector or porous fiber mats (Figure 3.9f). If the nozzle was not cleaned frequently, the rapid evaporation of the solvent at the nozzle due to low RH increased the solid concentration at the tip. As a result, the solution partially solidified and obstructed the discharge. Removal of the agglomeration either manually or via electric field induced abrupt ejection of a large volume of solution, resulting in temporary electrospraying. The temporary electrospraying generated micro- or macro-scale pits on the fiber mats. The pits might be covered by uniform fibers as new layers formed on top. Therefore, certain fiber mats showed no defects on the front surface, but exhibited porous structure underneath. The defect-free fiber mats (Figure 3.8d) could be obtained when electrospraying did not occur.

BOAS structures (Figure 3.9a) formed at high MW of PEO and low solid concentration. Previous study indicates BOAS structures can be reduced or eliminated by increasing PEO fraction, but increasing MW of PEO alone does not cause change in morphology due to insufficient chain entanglement[152]. Lack of bonding between PEO and lignin produced defective fiber mats. Porous beads with unsmoothed surface appeared typically at PEO MW of 2000 kDa or 5000 kDa in different forms, including particle-like form (Figure 3.9b), lump form (Figure 3.9c), and toroid form (Figure 3.9d). Beads tend to form based on minimal surface energy principle[117], and can be induced by low solution viscosity or low net charge density[118]. At the same total solid concentration, decrease in PEO fraction decreased the viscosity of the solution, which could promote bead generation. As the beads with trapped solvent formed at the collector, the rapid evaporation of the solvent caused the drying polymer skin to collapse into irregular shapes[158]. Fiber fusion was observed for some cases at solid concentration of 22 wt% (Figure 3.9e). As the fibers overlapped, the trapped solvents caused the fibers to merge at the contact point and created a network of fused fiber. Fiber branching (Figure 3.9d) was another defect with physical characteristics similar to fiber fusion but different mechanism. The main jet branches into sub-jets with smaller diameters to decrease the local electric charge[119]. Due to instability of the jet, the sub-jets were observed to be frizzy and curved.
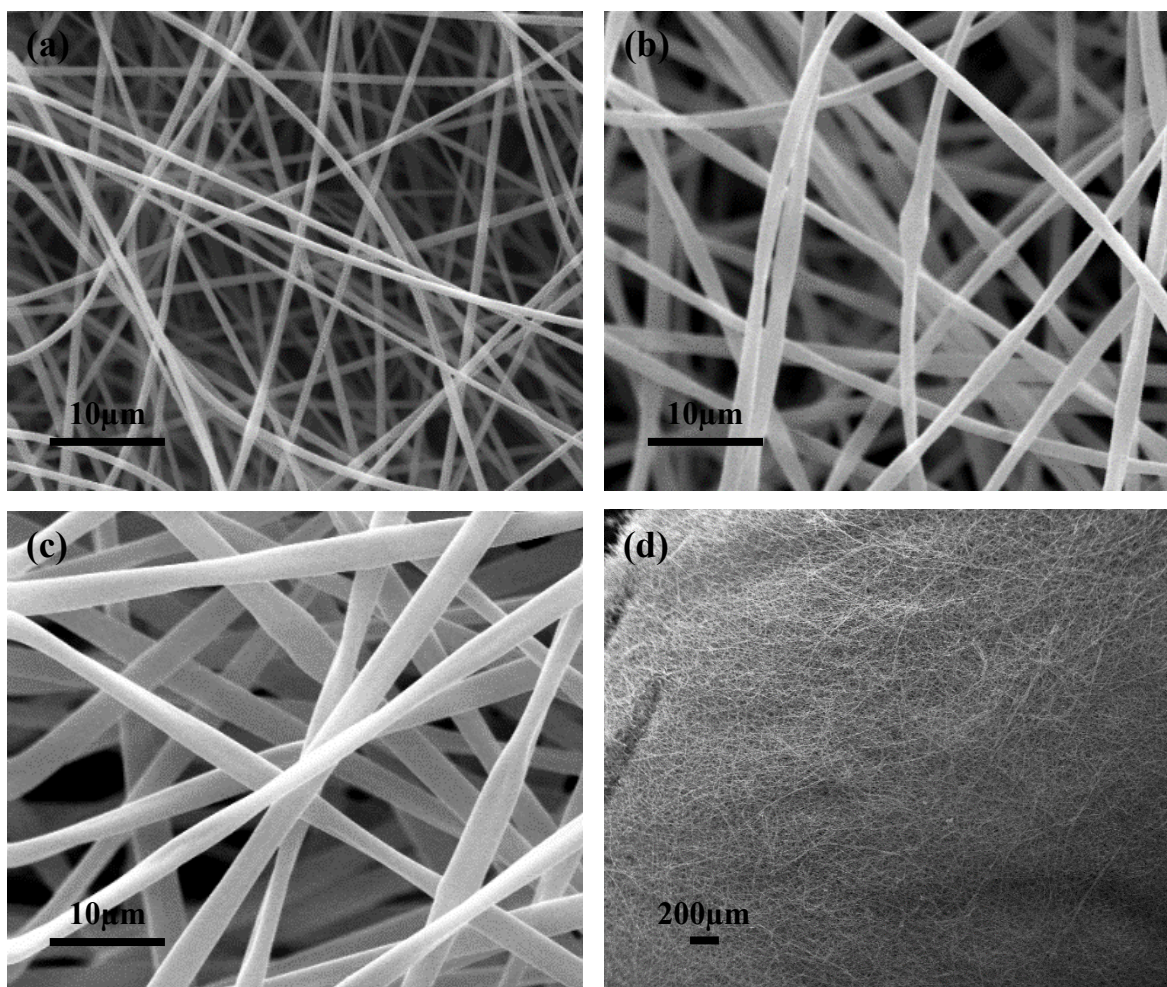
Figure 3.8. Morphologies of (a) smooth fibers electrospun from total solid concentration of 22 wt%, (b) ribbon-like fibers from total solid concentration of 30 wt% and (c) 35 wt%, and (d) defect-free fiber mat.
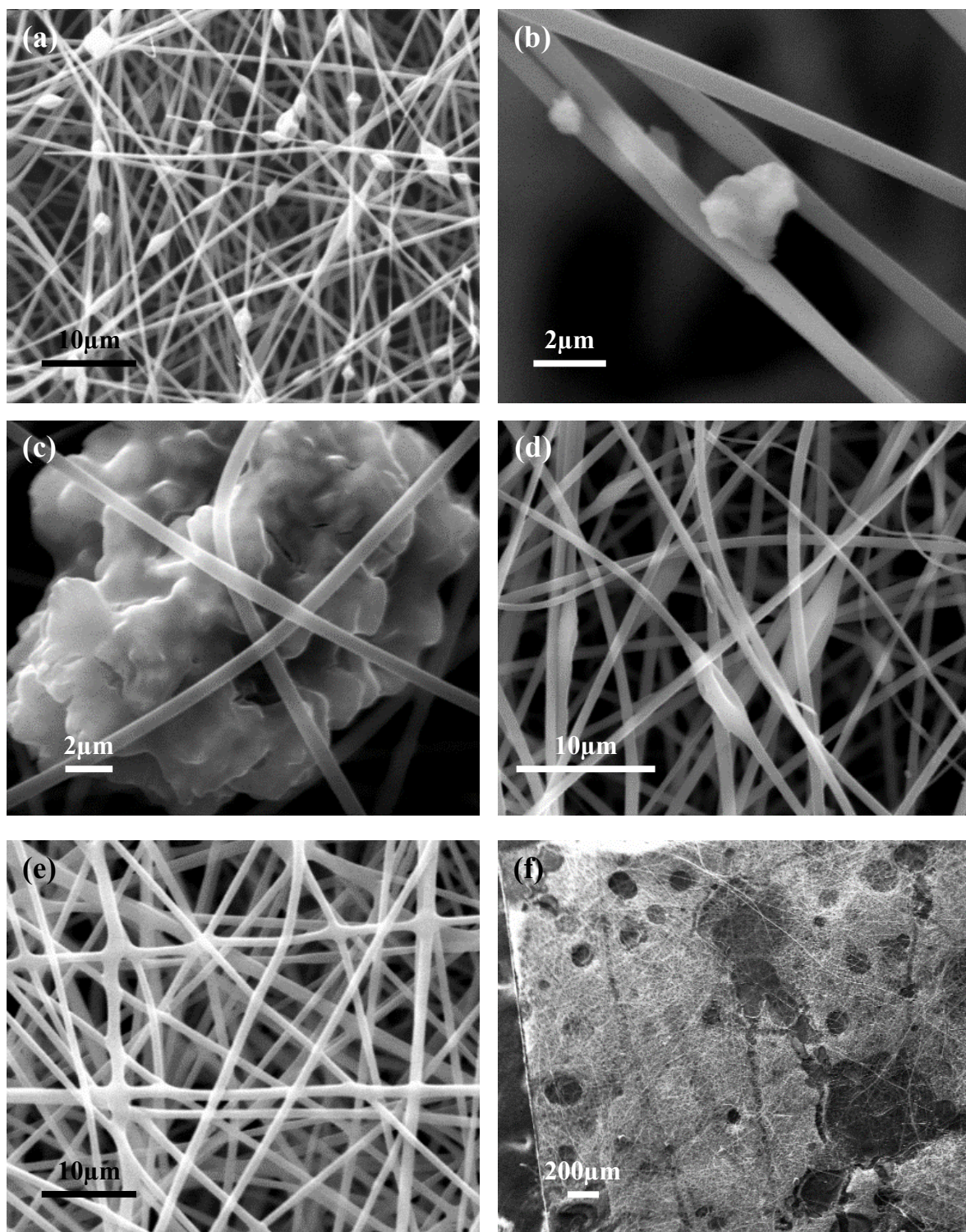
Figure 3.9. Morphologies of fiber defects exhibited at total solid concentration of 22 wt%, including (a) BOAS structure at PEO MW of 5000 kDa, lignin/PEO ratio of 95/5, electric field of 70 kV/m, (b) particle-like bead at PEO MW of 2000 kDa, lignin/PEO ratio of 95/5, electric field of 50 kV/m, (c) porous bead at PEO MW of 2000 kDa, lignin/PEO ratio of 95/5, electric field of

50 kV/m, (d) toroid bead and branched fibers at PEO MW of 2000 kDa, lignin/PEO ratio of 95/5, electric field of 60 kV/m, (e) fiber fusion at PEO MW of 5000 kDa, lignin/PEO ratio of 97/3, electric field of 60 kV/m, and (f) electrosprayed fiber mat at PEO MW of 2000 kDa, lignin/PEO ratio of 97/3, electric field of 60 kV/m.

3.1.6. Spinnability Test

Spinnability is the capability of polymer solution to be spun into fibers via electrospinning. Spinnability under different solution properties was tested for random fibers as listed in Table 3.1. The color bar corresponds to different spinning behaviors. Spinnable and testable conditions were marked green, under which fiber mats were uniform and removable from the aluminum foil. These fiber mats were later characterized by tensile test. Solutions that were spinnable typically showed viscoelastic characteristics (Figure 3.10a), and were observed for lignin/PEO ratio of 95/5-97/3, PEO MW of 1000-5000 kDa, and solid concentration of 22 wt%. Spinnable cases also occurred selectively for high lignin fraction at solid concentration of 30-35 wt%.

Spinnable but brittle fiber mats with a thick layer were marked orange in Table 3.1. These fiber mats were golden, cracked, and naturally fell off from the aluminum foil. This physical appearance of fiber mat was observed when the solution transitioned from non-spinnable to spinnable at solid concentration of 30 wt% and higher. The golden color (Figure 3.11a) demonstrated incomplete evaporation of solvent.

Spinnable but brittle fiber mats with a thin layer were marked yellow in Table 3.1. The fibers formed a thin layer with light yellow color (Figure 3.11b) on the aluminum foil, and could not be peeled off for tensile testing. This spinning scenario occurred at high lignin fraction for solid concentration of 22 wt% and 30 wt%. It could be possible that the solvent evaporated too rapidly to result in brittle fibers. It was also challenging for the solution to maintain the jet form due to low PEO fraction. Insufficient PEO concentration resulted in solution with low viscosity and poor viscoelasticity, and thus low fiber deposition.

Non-spinnable test conditions were marked red. They mostly occurred for total solid concentration of 30 wt% and 35 wt%. Under these conditions, the solution was either electrospraying as shown in Figure 3.10b or incapable of forming jet. The high fraction of PEO caused high solution viscosity[129], and the electric field was incapable of opposing the viscous force. The spinning condition marked with two colors indicated multiple spinning behaviors on the same fiber mat.

A diagonal trend was observed for the change in spinnability behavior (Table 3.1). Higher lignin concentration increased fiber brittleness at 22 wt%. At 30 wt% and 35 wt%, solution at low lignin fraction (high PEO fraction) was not spinnable. Solution at high PEO MW (5000 kDa) was either not spinnable or producing brittle fiber mats. As total solid concentration increased, successful spinning could be achieved at higher lignin/PEO ratio. Higher MW and fraction of PEO prolong the relaxation time and increase the viscosity of the solution[120]. But, if MW of PEO and PEO fraction were both too high, the solution was too viscous to be spun. For the same total solid concentration, as MW of PEO increased, smaller fraction of PEO was required to produce uniform fibers. However, reduction in PEO fraction below certain threshold could produce brittle fibers, as indicated in the yellow region in Table 3.1.

Table 3.1. Spinnability for solution with various concentrations and electrospinning parameters

Total Solid Concentration / Molecular Weight of PEO / Lignin/PEO ratio	22 wt%			30 wt%			35wt%		
	1000 kDa	2000 kDa	5000 kDa	1000 kDa	2000 kDa	5000 kDa	1000 kDa	2000 kDa	5000 kDa
95/5	green	green	green	red	red	red	red	red	red
96/4	green	green	green	red	red	red	red	red	red
97/3	green	green	green	red	red	red	red	red	red
99/1	yellow	yellow	yellow	orange/red	red	red	red	red	red
99.5/0.5	yellow	yellow	yellow	green	green	red	green/red	red	red
99.75/0.25	yellow	yellow	yellow	green	orange/yellow	red	green	orange	red
99.9/0.1	yellow	yellow	yellow	green	yellow	orange/yellow	orange	orange/green	green/red

spinnable and testable	green	spinnable but brittle (thin)	yellow	spinnable but brittle (thick)	orange	not spinnable	red
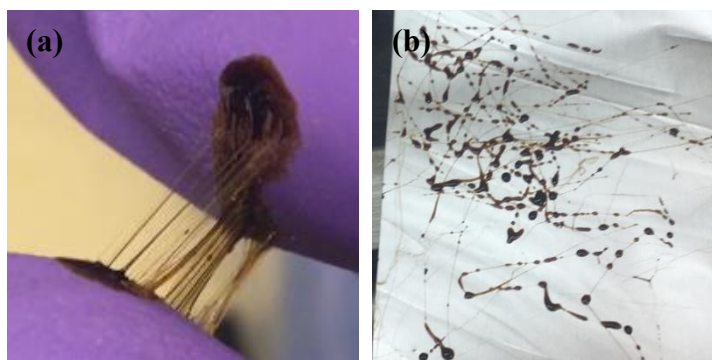
Figure 3.10. Solution showing (a) viscoelastic characteristics and (b) complete electrospraying at high viscosity.
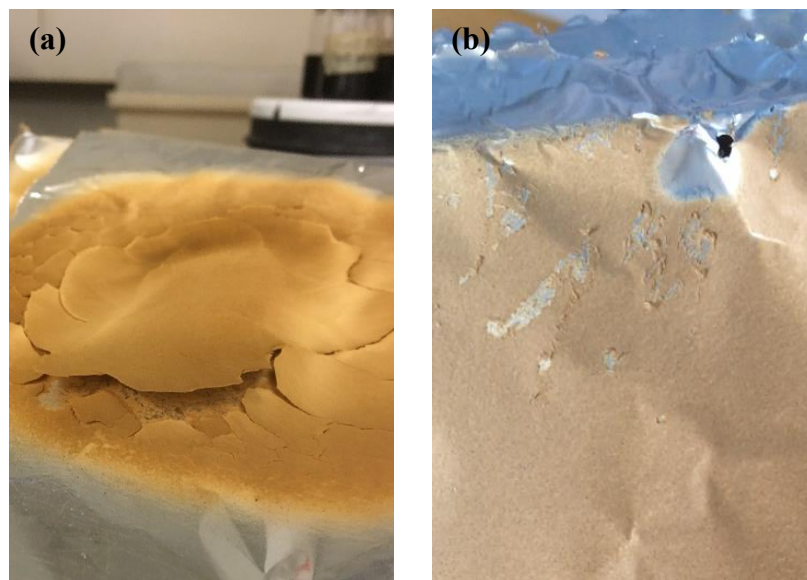
Figure 3.11. Appearance of (a) brittle KLA-R with a thick layer and (b) brittle KLA-R with a thin layer.

3.1.7. Mechanical Properties

Stress-strain curves obtained from the tensile tests were used to acquire the mechanical properties of KLA-R. Elastic modulus was measured as the slope of linear elastic region of the strain-strain curve. Strain at failure was determined as the stress reduced below 0.1 MPa. Tensile strength, elastic modulus, strain at failure and fiber diameter of KLA-R with solid concentration of 22 wt% are summarized in Figure 3.12. Tensile strength did not show a clear trend with change in parameters (Figure 3.12a). Highest tensile strength was 3.66±0.74 MPa, obtained at PEO MW of 2000 kDa, lignin/PEO ratio of 96/4, and electric field of 70 kV/m. The fiber morphology for that parameter combination was uniform with few beads and no fusion. The lowest tensile strength was 0.84±0.29 MPa, more than three times lower than the highest tensile strength. Similar lack of correlation was found between elastic modulus and the parameters (Figure 3.12b). Over 60% of the fiber mats exhibited no change or slight increment in tensile strength and elastic modulus when the electric field was increased from 50 kV/m to 60 kV/m. Tensile strength and elastic modulus reduced at electric field of 70 kV/m due to electrospraying at high voltage. No clear relationship was observed between strain at failure and the parameters (Figure 3.12c). Most KLA-R showed ductile fracture. Fiber diameter showed a negative correlation to electric field (Figure 3.12d). As electric field increased, the strengthened electrostatic force reduced the average fiber diameter. Tensile strength is plotted against average fiber diameter in Figure 3.13a. Although the standard

deviation was high, high tensile strength was generally observed at small fiber diameter (<600 nm). Finer fiber improves molecular orientation and crystallinity[159]. Consequently, tensile strength of the mats with smaller fiber diameter was enhanced. However, no correlation was found between fiber diameter and elastic modulus (Figure 3.13b).
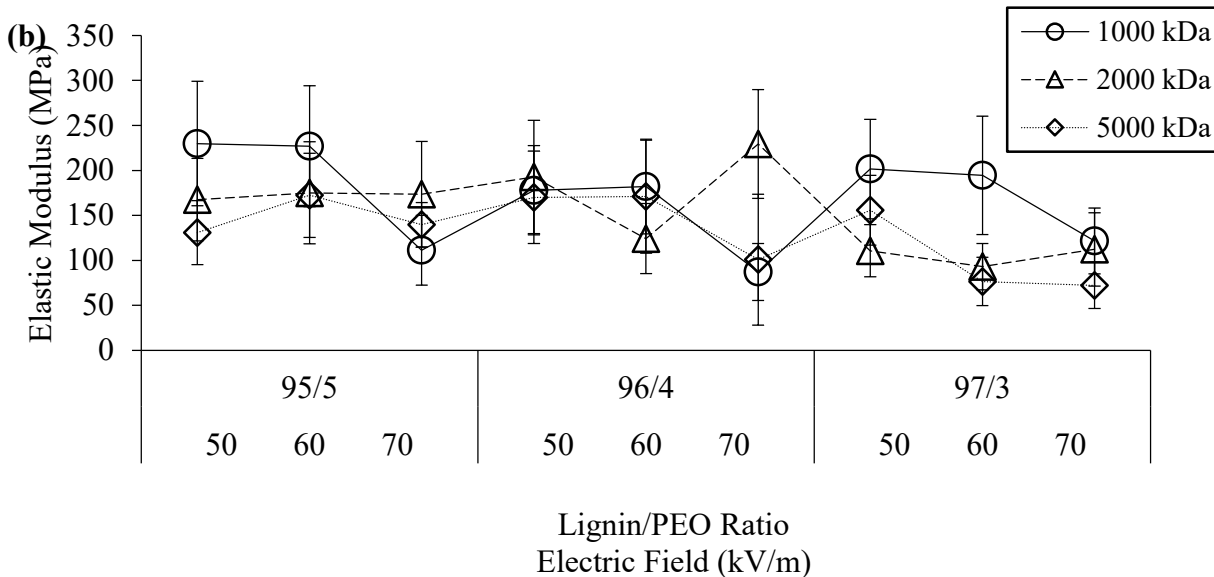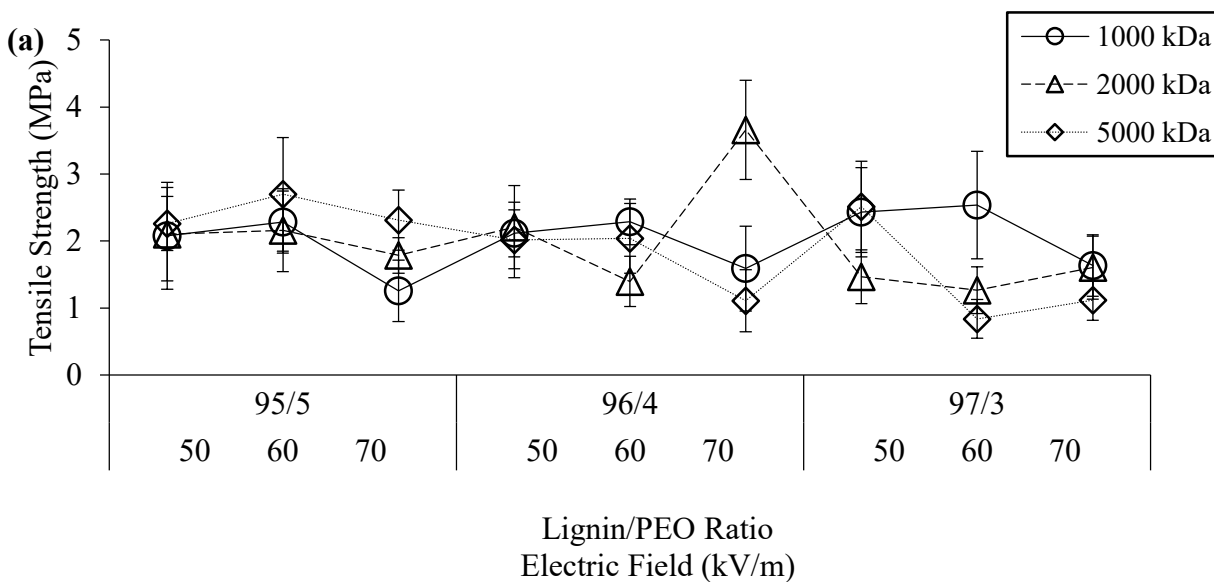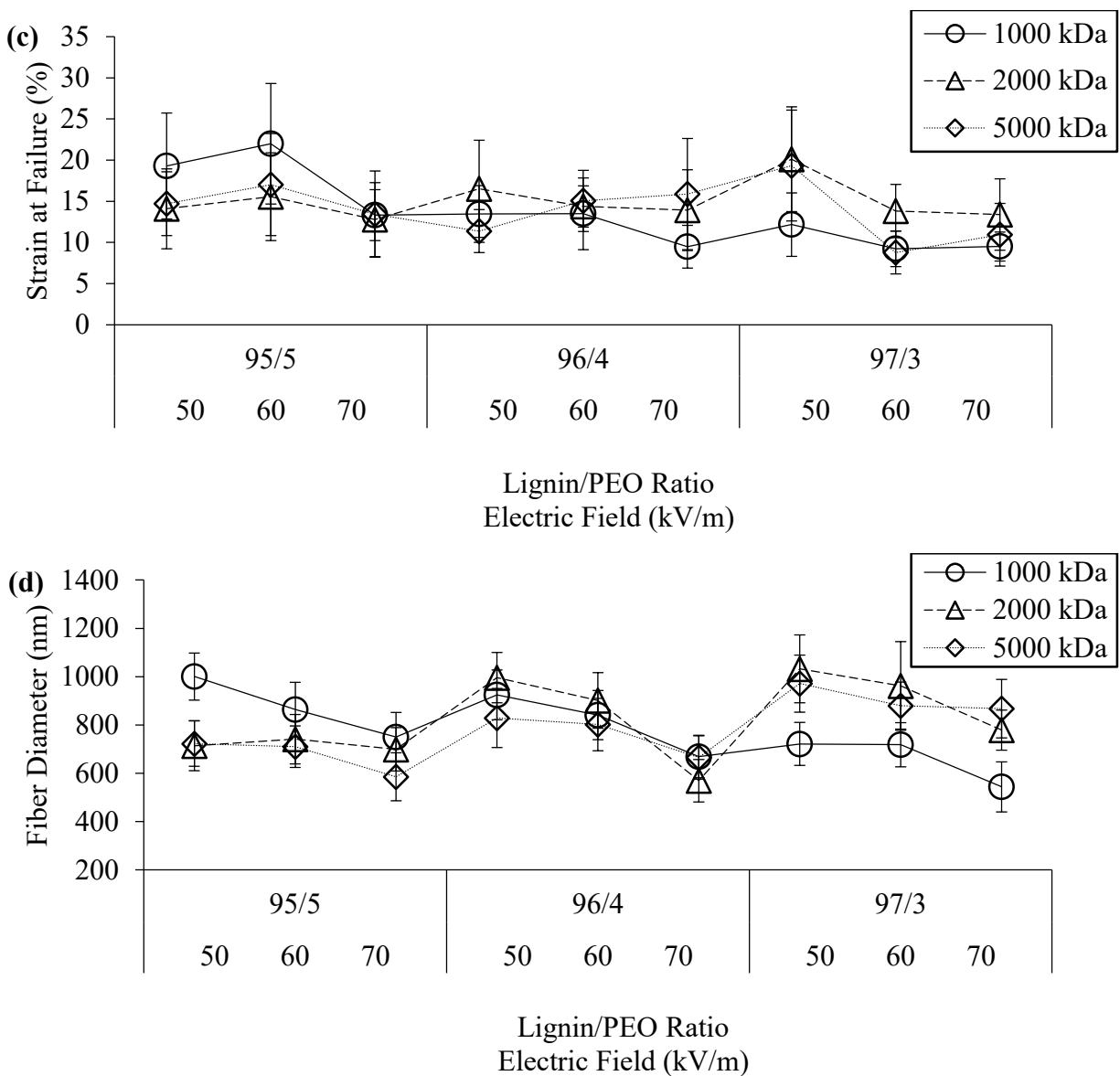
Figure 3.12. Plots of (a) tensile strength, (b) elastic modulus, (c) strain at failure, and (d) average fiber diameter of KLA-R for lignin/PEO ratio of 95/5-97/3, electric field of 50-70kV/m, PEO MW of 1000-5000 kDa, and total solid concentration of 22 wt%.
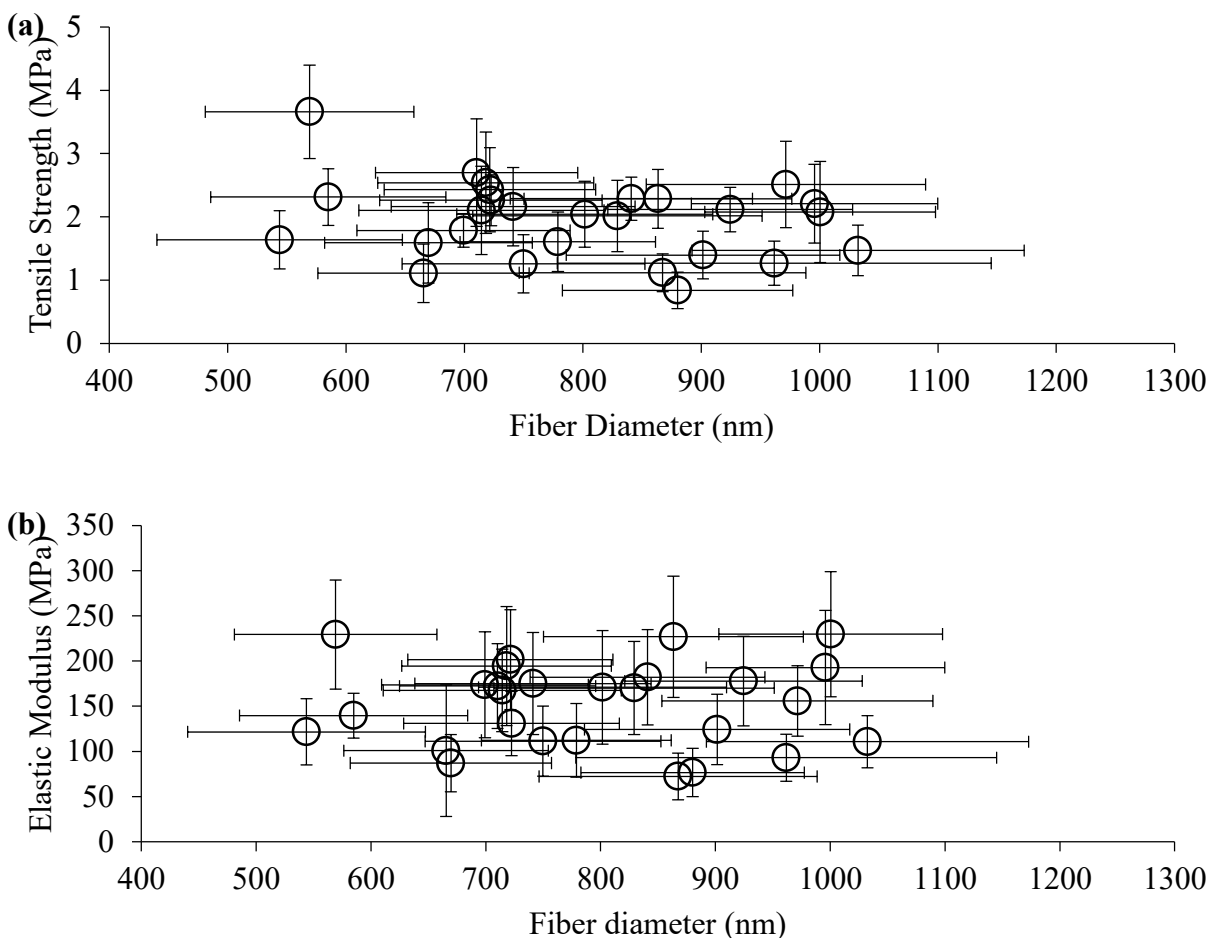
Figure 3.13. Effect of average fiber diameter on (a) tensile strength and (b) elastic modulus of fiber mats electrospun at solid concentration of 22 wt%.

3.1.8. Optimization Analysis

Since correlation shown in previous section was inconspicuous, the parameters were input into Design Expert® for further analysis. Good mechanical properties were mostly obtained at the intermediate level for the parameters investigated in previous section. Therefore, in order not to sacrifice any data, all 27 experimental runs were used for the optimization. Even though this experimental design may not be as efficient as other methods, such as 2-level factorial design or central composite design (CCD), it provided better estimation to the curvature of the correlation model.

The design matrix of the parameters and the responses are listed in Table 3.2. The parameters are shown in coded values. The responses, fiber diameter (D), elastic modulus (E), and tensile strength (σ), are displayed in actual data.

Table 3.2. Design matrix of independent variables in coded values (subscript c) and the corresponding responses in actual values (subscript a) for KLA-R

Test Run	Coded Variables			Responses		
	$(F_\infty)_c$	$(r_{L/P})_c$	W_c	D_a (nm)	E_a (MPa)	σ_a (MPa)
1	-1	-1	-1	1000.48	229.79	2.08
2	0	-1	-1	863.47	226.83	2.29
3	1	-1	-1	749.85	111.30	1.26
4	-1	0	-1	924.51	177.87	2.12
5	0	0	-1	840.95	182.08	2.29
6	1	0	-1	669.59	87.11	1.59
7	-1	1	-1	721.45	201.56	2.43
8	0	1	-1	718.09	194.59	2.54
9	1	1	-1	543.86	121.64	1.64
10	-1	-1	0	714.36	167.53	2.10
11	0	-1	0	741.10	175.11	2.16
12	1	-1	0	699.23	173.62	1.79
13	-1	0	0	995.82	192.75	2.21
14	0	0	0	901.54	124.26	1.40
15	1	0	0	569.21	229.35	3.66
16	-1	1	0	1022.08	110.71	1.47
17	0	1	0	961.74	93.02	1.27
18	1	1	0	778.89	112.21	1.60
19	-1	-1	1	722.42	130.88	2.26
20	0	-1	1	710.23	172.32	2.70
21	1	-1	1	584.93	139.66	2.31
22	-1	0	1	829.21	170.16	2.01
23	0	0	1	801.67	170.93	2.04
24	1	0	1	665.41	100.83	1.11
25	-1	1	1	971.57	155.77	2.51
26	0	1	1	880.11	76.56	0.84
27	1	1	1	867.48	72.30	1.12

Four models are evaluated in Table 3.3, with the recommended model highlighted. Aliased structure was detected for cubic model, so cubic model was not considered for optimization. Sequential p-value lower than 0.05 indicated that adding the term was significant to the model. For example, if sequential p-value was low for the quadratic model, the addition of quadratic term made the model provide better estimation. R^2 explained how well the model explained the variation in dependent responses based on independent parameters. But it was biased since it increased when more parameters were added to the model, no matter if the parameters were relevant. Therefore, R^2 was not included. Adjusted and predicted R^2 were used instead to evaluate the models. Adjusted R^2 signified how well the data fitted the model, adjusted for the number of parameters. Small adjusted R^2 implied the model was not suitable as the parameters that had insignificant correlation to the response were added to the model. Predicted R^2 entailed if the model could make valid prediction for new data. The difference between adjusted and predicted R^2 should be smaller than 0.2 for the model to be reliable.

For fiber diameter, two-factor-interaction (2FI) model was suggested since its sequential p-value was lower than 0.05, while adjusted and predicted R^2 were higher than other models. The linear model was recommended for elastic modulus due to the low p-value, high adjusted and predicted R^2. For both fiber diameter and elastic modulus, adjusted and predicted R^2 were in compliance with each other (difference<0.2). For tensile strength, sequential p-value was higher than 0.05. Adjusted and predicted R^2 were both low with difference larger than 0.2. It could be concluded that the parameters had negligible effect on tensile strength so tensile strength was removed from the model analysis for further optimization. The prediction equations are populated for fiber diameter and elastic modulus in both coded and actual values in Table 3.4, which specify the correlation between the responses and the parameters.

Table 3.3. Models recommended for each response of KLA-R

Response	Source	Sequential p-value	Adjusted R^2	Predicted R^2	Remarks
D	Linear	0.0050	0.3460	0.1736	
	2FI	**0.0158**	**0.5463**	**0.3738**	**Suggested**
	Quadratic	0.5038	0.5332	0.2344	
	Cubic	0.0275	0.7845	0.1812	Aliased
E	**Linear**	**0.0069**	**0.3261**	**0.1990**	**Suggested**
	2FI	0.9273	0.2423	-0.0310	
	Quadratic	0.8483	0.1486	-0.3461	
	Cubic	0.2794	0.2872	-0.4665	Aliased
σ	Linear	0.3179	0.0270	-0.1521	
	2FI	**0.3736**	**0.0391**	**-0.3123**	**Not Significant**
	Quadratic	0.9600	-0.1113	-0.7923	
	Cubic	0.4578	-0.0901	-1.6627	Aliased

Table 3.4. Prediction equation for variables in coded and actual values

Prediction Equation (Coded Value)

D_c = 793.42 - 94.36 $(F_\infty)_c$ + 52.36 $(r_{L/P})_c$ - 5.97 W_c - 10.13 $(F_\infty)_c * (r_{L/P})_c$ + 24.97 $(F_\infty)_c *$ W_c + 87.78 $(r_{L/P})_c * W_c$

E_c = 148.90 - 21.61 $(F_\infty)_c$ - 21.59 $(r_{L/P})_c$ - 17.91 W_c

Prediction Equation (Actual Value)

D_a = 3369.60 + 84.11 $(F_\infty)_a$ -18.50 $(r_{L/P})_a$ - 4.29 W_a - 1.01 $(F_\infty)_a * (r_{L/P})_a$ + 0.001 $(F_\infty)_a$ $* W_a$ + 0.04 $(r_{L/P})_a * W_a$

E_a = 2378.32 - 2.16 $(F_\infty)_a$ - 21.59 $(r_{L/P})_a$ - 0.01 W_a

The recommended models for fiber diameter and elastic modulus were analyzed with analysis of variance (ANOVA) in Table 3.5 and Table 3.6. F-value and p-value suggested if the model or the parameter was significant to the response with confidence level of 95%. The 2FI model for fiber diameter and the linear model for elastic modulus were both significant (p-

value<0.05). Adequate precision (signal-to-noise ratio) higher than 4 suggested that the effect of the parameters could be distinguished from noise.

In the ANOVA analysis for fiber diameter, the main effect of F_∞ showed the highest significance (p-value<0.05), followed by interaction effect $r_{L/P}*W$ between lignin/PEO ratio and MW of PEO (p-value<0.05), and main effect of $r_{L/P}$ (p-value<0.05). The other effects had insignificant correlation to fiber diameter (p-value>0.05). For elastic modulus, the significance of the main effects was ranked as follow: F_∞ (p-value<0.05), $r_{L/P}$ (p-value<0.05), and W (0.05<p-value<0.1).

Table 3.5. ANOVA analysis of model (coded) for fiber diameter

Source	Sum of Squares	Df	Mean Square	F-value	p-value
Model	310562.10	6	51760.35	6.22	0.0008
F_∞	154340.04	1	154340.04	18.54	0.0003
$r_{L/P}$	47525.58	1	47525.58	5.71	0.0269
W	694.29	1	694.29	0.08	0.7757
$F_\infty*r_{L/P}$	1232.50	1	1232.50	0.15	0.7045
$F_\infty*W$	8107.35	1	8107.35	0.97	0.3355
$r_{L/P}*W$	100173.71	1	100173.71	12.03	0.0024
Residual	166513.10	20	8325.651		
Total	477075.20	26			
Std. Dev.	91.25	R^2		0.6510	
Mean	794.42	Adjusted R^2		0.5463	
C.V. %	11.49	Predicted R^2		0.3738	
		Adeq Precision		9.0200	

Table 3.6. ANOVA analysis of model (coded) for elastic modulus

Source	Sum of Squares	Df	Mean Square	F-value	p-value
Model	23052.20	3	7684.07	5.19	0.0069
F_∞	8406.41	1	8406.41	5.68	0.0258
$r_{L/P}$	8392.39	1	8392.39	5.67	0.0259
W	6253.40	1	6253.40	4.23	0.0513
Residual	34028.24	23	1479.49		
Total	57080.44	26			
Std. Dev.	38.46		R^2	0.4039	
Mean	151.88		Adjusted R^2	0.3261	
C.V. %	25.33		Predicted R^2	0.1990	
			Adeq. Precision	8.2556	

The validity of the models for fiber diameter and elastic modulus was examined with predicted vs. actual values (Figure 3.14) and residuals vs. predicted response (Figure 3.15). In Figure 3.14, the data were located in close proximity to the straight line where the actual value was equal to the predicted value. Externally studentized residual was displayed in the unit of standard deviation. It implied whether each test run was in agreement with others in the model. If outliers occurred, it showed how many standard deviations the outlier fell from the target value (zero line). Figure 3.15 exhibited no pattern, suggesting that there was no correlation between errors and responses. The upper and lower boundaries representing confidence interval of 95% were used to identify outliers. No outlier was observed beyond the boundaries in the plots. Therefore, the model fitted the data well.
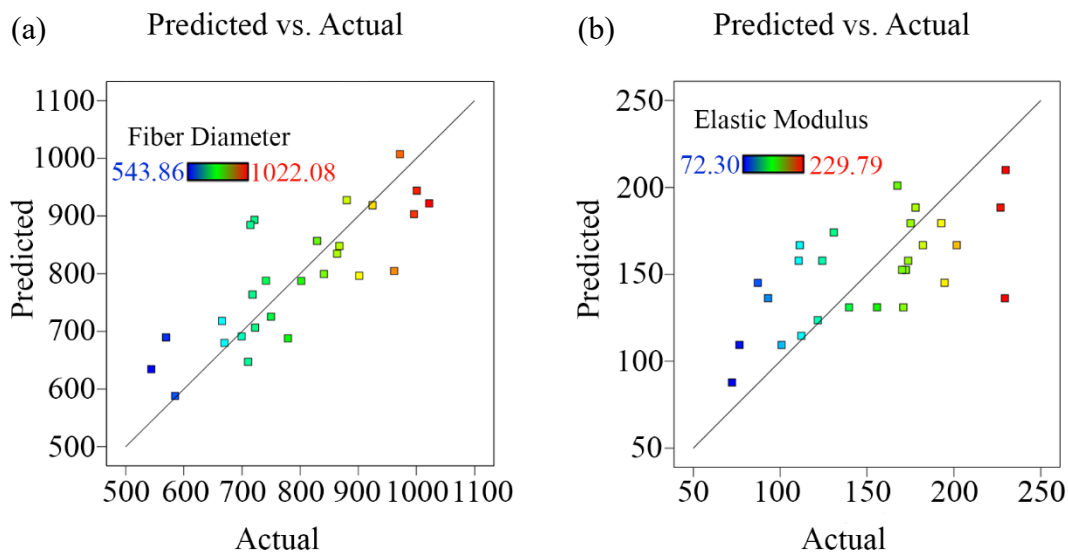
Figure 3.14. Predicted value versus actual value for (a) fiber diameter and (b) elastic modulus.
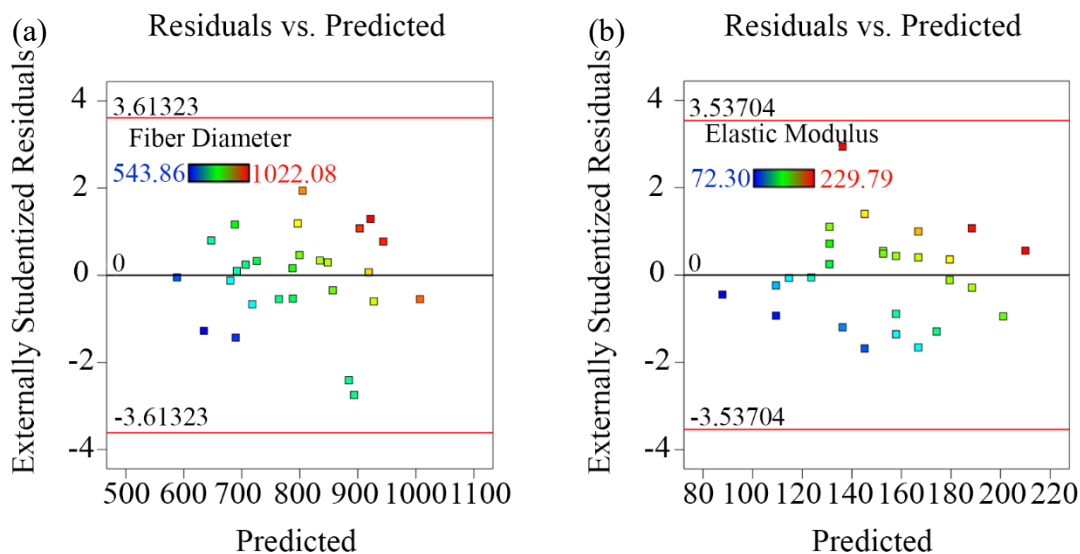
Figure 3.15. Residuals versus predicted value for (a) fiber diameter and (b) elastic modulus.

The main effects of the parameters on the responses predicted from the model with 95% confidence interval are shown in Figure 3.16. Average fiber diameter decreased as electric field increased (Figure 3.16a). Fiber diameter did not reveal an apparent relationship with other parameters. The fraction of PEO might be too small to affect fiber diameter, or the main effects were counteracted due to the interaction effects between $r_{L/P}$ and W. Elastic modulus was also negatively related to F_∞, $r_{L/P}$, and W (Figure 3.16d,e,f). The decrease in elastic modulus could be

driven by decrement in fiber diameter at high electric field, which was reported to reduce the elasticity of the fibers[160]. Poor mechanical properties induced by electrospraying at high electric field also justified this correlation. Even though elastic modulus reduced as W increased, their correlation was not significant as indicated by ANOVA analysis.

The interaction effects for fiber diameter are illustrated with contour plots in Figure 3.17. There was no interaction effect for elastic modulus since linear model was selected. The results of the test runs were marked as red dots on the plots. The interaction effect $F_\infty * r_{L/P}$ was insignificant as the curvature of the contour plot (Figure 3.17a) was not substantial. The interaction effect $F_\infty * W$ was also not evident (Figure 3.17b). Considerably curved plots for interaction $r_{L/P} * W$ (Figure 3.17c) signified notable interactive effect on fiber diameter. The data points on the curves indicated fiber diameter was positively correlated to W and negatively correlated to $r_{L/P}$.
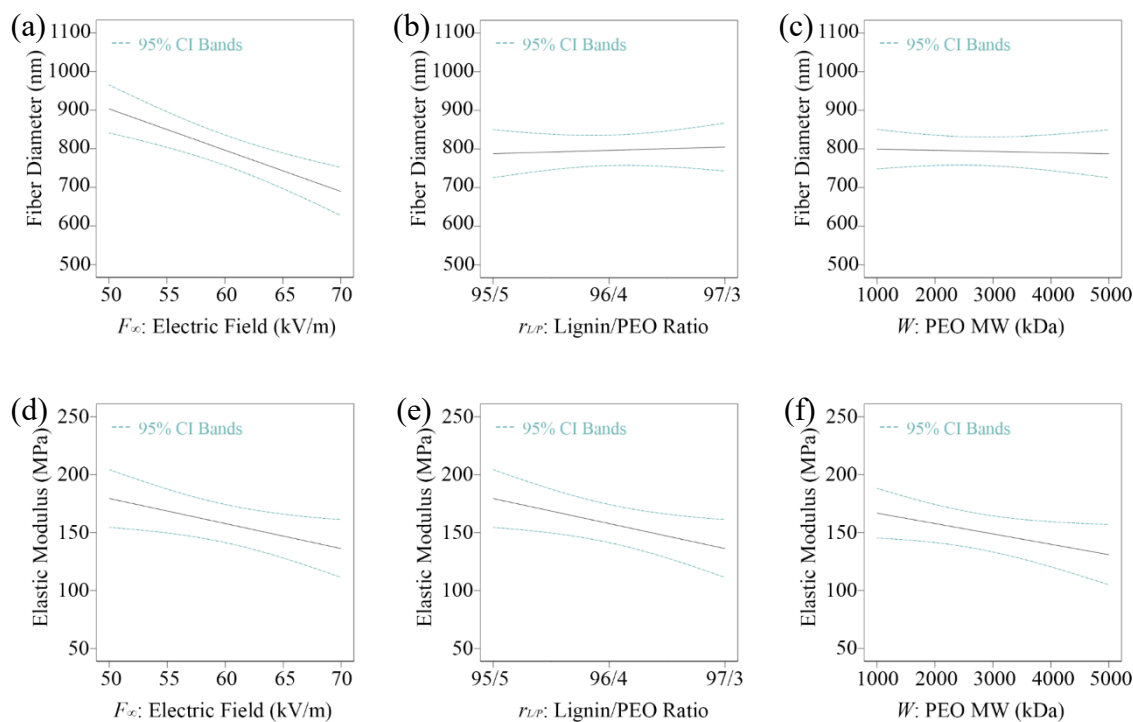
Figure 3.16. Main effects of (a, d) electric field, (b, e) lignin/PEO ratio, and (c, f) MW of PEO on (top) fiber diameter and (bottom) elastic modulus.
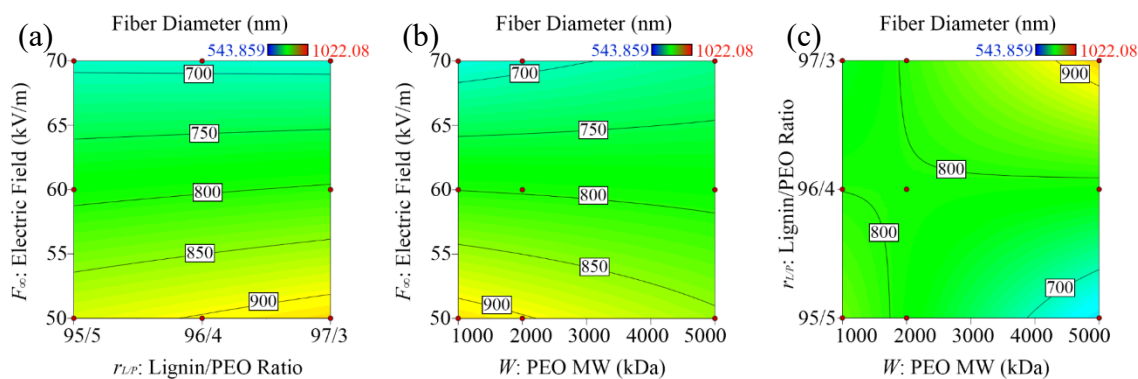
Figure 3.17. Interaction effects between (a) electric field and lignin/PEO ratio, (b) electric field and MW of PEO, (c) lignin/PEO ratio and MW of PEO on fiber diameter.

The limits of parameters and the goals for optimization are listed in Table 3.7. The models were optimized to minimize fiber diameter and maximize elastic modulus. Electric field of 50 kV/m, lignin/PEO ratio of 95/5, MW of PEO of 1000 kDa were recommended as the optimal condition with highest desirability in Table 3.8. Since the optimal condition was at the corner point, parameters lower than the experimental value were tested. Electric field lower than 50 kV/m and lignin/PEO ratio lower than 95/5 could not yield uniform fiber mats at the collector. Consequently, the optimal condition was valid. Predicted fiber diameter was 944 nm and predicted elastic modulus was 210 MPa. In comparison to the experimental data, where fiber diameter was 1000.48±97.48 nm and elastic modulus was 229.79±69.21 MPa (tensile strength was 2.08±0.80 MPa), the predicted responses were close to their experimental values. Thus, the model estimation was adequate.

Table 3.7. Optimization goals and limits of optimization parameters for random fibers

Name	Goal	Lower Limit	Upper Limit	Importance
Electric Field Strength	in range	50	70	3
Lignin/PEO Ratio	in range	95	97	3
PEO MW	in range	1000	5000	3
Elastic Modulus	maximize	200	400	3
Fiber Diameter	minimize	500	1000	3

Table 3.8. Optimal condition for electrospinning condition and solution properties for random fibers

Optimal parameters			Predicted response		Desirability
F_∞	$r_{L/P}$	W	D	E	
50	95/5	1000	944	210	0.075

3.2. Bio-KLA and KLA/Bio-KLA CNFs

Random Bio-KLA was electrospun at the same lignin/PEO ratio and MW of PEO optimized for KLA-R. Since Bio-KLA exhibited dripping and low fiber deposition at electric field of 50 kV/m, the electric field was adjusted to 60 kV/m based on the spinnability of Bio-KLA. Average fiber diameter and mechanical properties were characterized for Bio-KLA-R below. Carbonization was conducted for both KLA and Bio-KLA fibers. The thermostabilized and the carbonized fibers from vacuum-dried KLA are shown in Figure 3.18a and Figure 3.18b. If Bio-KLA was not dried prior to solution preparation, the humidity absorbed after exposing to air resulted in metallic appearance after carbonization (Figure 3.18c). The glassy carbon texture could be in transitional state between carbon fiber and graphitized fiber. Compared to smooth carbon fiber, this glass carbon fiber exhibited lower mass yield and higher brittleness. It could indicate decrease in carbon layer spacing, increase in crystallinity and carbon content. The effect of humidity on production of lignin-based CNF was out of scope in current study and could be investigated in future work.
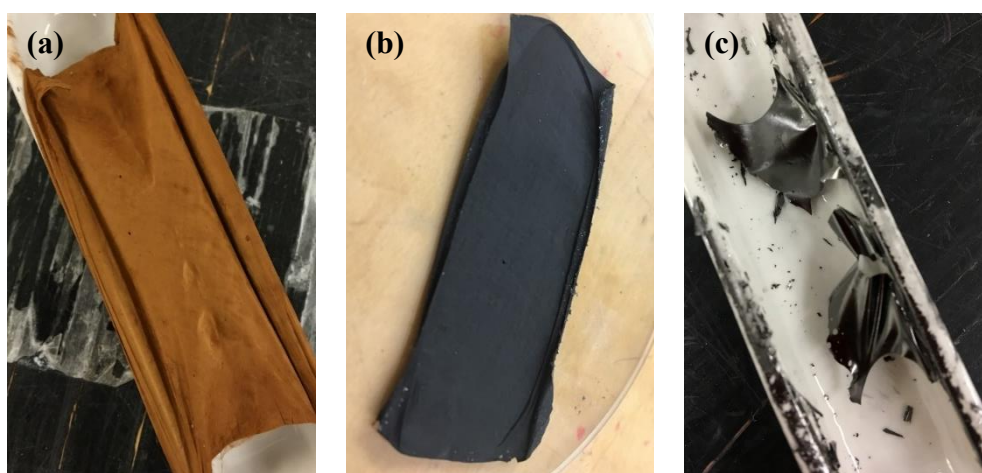
Figure 3.18. Appearance of (a) thermostabilized fibers, (b) smooth CNFs, and (c) glassy CNFs from humidified lignin samples.

3.2.1. Fiber Morphology

The fiber morphologies of random as-spun, thermostabilized, and carbonized untreated KLA and Bio-KLA fiber mats are shown in Figure 3.19. All fibers were uniform, smooth, and defect-free. No beads were detected in the SEM images. Thermostabilization was conducted to prevent fiber fusion in carbonization. Fiber diameter reduced and straight fibers lost shape after thermostabilization. The fibers remained curved after carbonization. Merged fibers were observed after carbonization as a result of increase in mobility of molecular chains at high temperature during thermostabilization before cross-linking took place. No fusion was observed for CNFs. The fiber diameters are summarized in Table 3.9. Average fiber diameter of Bio-KLA fiber mats was 42% smaller than untreated KLA mats. The mass yield of carbonization was 65% for KLA fibers and 58% for Bio-KLA fibers. The elements other than carbon were volatized during carbonization. The major diameter reduction was from electrospinning to thermostabilization for KLA, and from thermostabilization to carbonization for Bio-KLA. Average fiber diameter of KLA-R-CNT was 66% of the diameter of KLA-R. Average fiber diameter of Bio-KLA-R-CNT was 80% of that of Bio-KLA-R. Fiber diameter of Bio-KLA-R-CNF was 70% of KLA-R-CNF average diameter.
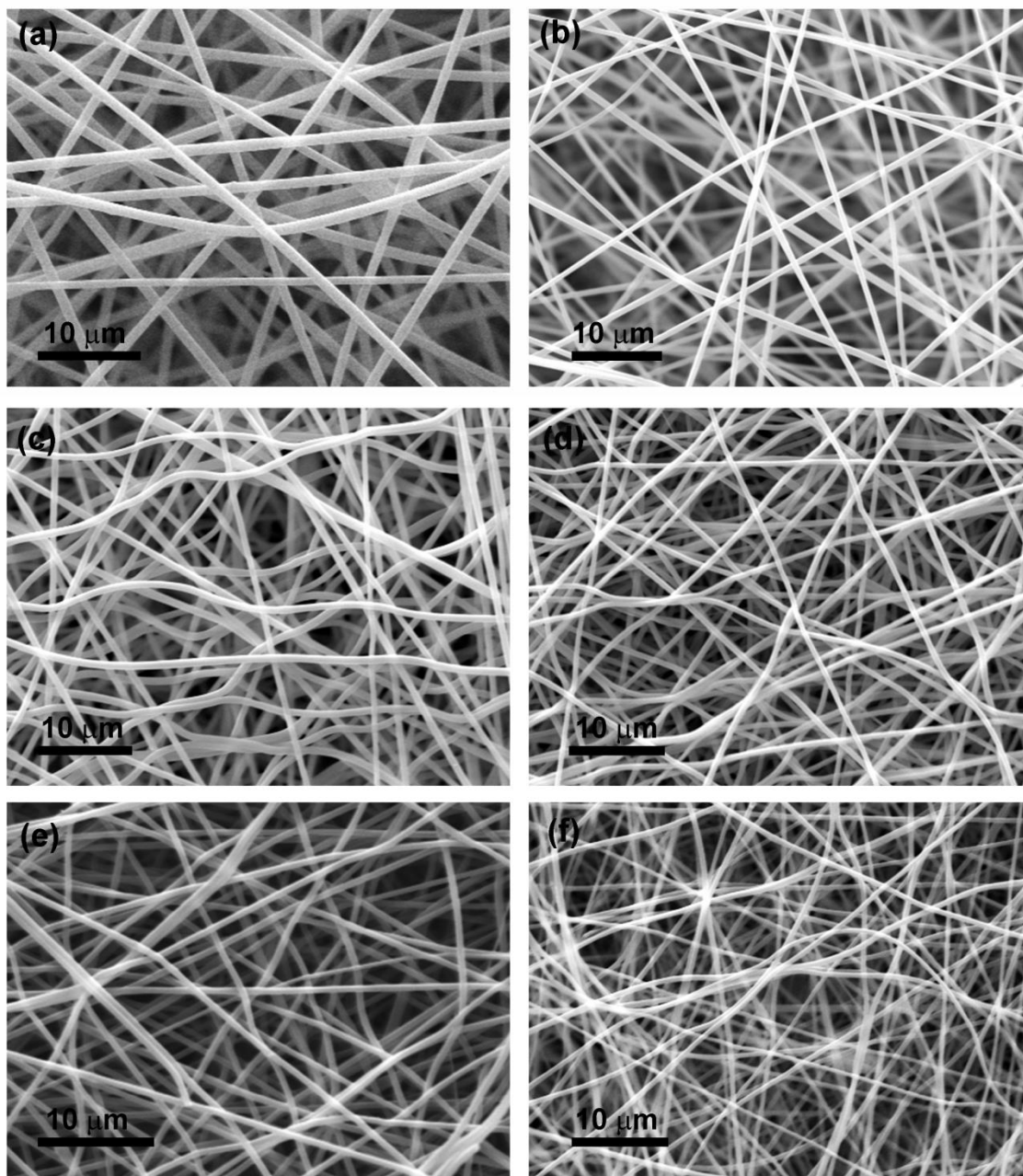
Figure 3.19. Fiber morphology of (a) KLA-R, (b) Bio-KLA-R, (c) thermostabilized KLA fibers, (d) thermostabilized Bio-KLA fibers, (e) KLA-R-CNF, and (f) Bio-KLA-R-CNF.

Table 3.9. Average fiber diameter and fiber morphology of random as-spun and carbonized untreated KLA and Bio-KLA

Lignin	Morphology	Diameter (nm)
KLA-R	Bead-free, uniform	1000.48±97.48
Thermostabilized KLA-R	Bead-free. uniform	756.88±137.09
KLA-R-CNF	Bead-free. uniform	663.17±64.51
Bio-KLA-R	Bead-free, uniform	582.86±90.07
Thermostabilized Bio-KLA-R	Bead-free, uniform	545.54±69.57
Bio-KLA-R-CNF	Bead-free, uniform	464.69±75.55

3.2.2. Tensile Deformation

Tensile deformation of KLA-R is shown in Figure 2.4 in Section 2.7. KLA-R mats showed ductile failure with necking. The defects in as-spun fibers, such as porous surface due to electrospraying, or fracture of single fiber promoted ductile fracture by void coalescence. KLA-R-CNF exhibited plastic deformation (Figure 3.20) while Bio-KLA-R-CNF was more brittle with higher elastic modulus.
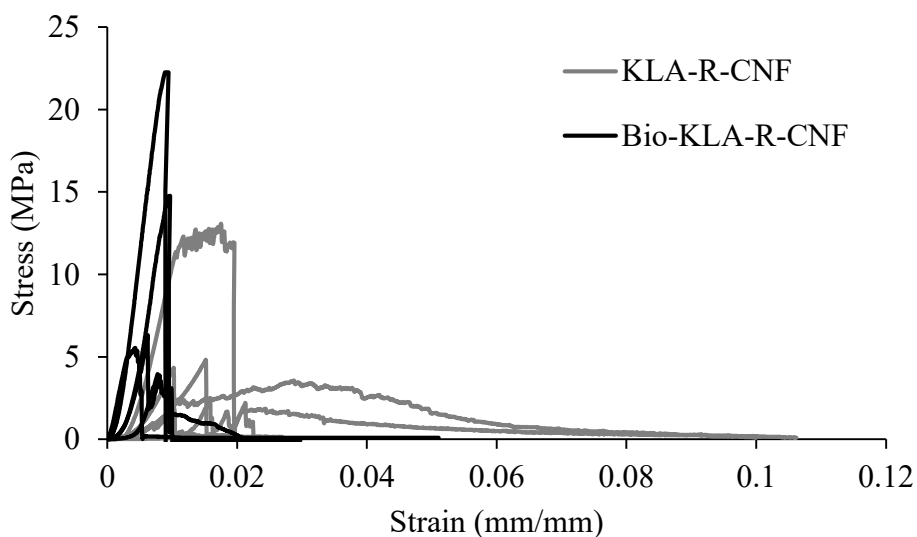
Figure 3.20. Stress-strain curves for KLA-R-CNF and Bio-KLA-R-CNF with each curve up to the point of failure. For each type of fiber, 5 curves are shown corresponding to 5 independent tests.

3.2.3. Mechanical Properties

Mechanical properties of KLA-R, KLA-R-CNF, Bio-KLA-R, and Bio-KLA-CNF were compared to their average fiber diameters in Figure 3.21. Bio-KLA-R-CNF showed 2.7 times

increase in elastic modulus and 2.1 times increase in tensile strength compared to KLA-R-CNF. Impurities in KLA generated defects in as-spun mats, which promoted stress concentration for crack propagation to take place more easily in tensile test. Extraction of impurities after bio-cleaning produced bead-free fibers with reduced average diameter. As illustrated in Figure 3.21a and Figure 3.21b, bio-cleaning enhanced tensile strength and elastic modulus. Carbonization process yielded fibers with improved strength and modulus, but decreased ductility (Figure 3.21c).
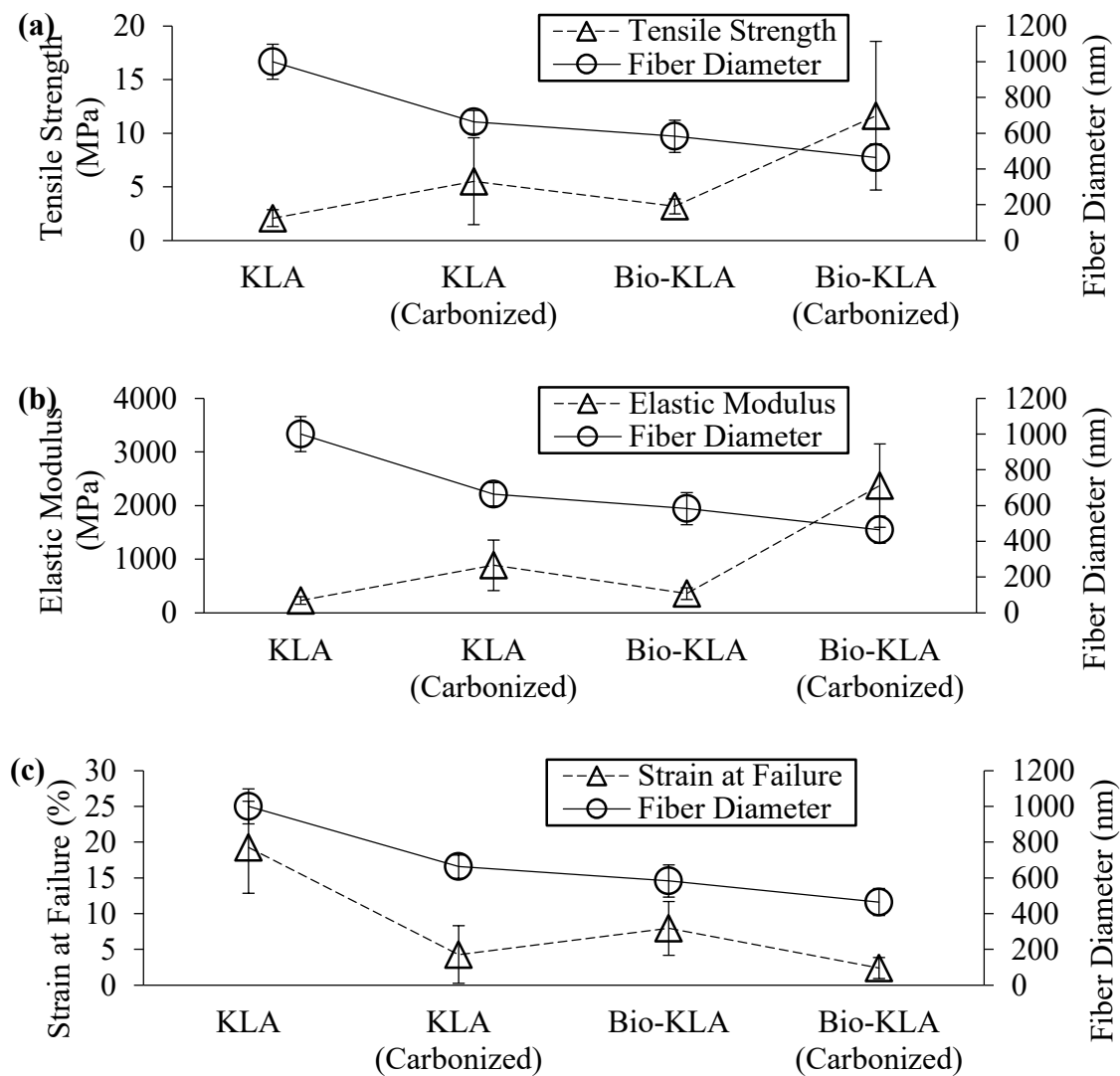
Figure 3.21. Comparison between average fiber diameter and (a) tensile strength, (b) elastic modulus, (c) strain at failure respectively for KLA-R, KLA-R-CNF, Bio-KLA-R, and Bio-KLA-R-CNF.

Chapter 4. Aligned KLA, Bio-KLA and Their CNFs

4.1. Aligned Untreated KLA

Aligned untreated KLA fibers were fabricated using a rotating drum. The electrospinning parameters were optimized to maximize mechanical properties and minimize average fiber diameter for aligned fibers. Box-Behnken method was used in this optimization.

4.1.1. Fiber Morphology

Fiber morphologies, distribution of fiber orientation and defects of KLA-A are presented in Figure 4.1. Over 100 measurements were made to determine average fiber diameter and alignment. The distribution of the fiber orientation was shifted so that the most probable orientation corresponded to an angle of 0°. By comparing the fibers electrospun at rotating speed of 2000 rpm (Figure 4.1a) and 3000 rpm (Figure 4.1b), more aligned fibers were achieved at higher rotational speed. The orientation distribution at 3000 rpm was narrower (standard deviation 25.86°) than that at 2000 rpm (standard deviation 31.38°) with a higher peak value, quantitatively confirming the enhancement in fiber alignment. The backside of the as-spun fibers at rotating speed of 2000 rpm is shown in Figure 4.1c with residue of release agent, and the standard deviation of the fiber orientation distribution was lower (±27.89°). As mat thickness increased, the decrease in electrostatic force induced loss in fiber alignment. Residue of release agent connected the fibers at the backside, forming islands that affected the density calculation of the fiber mats. Approximately 1/3 of the fiber mats showed residue of release agent (area coverage ~10%), while the rest of the fiber mats were residue-free. Fiber fusion (Figure 4.1d) was detected for most spinning conditions of KLA-A. An interesting observation was that some of the aligned fiber mats manifested separation of multiple layers. The multilayer structure indicated the as-spun mats could be composed of fiber laminates due to stronger inter-fiber bonding within the same layer.
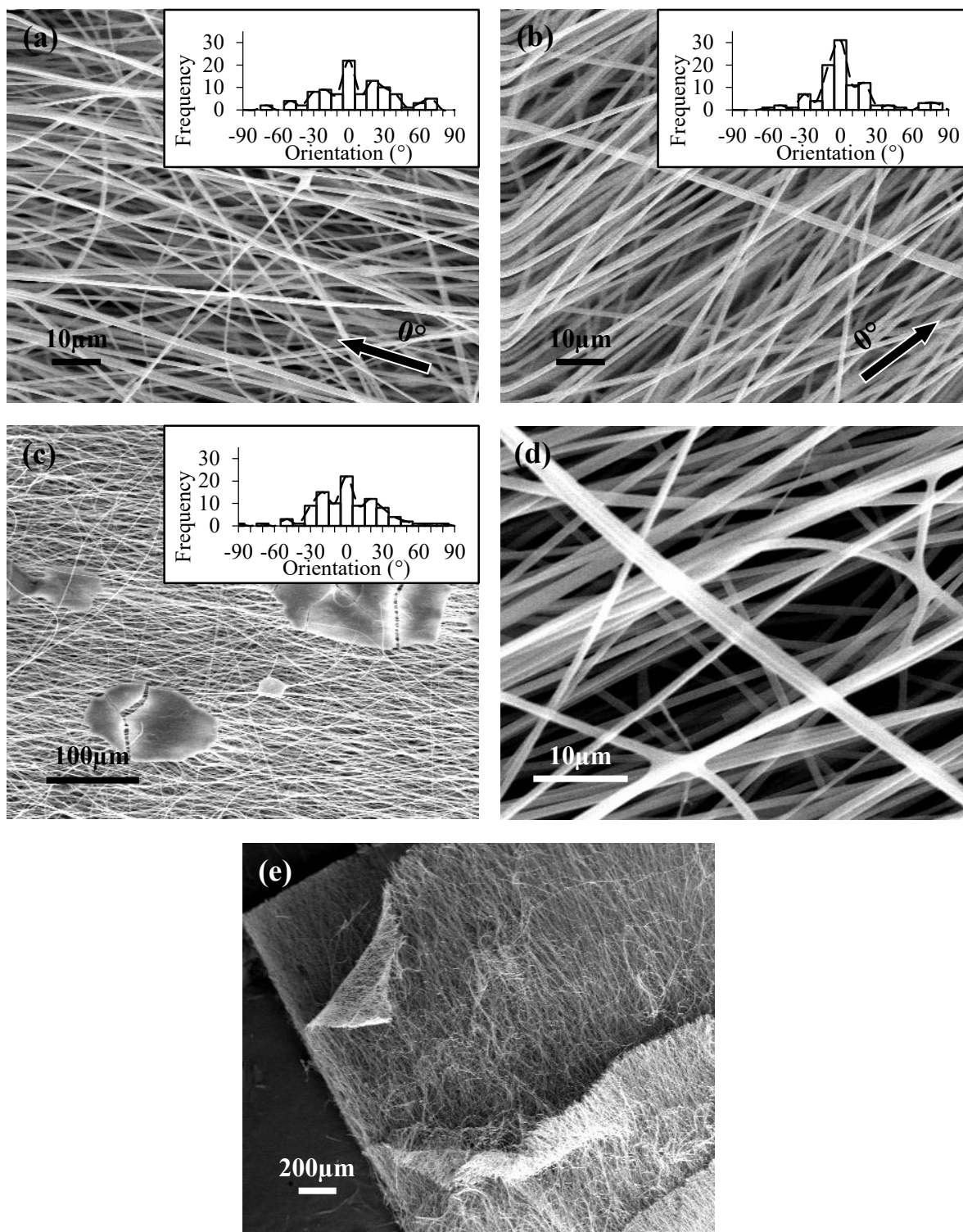
Figure 4.1. Fiber morphology of KLA-A at electric field of 65 kV/m, flow rate of 440 nl/s, rotating speed of (a) 2000 rpm and (b) 3000 rpm with sample defects of (c) release agent residue, (d) fiber fusion, and (e) multi-layer structure.

4.1.2. Optimization Analysis

The following characterization and optimization were performed assuming release agent residue had negligible effect on the properties of KLA-A. The optimized solution properties from KLA-R, including MW of PEO and lignin/PEO ratio of 95/5, were adopted for aligned fibers. To optimize electrospinning parameters for aligned fibers, electric field, flow rate, and rotating speed were investigated. Box-Behnken method was employed to optimize the electrospinning parameters for aligned KLA fibers. Box-Behnken design sacrificed the test runs with extreme values, for example, when all parameters were at their low level. Box-Behnken method produced reasonable estimation for quadratic model fitting, and relatively accurate analysis for both main parameter effects and interaction effects in an efficient manner. Two more center points (all parameters at intermediate level) were included to evaluate the reproducibility of the test runs. The design matrix (coded value) for the aligned fibers and the corresponding responses (actual value) are summarized in Table 4.1. Fiber diameter (D), elastic modulus (E), and tensile strength (σ), were selected as the responses.

The fit summary is provided for each model (coded value) in Table 4.2. Cubic terms were aliased so cubic model was discarded. Linear model was suggested for both fiber diameter and tensile strength with low sequential p-value (<0.05), and high adjusted and predicted R^2. However, predicted R^2 was negative for tensile strength, which suggested that the noise might be too high for the model to make adequate predictions. Quadratic model was selected for the elastic modulus. The difference between adjusted and predicted R^2 were larger than 0.2, possibly due to the large number of insignificant parameters in the model. It might reduce the stability of the model and lead to less accurate prediction. The prediction equations for all responses are listed in Table 4.3 for both coded and actual models.

Table 4.1. Design matrix of independent variables in coded values (subscripted c) and the corresponding responses in actual values (subscripted a) for KLA-A

Test Run	Coded Variables			Responses		
	$(F_\infty)_c$	Q_c (nm)	Ω_c (nm)	D_a (nm)	E_a (MPa)	σ_a (MPa)
1	+1	0	+1	900.46	799.64	6.90
2	0	0	0	895.79	979.13	8.75
3	+1	+1	0	946.48	807.50	7.98
4	-1	+1	0	1023.51	717.11	7.77
5	-1	0	-1	1023.51	806.49	7.42
6	+1	0	-1	907.01	940.67	11.20
7	+1	-1	0	900.40	886.83	10.54
8	0	0	0	1010.97	928.43	8.16
9	0	-1	-1	1045.12	890.06	9.19
10	0	+1	+1	1026.63	605.61	8.67
11	0	+1	-1	983.17	791.32	7.71
12	0	0	0	978.60	899.34	8.33
13	-1	0	+1	1149.09	782.08	5.07
14	-1	-1	0	1183.52	817.27	8.09
15	0	-1	+1	980.07	786.47	9.51

Table 4.2. Models recommended for each response of KLA-A

Response	Source	Sequential p-value	Adjusted R^2	Predicted R^2	Remarks
	Linear	**0.0054**	**0.5796**	**0.3964**	**Suggested**
	2FI	0.0973	0.7263	0.6036	
D	Quadratic	0.5303	0.7081	0.2734	
	Cubic	0.7989	0.5207		Aliased
	Linear	0.0437	0.3734	0.2376	
	2FI	0.8646	0.2101	-0.1759	
E	**Quadratic**	**0.0083**	**0.8577**	**0.5408**	**Suggested**
	Cubic	0.6533	0.8199		Aliased
	Linear	**0.0391**	**0.3869**	**-0.0252**	**Suggested**
	2FI	0.6844	0.2931	-1.1241	
σ	Quadratic	0.6800	0.1426	-3.8153	
	Cubic	0.0299	0.9571		Aliased

Table 4.3. Prediction equation for variables in coded and actual values

Prediction Equation (Coded Value)

$D_c = 996.95 - 90.66\ (F_\infty)_c - 16.17\ Q_c + 12.18\ \Omega_c$

$E_c = 935.63 + 38.96\ (F_\infty)_c - 57.39\ Q_c - 56.84\ \Omega_c + 5.21\ (F_\infty)_c * Q_c - 29.16\ (F_\infty)_c * \Omega_c - 20.53\ Q_c * \Omega_c - 32.30\ (F_\infty)_c{}^2 - 96.15\ Q_c{}^2 - 71.11\ \Omega_c{}^2$

$\sigma_c = 8.35 + 1.03\ (F_\infty)_c - 0.65\ Q_c - 0.67\ \Omega_c$

Prediction Equation (Actual Value)

$D_a = 2168.05 - 12.09\ (F_\infty)_a - 0.81\ Q_a + 0.02\ \Omega_a$

$E_a = -51788.47 + 92.62\ (F_\infty)_a + 211.28\ Q_a + 2.78\ \Omega_a + 0.03\ (F_\infty)_a * Q_a - 0.01\ (F_\infty)_a * \Omega_a - 0.002\ Q_a * \Omega_a - 0.57\ (F_\infty)_a{}^2 - 0.24\ Q_a{}^2 - 0.0003\ \Omega_a{}^2$

$\sigma_a = 16.02 + 0.14\ (F_\infty)_a - 0.03\ Q_a - 0.001\ \Omega_a$

Based on the ANOVA analysis for fiber diameter, elastic modulus, and tensile strength in Tables 4.4-4.6, the models were significant (p-value<0.05). Adequate precision for each model was higher than 4. For the linear model of fiber diameter, ANOVA analysis showed F_∞ was significant (p-value<0.05) while other parameters were insignificant. The quadratic model for elastic modulus contained five significant parameters or interactions. By ranking their influence, the parameters were Q^2, Q, Ω, Ω^2 and F_∞. Other parameters or interactions were not significant (p-value>0.05). For tensile strength, only F_∞ was significant in the linear model (p-value <0.05).

Table 4.4. ANOVA analysis of model (coded) for fiber diameter

Source	Sum of Squares	df	Mean Square	F-value	p-value
Model	69029.14	3	23009.71	7.43	0.0054
F_∞	65751.71	1	65751.71	21.24	0.0008
Q	2090.49	1	2090.49	0.6754	0.4286
Ω	1186.94	1	1186.94	0.3835	0.5483
Residual	34045.07	11	3095.01		
Lack of Fit	26987.89	9	2998.65	0.8498	0.6484
Pure Error	7057.18	2	3528.59		
Cor Total	103100	14			
User Std. Dev.	210.47			R^2	0.6697
Std. Dev.	55.63			Adjusted R^2	0.5796
Mean	996.95			Predicted R^2	0.3964
C.V. %	5.58			Adeq Precision	7.4367

Table 4.5. ANOVA analysis of model (coded) for elastic modulus

Source	Sum of Squares	df	Mean Square	F-value	p-value
Model	120300	9	13366.18	10.38	0.0095
F_∞	12144.53	1	12144.53	9.43	0.0278
Q	26346.14	1	26346.14	20.46	0.0063
Ω	25848.22	1	25848.22	20.07	0.0065
$F_\infty * Q$	108.51	1	108.51	0.0842	0.7833
$F_\infty * \Omega$	3400.11	1	3400.11	2.64	0.1651
$Q * \Omega$	1686.09	1	1686.09	1.31	0.3044
$F_\infty{}^2$	3852.08	1	3852.08	2.99	0.1443
Q^2	34137.18	1	34137.18	26.50	0.0036
Ω^2	18671.28	1	18671.28	14.50	0.0125
Residual	6440.00	5	1288.00		
Lack of Fit	3178.54	3	1059.51	0.6497	0.6533
Pure Error	3261.46	2	1630.73		
Cor Total	126700	14			
User Std. Dev.	263.45			R^2	0.9492
Std. Dev.	35.89			Adjusted R^2	0.8577
Mean	829.20			Predicted R^2	0.5408
C.V. %	4.33			Adeq Precision	11.0423

Table 4.6. ANOVA analysis of model (coded) for tensile strength

Source	Sum of Squares	df	Mean Square	F-value	p-value
Model	15.50	3	5.17	3.94	0.0391
F_∞	8.52	1	8.52	6.51	0.0270
Q	3.37	1	3.37	2.57	0.1369
Ω	3.61	1	3.61	2.75	0.1252
Residual	14.41	11	1.31		
Lack of Fit	14.22	9	1.58	17.26	0.0560
Pure Error	0.1832	2	0.0916		
Cor Total	29.91	14			
User Std. Dev.	3.02			R^2	0.5183
Std. Dev.	1.14			Adjusted R^2	0.3869
Mean	8.35			Predicted R^2	-0.0252
C.V. %	13.70			Adeq Precision	5.7650

To evaluate the validity of the models for the responses, predicted vs. actual values are shown for fiber diameter (Figure 4.2a), elastic modulus (Figure 4.2b), and tensile strength (Figure 4.2c). The data were close to the fitted line for elastic modulus, suggesting the model was accurate. The data were more dispersed for fiber diameter and tensile strength. The reduction in correlation between the predicted and actual values indicated the model was not as accurate.

Residuals vs. predicted responses plots were also used to substantiate the validity of the models (Figure 4.3). Externally studentized residuals for all responses lied within the confidence interval band, so outliers were not detected. There was no correlation between residuals and predicted response. Overall, the models were fitting the data well.
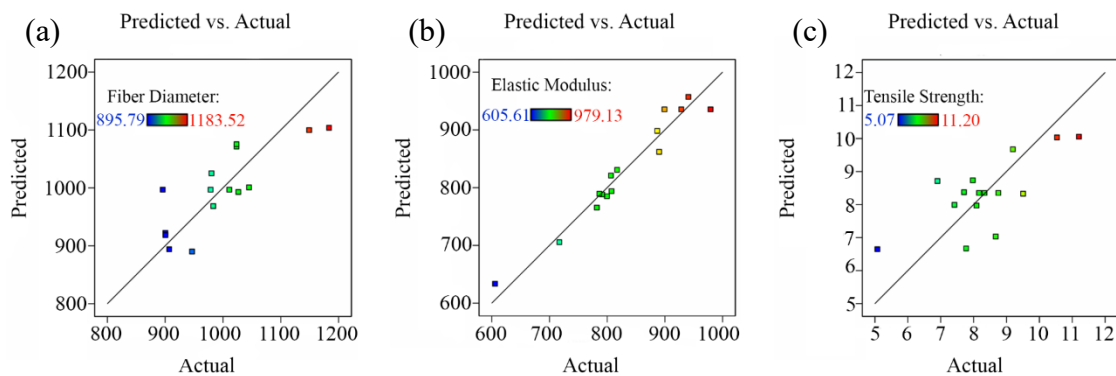
Figure 4.2. Predicted value versus actual value for (a) fiber diameter, (b) elastic modulus and (c) tensile strength.
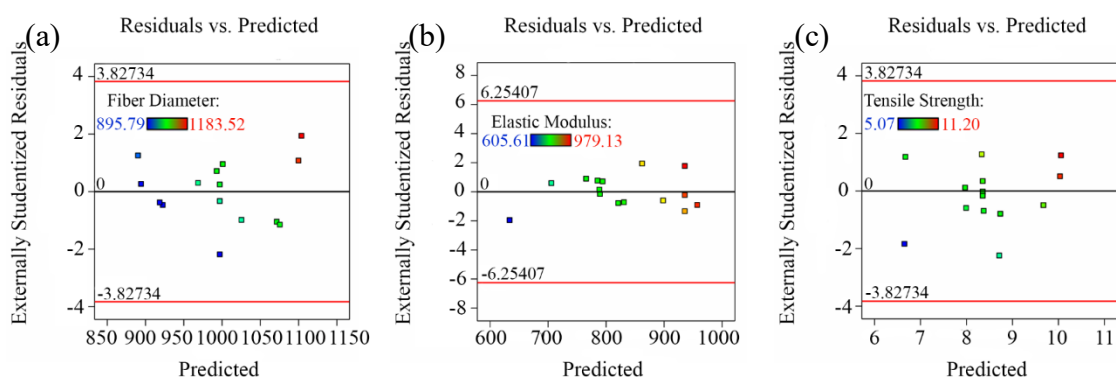
Figure 4.3. Residuals versus predicted value for (a) fiber diameter, (b) elastic modulus and (c) tensile strength.

With 95% confidence interval, the main parameter effects on the responses are displayed in Figure 4.4. Steep slope revealed a strong negative correlation between fiber diameter and F_∞ (Figure 4.4a). There was no correspondence between the fiber diameter and other two main parameter effects.

From the main parameter effects in the quadratic model for elastic modulus (Figure 4.4d-f), the curved trend indicated the probability of obtaining a maximum response at the middle level of each parameter. Elastic modulus demonstrated an overall weak positive correlation with F_∞ and weak negative correlation with the other two parameters, Q and Ω. Increasing F_∞ slightly increased elastic modulus while decreased fiber diameter, in contrast to the optimization analysis for KLA-R. Therefore, the relationship between mechanical properties and fiber diameter was complicated. The negative correlation elastic modulus had with Q could be induced by possible electrospraying at high Q. The enhanced fiber alignment with Ω was expected to enhance the mechanical properties of the aligned fiber mats. Average elastic modulus of KLA-A at 2000 rpm was greater than the

elastic modulus of optimized KLA-R (Section 3.2.3). However, the elastic modulus was observed to decrease as Ω increased further from 2000 rpm to 3000 rpm. This suggested that the improvement of elastic modulus with Ω might have an optimal value at specific value of Ω. Large Ω could engender stronger airflow, affecting jet instability and deposition of fibers. The existence of an optimal Ω was also reported by Thomas et al[102].

Tensile strength increased with F_∞, decreased with Q and Ω (Figure 4.4g-i). The correlation with Q and Ω were insignificant as mentioned in ANOVA analysis. The augmentation of tensile strength by increasing F_∞ was also due to finer fibers produced at higher F_∞.
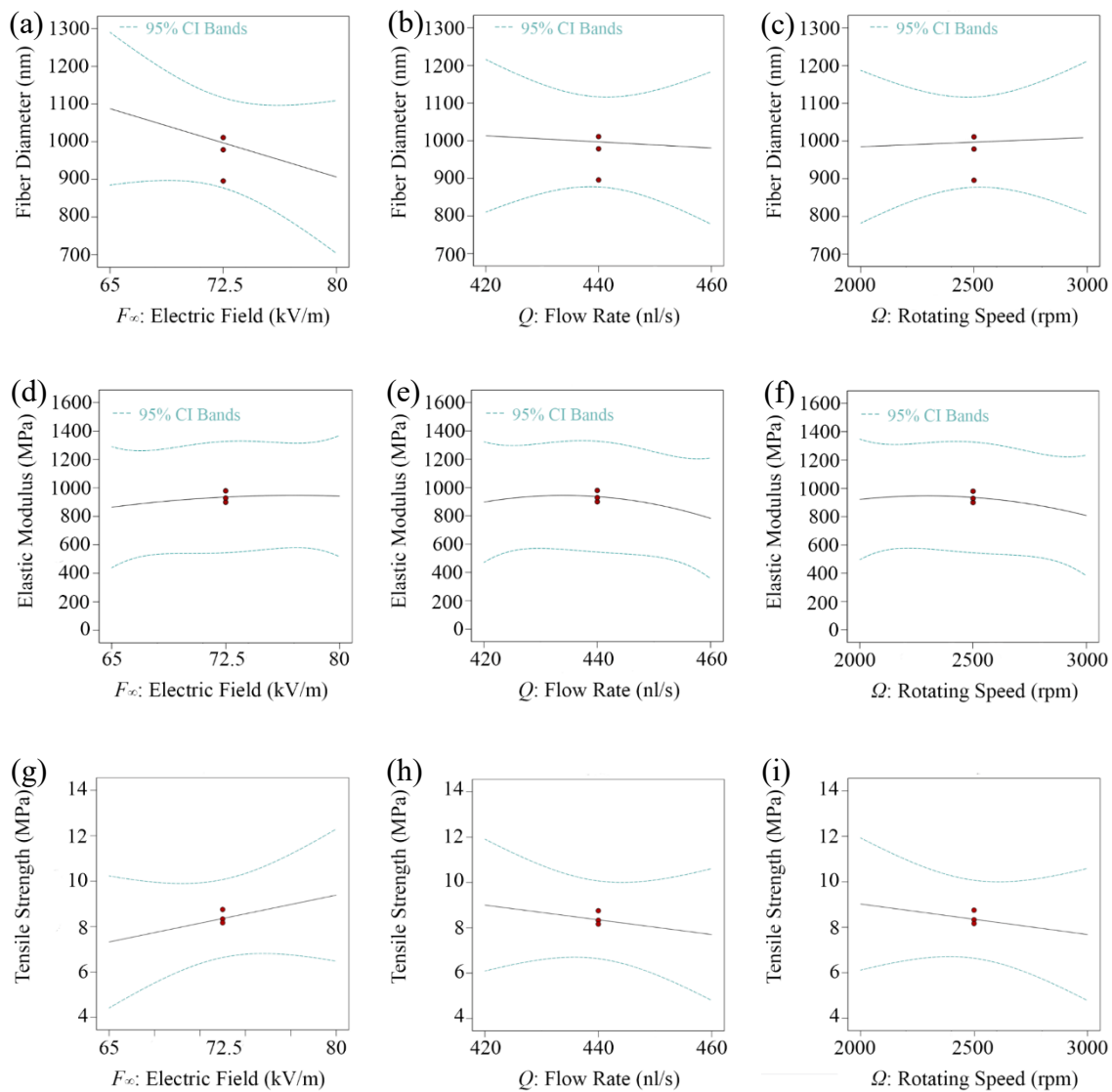
Figure 4.4. Main effects of (a, d, g) electric field, (b, e, h) flow rate, and (c, f, i) rotating speed on (top) fiber diameter, (middle) elastic modulus and (bottom) tensile strength.

The parameter interaction effects on elastic modulus are shown in Figure 4.5. Although extensive curvature was observed for the contour plots, the interaction effects were not significant as per ANOVA analysis.
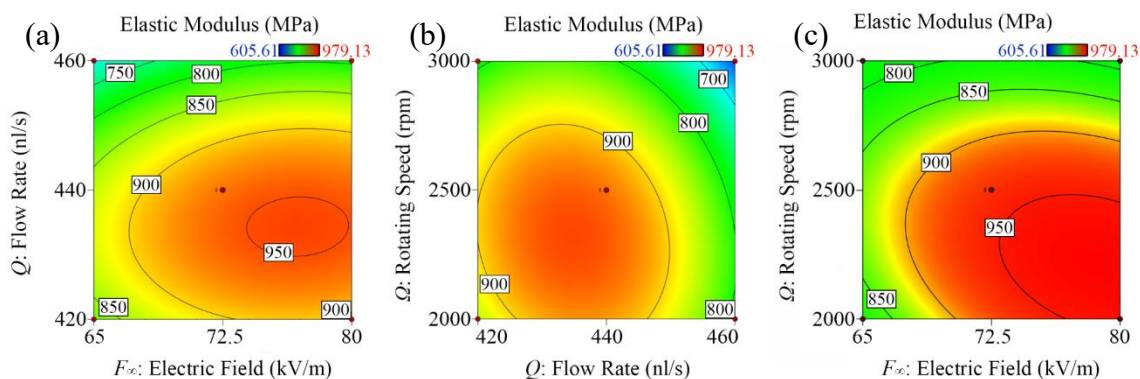
Figure 4.5. Interaction effects between (a) electric field and flow rate, (b) flow rate and rotating speed, (c) electric field and rotating speed on elastic modulus.

The limits of responses are summarized in Table 4.7 for optimization of the electrospinning conditions. The goal of the optimization was to minimize fiber diameter, maximize tensile strength and elastic modulus. The importance assigned to each response was the same. The optimal electrospinning condition with highest desirability to produce fiber mats with high mechanical properties and low average fiber diameter is listed in Table 4.8. The optimized condition was found to be electric field of 80 kV/m, flow rate of 440 nl/s, and rotating speed of 2000 rpm. The predicted responses were 10 MPa in tensile strength, 957 MPa in elastic modulus and 894 nm in average fiber diameter. The experimental values of the responses were tensile strength of 11.20±3.02 MPa, elastic modulus of 940.67±182.41 MPa, average fiber diameter of 907.01±147.44 nm at the optimized electrospinning condition. The experimental values were close to the predicted values, signifying the adequacy of the model prediction.

Table 4.7. Optimization goals and limits of optimization parameters for aligned fibers

Name	Goal	Lower Limit	Upper Limit	Importance
Electric Field	in range	65	80	3
Flow Rate	in range	420	460	3
Rotating Speed	in range	2000	3000	3
Tensile Strength	maximize	3	15	3
Elastic Modulus	maximize	400	1200	3
Fiber Diameter	minimize	700	1400	3

Table 4.8. Optimal condition for electrospinning of KLA-A

Optimal parameters			Predicted response			Desirability
F_∞	Q	Ω	σ	E	D	
80	440	2000	10	957	894	0.666

4.2. Aligned KLA CNFs & Bio-KLA

The optimized KLA-A fibers were carbonized to form CNFs. Bio-KLA was also electrospun into aligned fibers under the same electrospinning condition, but SEM characterization and carbonization of Bio-KLA-A could not be conducted due to lab closure caused by COVID-19 pandemic. Fiber morphologies were examined for optimal KLA-A and KLA-A-CNF. KLA-R with release agent were fabricated at the optimal condition for KLA-R without release agent to examine the effect of release agent residue on the fiber morphology and the mechanical properties of the resulted fiber mats. Their mechanical properties were compared to Bio-KLA-A.

4.2.1. Fiber Morphology & Effect of Residue

The morphologies of KLA-R (with release agent), KLA-A and KLA-A-CNF are presented in Figure 4.6. Their average fiber diameters are compiled in Table 4.9. KLA-A and KLA-A-CNF were mostly bead-free but the fibers became curved and fused after carbonization (Figure 4.6b). Fiber relaxation due to increased mobility during thermostabilization possibly took place before cross-linking occurred[57], which induced fusion in carbonization. Average fiber diameter for KLA-A-CNF was 77% of fiber diameter for KLA-A. Mass yield of carbonization was 47% for aligned KLA fibers.

For KLA-R with applied release agent, large cracked blocks were found on the backside of the fiber mat (Figure 4.6c). Either residue of release agent or electrospraying of lignin solution could contribute to formation of such defect. The random fibers were bead-free, slightly flat, and occasionally fused (Figure 4.6d). The average fiber diameter of optimal KLA-R with release agent (Table 4.9) was 1.5 times larger than the fiber diameter of optimal KLA-R without release agent (Table 3.9). Release agent possibly reduced the electric conductivity of the collector, weakened the electric field, thus increasing the average fiber diameter of the fiber mat.
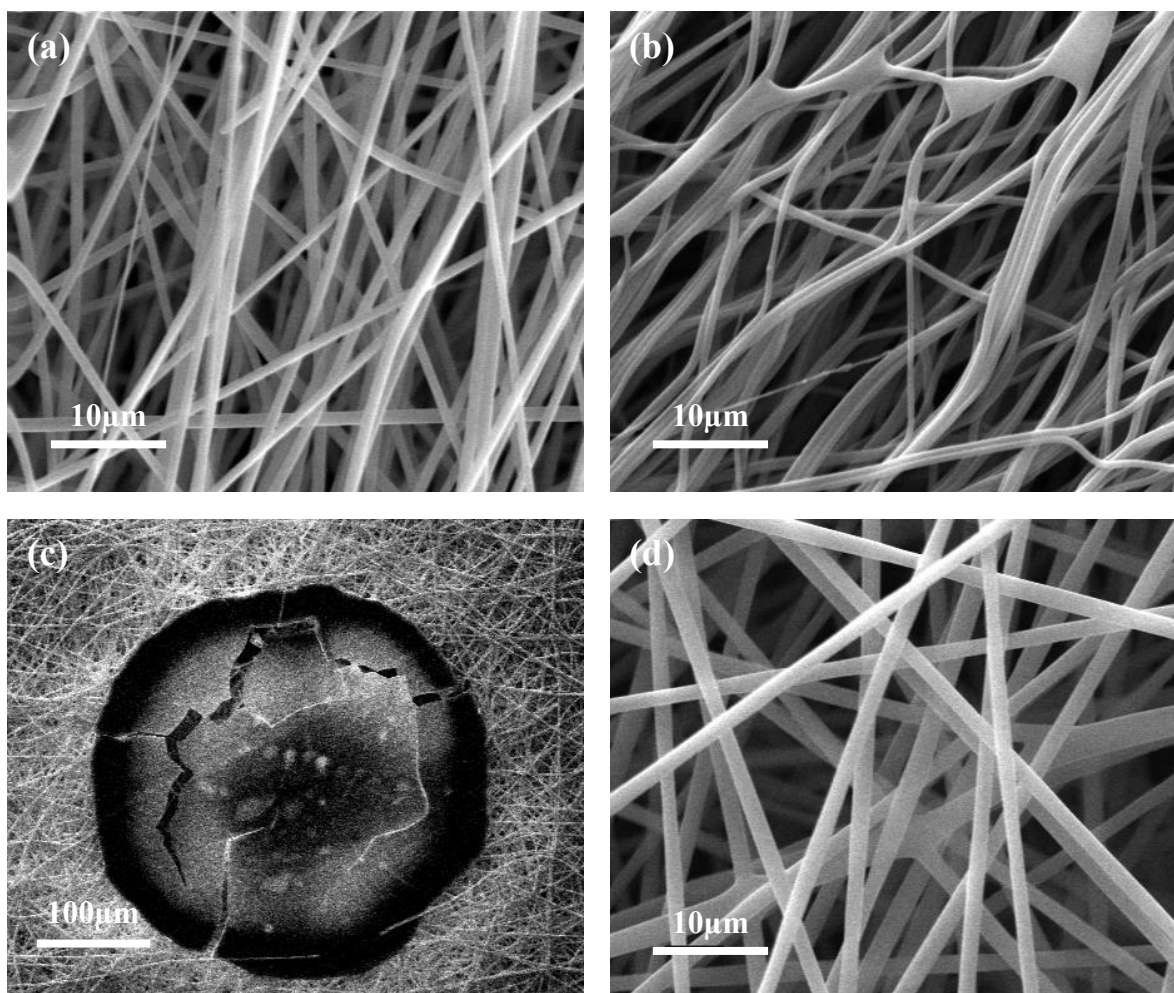
Figure 4.6. Fiber morphology of optimal (a) KLA-A, (b) KLA-A-CNF, (c) KLA-R at residue side, and (d) KLA-R at front surface with release agent.

Table 4.9. Average fiber diameter and fiber morphology of random and aligned untreated KLA after electrospinning and carbonization

Lignin (all with release agent)	Morphology	Diameter (nm)
KLA-R	Bead-free, fusion	1509.68 ± 177.57
KLA-A	Mostly bead-free, fusion	907.01 ± 147.44
KLA-A-CNF	Mostly bead-free, fusion	697.07 ± 96.41

4.2.2. Tensile Deformation

The tensile specimens of aligned fibers showed different tensile deformation in Figure 4.7. KLA-A exhibited, with increasing ductility, failure without necking (Figure 4.7a) due to void sheeting, failure with necking (Figure 4.7b) similar to KLA-R, and incomplete multi-layer failure (Figure 4.7c). Different from KLA-R-CNF, most samples of KLA-A-CNF did not exhibit plastic deformation (Figure 4.7d and Figure 4.8). The brittle failure of carbonized aligned fiber was possibly attributed to localized shear.
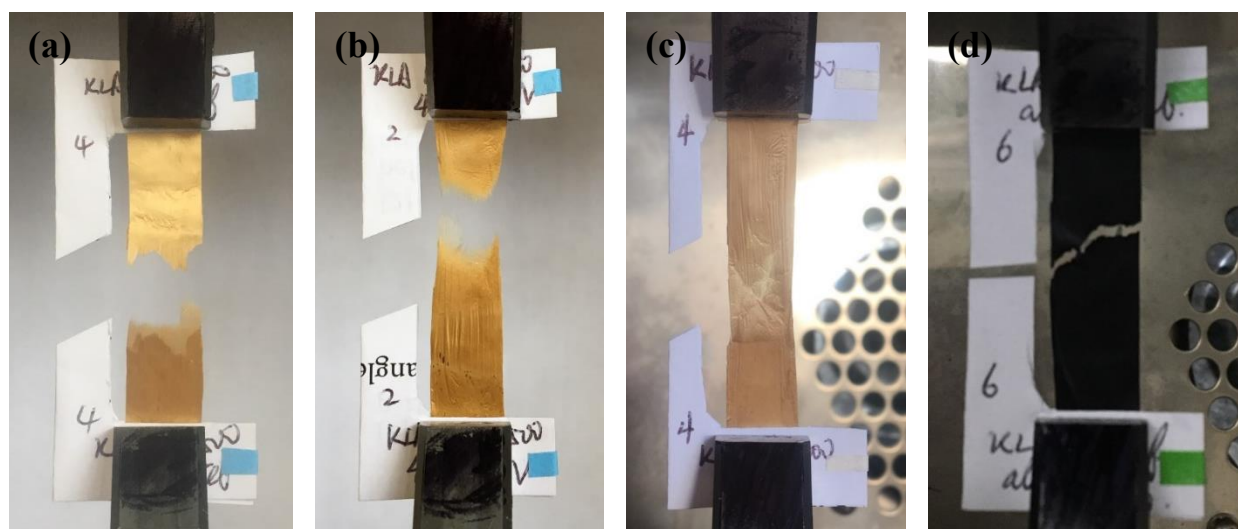
Figure 4.7. Tensile specimens of different tensile deformation of (a, b, c) KLA-A and (d) KLA-A-CNF.
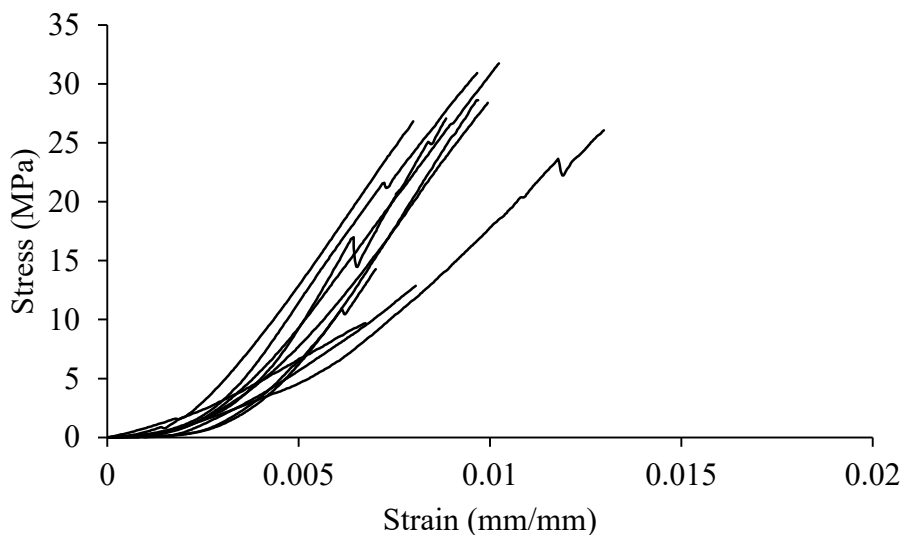
Figure 4.8. Stress-strain curves for KLA-A-CNF with each curve up to the point of failure. 10 curves are shown corresponding to 10 independent tests.

4.2.3. Mechanical Properties

The mechanical properties of KLA-A and KLA-A-CNF, Bio-KLA-A, KLA-R with and without release agent are illustrated in Figure 4.9. Tensile strength and elastic modulus showed similar trend. When release agent was applied to obtain KLA-R, 68% reduction in tensile strength and 62% reduction in elastic modulus were obtained. The substantial increase in average fiber diameter with applied release agent led to poorer mechanical properties.

KLA-A showed 16.7 times higher in tensile strength, and 10.6 times higher in elastic modulus than KLA-R with release agent. Bio-KLA-A did not show an improvement in mechanical properties compared to KLA-A. Bio-KLA-A was 42% lower in tensile strength but elastic modulus was comparable to KLA-A at optimal electrospinning condition. It was more difficult to adjust the electrospinning conditions for Bio-KLA-A than Bio-KLA-R since more parameters should be included. In addition, rotating drum generated strong air circulation that impacted electric field, jet trajectory, flow rate, and other parameters. The optimized condition for aligned KLA fibers might not be exactly same for Bio-KLA fibers. Further optimization might be required.

After carbonization, KLA-A-CNF exhibited 2.1 times higher in tensile strength, 4.2 times higher in elastic modulus, and 12.0 times lower in strain at failure than KLA-A. The tensile strength and elastic modulus of KLA-A-CNF were 23.65±7.70 MPa and 3960.98±1155.67 MPa, respectively.
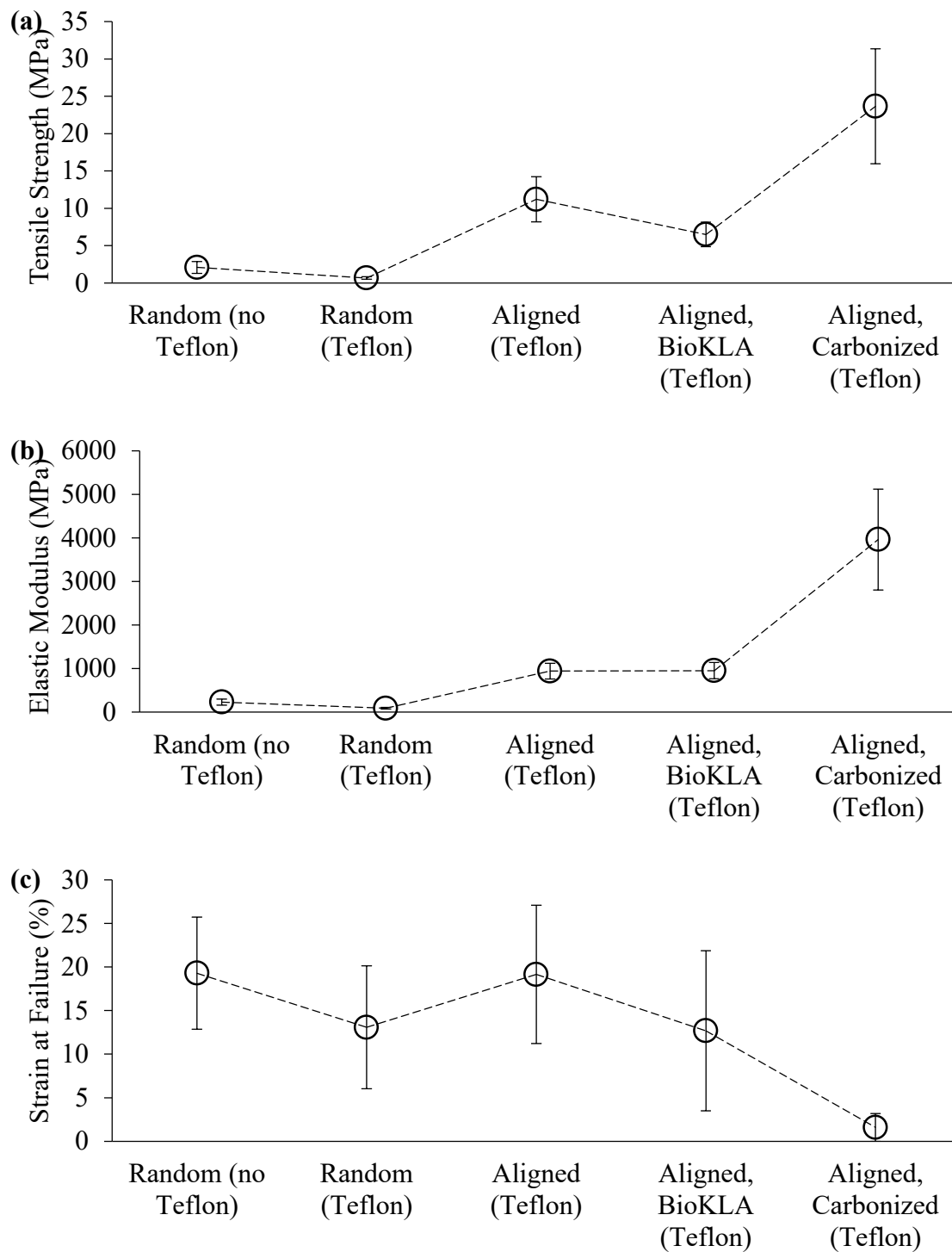
Figure 4.9. Comparison of (a) tensile strength, (b) elastic modulus, and (c) strain at failure for lignin fiber mats with different treatments.

Chapter 5. Random Bio-KLB

Untreated KLB was too viscous to be electrospun into fibers. After biodegradation, uniform random fibers could be fabricated from Bio-KLB. The optimal condition for KLA-R was adopted for Bio-KLB-R. Fiber morphology, average fiber diameter and mechanical properties were characterized for both Bio-KLB-R and Bio-KLB-R-CNF. Aligned Bio-KLB fibers were not detachable from collector, even when release agent was used. It suggested more parameters should be considered in the optimization process for aligned Bio-KLB.

5.1. Fiber Diameter & Morphology

Bio-KLB-R were electrospun at optimal condition for KLA-R. The morphology of Bio-KLB-R showed uniform fibers with slight ribbon-structure (Figure 5.1a) and BOAS structure (Figure 5.1b). Both collapsed beads and torus beads formed for Bio-KLB-R due to rapid evaporation of residual solvent. It was hypothesized that incomplete solvent evaporation might be attributed to lower relaxation time[131] compared to KLA/Bio-KLA. Mass yield of carbonization was 54% for random Bio-KLB fibers. Average fiber diameter of Bio-KLB-R-CNF (Figure 5.1c) was 278.95±49.89 nm, lower than average fiber diameter of Bio-KLB-R at 421.58±59.47 nm. These fibers possessed finest diameter among various treatments and experimental conditions investigated in this study.
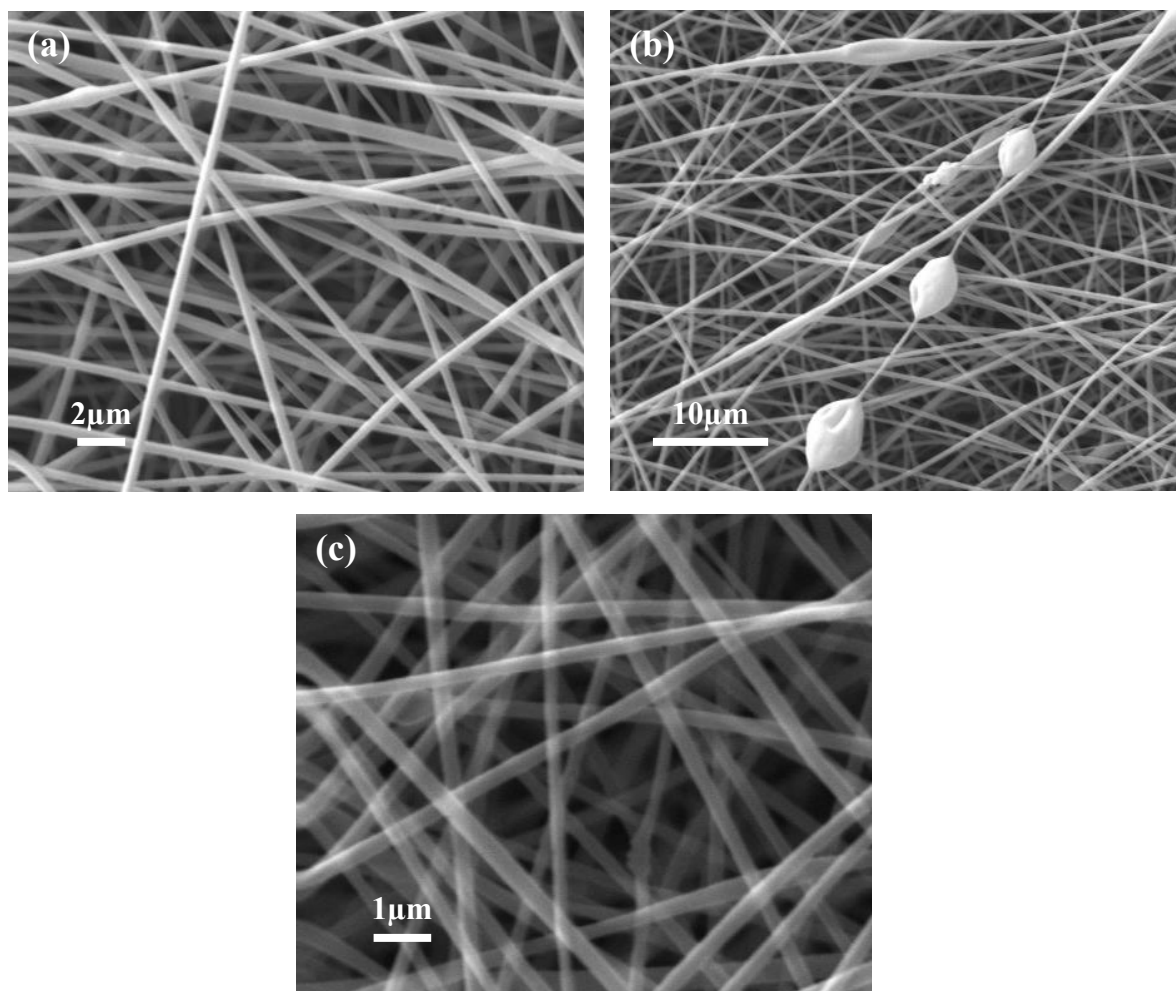
Figure 5.1. Fiber morphology of random (a) Bio-KLB-R with uniform fibers, (b) Bio-KLB-R with BOAS structure, and (c) Bio-KLB-R-CNF at lignin/PEO ratio of 95/5.

5.2. Mechanical Properties

The mechanical properties of Bio-KLB-R and Bio-KLB-R-CNF were summarized in Figure 5.2. Tensile strength and elastic modulus were 4.1 times and 6.3 times higher respectively after carbonization. Strain at failure for Bio-KLB-R was 5.8 times higher than Bio-KLB-R-CNF.
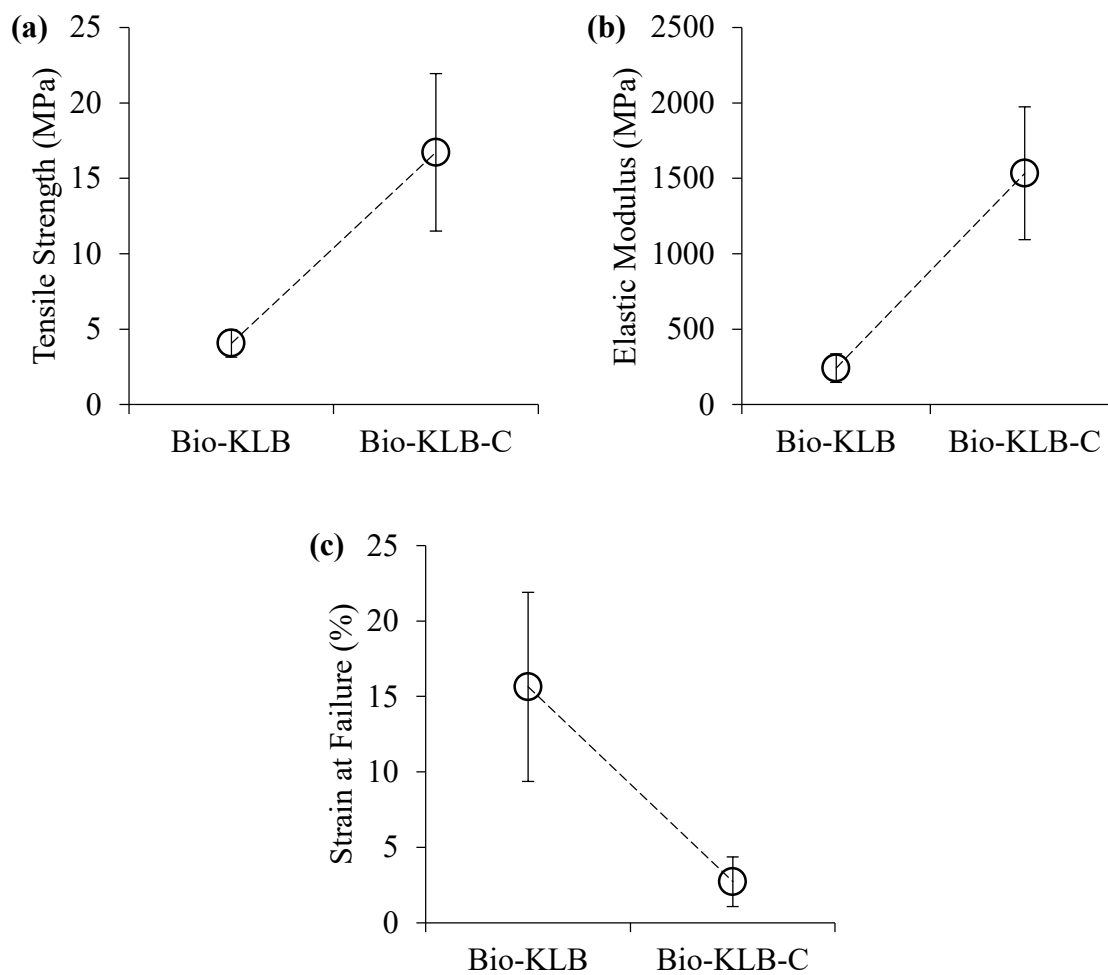
Figure 5.2. Mechanical properties including (a) tensile strength, (b) elastic modulus, and (c) strain at failure of Bio-KLB-R and Bio-KLB-R-CNF.

Chapter 6. Conclusions and Future Works

  6.1. Conclusions

  Lignin as an alternative CNF precursor to replace PAN and pitch was substantiated to be plausible. Lignin greatly reduced the cost of CNFs and alleviated the negative environmental impact of the manufacturing process. To target the problem of poor mechanical properties of lignin-based CNFs, bio-cleaning and aligning fibers were proposed to meet this goal. Electrospinning was conducted to produce both random and aligned fibers from KLA, Bio-KLA, and Bio-KLB. The electrospinning parameters and solution conditions were optimized to minimize fiber diameter, maximize tensile strength and elastic modulus. The optimized condition for random and aligned fibers were applied to fabricate carbon fibers. The fiber morphology and the mechanical properties of fibers were characterized after each stage of manufacturing process. The key results are summarized below:

- In the spinnability test, diagonal spinnability table was produced for untreated KLA. High total solid concentration yielded ribbon-like fibers after electrospinning. The spinnability transition point occurred at higher lignin/PEO ratio as total solid concentration increased. Higher PEO molecular weight reduced required PEO fraction to reach desired spinnability.

- For as-spun random KLA fibers, minimum fiber diameter was achieved at flow rate of 420 nl/s. Collection time did not show significant effect on fiber diameter. Fiber diameter was inversely correlated to voltage. Preheating of solution could assist with reducing fiber diameter. After narrowing down the investigated parameters, the optimized condition for random fibers was electric field of 50 kV/m, lignin/PEO ratio of 95/5, and 1000 kDa PEO. By adopting the optimized solution condition for random fibers, the optimized electrospinning condition for aligned KLA fibers was electric field of 80 kV/m, flow rate of 440 nl/s, and rotating speed of 2000 rpm.

- The optimized condition for random KLA fibers was employed to fabricate random Bio-KLA and Bio-KLB fibers while the optimized condition for aligned KLA fibers was used to fabricate aligned Bio-KLA and Bio-KLB fibers. The mechanical properties and the average fiber diameter of all fibers fabricated in this study are summarized in Table 6.1. In general, bio-cleaning reduced average fiber diameter, enhanced mechanical properties, and mitigated formation of defects for KLA. It demonstrated the viability of a sustainable

purification technique to increase the properties of lignin-based CNFs in an economical and environmental-friendly manner. In terms of KLB, bio-cleaning greatly improved its spinnability. At optimal condition, random Bio-KLB CNFs exhibited lowest fiber diameter. Aligning fibers further decreased fiber diameters and improved mechanical properties of as-spun fibers. A simple adjustment of electrospinning setup from static to rotating collector achieved this purpose effectively and inexpensively. Application of release agent assisted with detaching fibers from substrate but it exhibited negative impact on mechanical properties of as-spun fiber mats.

Table 6.1. Summary of mechanical properties and fiber diameter of lignin fibers reported in this study

Lignin	Average Fiber Diameter (nm)	Tensile Strength (MPa)	Elastic Modulus (MPa)
As-spun random KLA	1000.48±97.48	2.08±0.80	229.79±69.21
As-spun random KLA (Tef)	1509.68 ± 177.57	0.67 ± 0.18	88.34 ± 20.7
As-spun random Bio-KLA	582.86±90.07	3.19±0.70	358.61±109.53
As-spun random Bio-KLB	421.577±59.47	4.06±0.92	241.88±93.74
As-spun aligned KLA (Tef)	907.01 ± 147.44	11.2 ± 3.02	940.67 ± 182.41
As-spun aligned Bio-KLA (Tef)	Not measured	6.49 ± 1.64	950.98 ± 186.53
Carbonized random KLA	663.17±64.51	5.52±4.05	886.29±471.47
Carbonized random Bio-KLA	464.69±75.55	11.64±6.94	2374.28±778.34
Carbonized random Bio-KLB	278.95±49.89	16.72±5.21	1532.87±439.63
Carbonized aligned KLA (Tef)	697.07 ± 96.41	23.65 ± 7.7	3960.98 ± 1155.67

Even though a few challenges still required to be addressed in future work, the characterizations conducted in the study demonstrated the prospective of bio-cleaning as a promising solution to fabricate high-quality lignin-based CNFs.

6.2. Future Works

From the current study, further investigation on the following topics is recommended to understand the fundamental mechanism of lignin-based CNF production and the approaches to improve the properties of lignin-based CNFs.

- **Characterization of Lignin Solution**

    Investigating the rheological properties of lignin solution will lay a basic understanding of how jet behaves during electrospinning process, and subsequently correlate the solution properties to the resulted fiber morphology. Extensional viscosity is a significant parameter to characterize since the fundamental mechanism is to use electrostatic force to elongate solution. There is a high possibility to associate the transition from BOAS structure to bead-free smooth fibers with the extensional properties of the solution. The ribbon-like structures and the collapsed beads caused by incomplete solvent evaporation can also be correlated to the extensional properties.

- **Characterization and Optimization of As-spun Mats**

    Due to lab closure caused by COVID-19 pandemic, SEM for aligned Bio-KLA fibers and fabrication of aligned Bio-KLA CNFs were not conducted. Characterization of fiber morphology and fiber diameter may provide an insight into the slightly weaker mechanical properties of aligned Bio-KLA fibers than aligned KLA fibers. Optimized condition of aligned KLA fibers did not apply for Bio-KLB fibers. A separate optimization process comprising of more solution parameters needs to be conducted for aligned Bio-KLB fibers.

    The fabricated aligned fiber mats showed multilayer structures. The bonding between layers can be analyzed to explore if particles can be embedded between layers in application of delayed release drug delivery.

    Wettability of the lignin fibers can be evaluated by measuring the contact angle of droplet on the surface. Most lignin fibers exhibited strong electrostatic repulsion or attraction. The charging effect of the fibers can also be characterized to understand the charge capacity of lignin fibers. If the fibers are highly charged after electrospinning, its electrical conductivity can be measured to explore its application as a conductor.

- **Modelling**

    Elastic modulus and tensile strength of random or aligned as-spun lignin fibers can be modelled to obtain more insightful understanding of the unique properties of single fiber or fiber mats. The electrospinning process can also be modelled to analyze the relationship between fabricated fibers and electrospinning parameters, such as draw ratio, jet instability, applied voltage, etc.

- **Improvement of CNF Mechanical Properties**

Release agent was found to have negative effect on the mechanical properties of the as-spun fiber mats. The interaction between release agent and lignin/PEO fibers needs to be investigated to understand how release agent affects the properties. New methods can also be proposed to replace release agent for aiding removal of lignin fibers.

Preheating solution to reduce fiber diameter was proven to be feasible. If the solution is heated constantly during electrospinning, the average fiber diameter can be decreased with more uniform diameter distribution. Heating elements and insulation material can be attached or wrapped around the syringe to heat the solution evenly.

If tension is applied during thermostabilization process, the mechanical properties of CNFs can be improved. In the current setup, the sample was lied on a flat quartz plate. If the edges of the sample were fixed, tears or notches were introduced to the sample. An apparatus should be designed to apply tension and adjust for deformation during thermostabilization process.

- **Potential Fabrication of Lignin-based Graphite and Other Applications**

Humidified Bio-KLA powders yielded CNFs with metallic appearance. Effect of ambient humidity during electrospinning process was reported by other studies, but there were few studies related to effect of humidity in lignin powders on electrospinning behavior. If introduction of humidity does not induce defects while reducing the carbonization temperature for lignin samples, it can be a hypothesized method to bring down the required temperature of graphitization. The production cost of graphitized fibers can be greatly reduced.

The applications of lignin-based CNFs can be explored by fabricating CNFs into sensors, membranes for filtration, scaffolds, battery electrodes, or fillers embedding into other matrix to produce composite material.

References

1. Chand, S. Review carbon fibers for composites. *J. Mater. Sci.* **35**, 1303–1313 (2000).
2. Rebouillat, S., Peng, J. C. M., Donnet, J. B. & Ryu, S. K. Carbon fiber applications. in *Carbon fibers* 463–465 (Marcel Dekker, 1998).
3. Chung, D. D. L. *Carbon fiber composites*. (Elsevier, 2012).
4. Inagaki, M. *New carbons-control of structure and functions*. (Elsevier, 2000).
5. Mordkovich, V. Z. Carbon nanofibers: A new ultrahigh-strength material for chemical technology. *Teor. Osn. Khimicheskoi Tekhnologii* **37**, 460–471 (2003).
6. Park, S. J. & Seo, M. K. *Interface science and composites*. vol. 18 (Academic Press, 2011).
7. Klett, J., Hardy, R., Romine, E., Walls, C. & Burchell, T. High-thermal-conductivity, mesophase-pitch-derived carbon foams: effect of precursor on structure and properties. *Carbon N. Y.* **38**, 953–973 (2000).
8. Roberts, A. The Carbon Fibre Industry Worldwide 2011-2020: an evaluation of current markets and future supply and demand. *Mater Tech Pub* (2011).
9. Zhou, F. L. & Gong, R. H. Manufacturing technologies of polymeric nanofibres and nanofibre yarns. *Polym. Int.* **57**, 837–845 (2008).
10. Thenmozhi, S., Dharmaraj, N., Kadirvelu, K. & Kim, H. Y. Electrospun nanofibers: New generation materials for advanced applications. *Mater. Sci. Eng. B Solid-State Mater. Adv. Technol.* **217**, 36–48 (2017).
11. Gupta, A. K., Paliwal, D. K. & Bajaj, P. Acrylic precursors for carbon fibers. *J. Macromol. Sci. Part C* **31**, 1–89 (1991).
12. Gupta, A. & Harrison, I. R. New aspects in the oxidative stabilization of PAN-based carbon fibers. *Carbon N. Y.* **34**, 1427–1445 (1996).
13. Chae, H. G. *et al.* High strength and high modulus carbon fibers. *Carbon N. Y.* **93**, 81–87 (2015).
14. Honjo, K. Fracture toughness of PAN-based carbon fibers estimated from strength-mirror size relation. *Carbon N. Y.* **41**, 979–984 (2003).
15. Zussman, E. *et al.* Mechanical and structural characterization of electrospun PAN-derived carbon nanofibers. *Carbon N. Y.* **43**, 2175–2185 (2005).
16. Arshad, S. N., Naraghi, M. & Chasiotis, I. Strong carbon nanofibers from electrospun polyacrylonitrile. *Carbon N. Y.* **49**, 1710–1719 (2011).
17. Gill, A. S., Visotsky, D., Mears, L. & Summers, J. D. Cost estimation model for pan based carbon fiber manufacturing process. in *ASME 2016 11th International Manufacturing Science and Engineering Conference, MSEC 2016* vol. 1 1–10 (2016).
18. Yang, K. S., Kim, B. H. & Yoon, S. H. Pitch based carbon fibers for automotive body and electrodes. *Carbon Lett.* **15**, 162–170 (2014).
19. Choi, D., Kil, H. S. & Lee, S. Fabrication of low-cost carbon fibers using economical precursors and advanced processing technologies. *Carbon N. Y.* **142**, 610–649 (2019).
20. Alcañiz-Monge, J. *et al.* Preparation of general purpose carbon fibers from coal tar pitches with low softening point. *Carbon N. Y.* **35**, 1079–1087 (1997).
21. Park, S. H., Kim, C. & Yang, K. S. Preparation of carbonized fiber web from electrospinning of isotropic pitch. *Synth. Met.* **143**, 175–179 (2004).
22. Diefendorf, R. J. & Tokarskyo, E. High-performance carbon fibers. *Polym. Eng. Sci.* **15**, 150–159 (1975).

23. Huang, Y. & Young, R. J. Effect of fibre microstructure upon the modulus of PAN- and pitch-based carbon fibres. *Carbon N. Y.* **33**, 97–107 (1995).
24. Ko, S., Choi, J. E., Lee, C. W. & Jeon, Y. P. Preparation of petroleum-based mesophase pitch toward cost-competitive high-performance carbon fibers. *Carbon Lett.* **30**, 35–44 (2020).
25. Naito, K., Tanaka, Y., Yang, J. M. & Kagawa, Y. Tensile properties of ultrahigh strength PAN-based, ultrahigh modulus pitch-based and high ductility pitch-based carbon fibers. *Carbon N. Y.* **46**, 189–195 (2008).
26. Mainka, H. *et al.* Lignin–an alternative precursor for sustainable and cost-effective automotive carbon fiber. *J. Mater. Res. Technol.* **4**, 283–296 (2015).
27. Ku, H., Wang, H., Pattarachaiyakoop, N. & Trada, M. A review on the tensile properties of natural fiber reinforced polymer composites. *Compos. Part B Eng.* **42**, 856–873 (2011).
28. Luckachan, G. E. & Pillai, C. K. S. Biodegradable polymers-a review on recent trends and emerging perspectives. *J. Polym. Environ.* **19**, 637–676 (2011).
29. Sauder, C., Lamon, J. & Pailler, R. The tensile behavior of carbon fibers at high temperatures up to 2400°C. *Carbon N. Y.* **42**, 715–725 (2004).
30. Schalamon, W. A. & Bacon, R. Process for producing carbon fibers having a high young's modulus of elasticity. (1973).
31. Newcomb, B. A. Processing, structure, and properties of carbon fibers. *Compos. Part A Appl. Sci. Manuf.* **91**, 262–282 (2016).
32. Wu, Q. & Pan, D. A new cellulose based carbon fiber from a lyocell precursor. *Text. Res. J.* **72**, 405–410 (2002).
33. Fengel, D. & Wegener, G. *Wood: chemistry, ultrastructure, reactions*. (Walter de Gruyter, 1989).
34. Otani, S., Fukuoka, Y., Igarashi, B. & Sasaki, K. Method for producing carbonized lignin fiber. (1969).
35. Gellerstedt, G., Sjöholm, E. & Brodin, I. The wood-based biorefinery: A source of carbon fiber? *Open Agric. J.* **4**, 119–124 (2010).
36. Vishtal, A. G. & Kraslawski, A. Challenges in industrial applications of technical lignins. *BioResources* **6**, 3547–3568 (2011).
37. Nar, M. *et al.* Superior plant based carbon fibers from electrospun poly-(caffeyl alcohol) lignin. *Carbon N. Y.* **103**, 372–383 (2016).
38. Whetten, R. W., MacKay, J. J. & Sederoff, R. R. Recent advances in understanding lignin biosynthesis. *Annu. Rev. Plant Biol.* **49**, 585–609 (1998).
39. Popescu, C. M. *et al.* Analytical methods for lignin characterization. II. Spectroscopic studies. *Cellul. Chem. Technol.* **40**, 597–621 (2006).
40. Mahmood, N., Yuan, Z., Schmidt, J. & Xu, C. Depolymerization of lignins and their applications for the preparation of polyols and rigid polyurethane foams: A review. *Renew. Sustain. Energy Rev.* **60**, 317–329 (2016).
41. Watkins, D., Nuruddin, M., Hosur, M., Tcherbi-Narteh, A. & Jeelani, S. Extraction and characterization of lignin from different biomass resources. *J. Mater. Res. Technol.* **4**, 26–32 (2015).
42. Xu, F., Sun, J. X., Sun, R., Fowler, P. & Baird, M. S. Comparative study of organosolv lignins from wheat straw. *Ind. Crops Prod.* **23**, 180–193 (2006).
43. Lallave, M. *et al.* Filled and hollow carbon nanofibers by coaxial electrospinning of alcell lignin without binder polymers. *Adv. Mater.* **19**, 4292–4296 (2007).

44. Oroumei, A., Fox, B. & Naebe, M. Thermal and rheological characteristics of biobased carbon fiber precursor derived from low molecular weight organosolv lignin. *ACS Sustain. Chem. Eng.* **3**, 758–769 (2015).

45. Van Blaricom, L. E. & Russell, G. K. Lignosulfonate recovery from waste sulfite liquor. (1955).

46. Yen, S. H. & Chang, F. C. Effects of fiber processing conditions on the yield, carbon content, and diameter of lignosulfonate-based carbon fibers. *BioResources* **11**, 10158–10172 (2016).

47. Xia, K. *et al.* Preparation and characterization of lignosulfonate–acrylonitrile copolymer as a novel carbon fiber precursor. *ACS Sustain. Chem. Eng.* **4**, 159–168 (2016).

48. Sudo, K. & Shimizu, K. A new carbon fiber from lignin. *J. Appl. Polym. Sci.* **44**, 127–134 (1992).

49. Chen, H. & Liu, L. Unpolluted fractionation of wheat straw by steam explosion and ethanol extraction. *Bioresour. Technol.* **98**, 666–676 (2007).

50. Li, Y., Cui, D., Tong, Y. & Xu, L. Study on structure and thermal stability properties of lignin during thermostabilization and carbonization. *Int. J. Biol. Macromol.* **62**, 663–669 (2013).

51. Yi, X. *et al.* Graphene-like carbon sheet/Fe3O4 nanocomposites derived from soda papermaking black liquor for high performance lithium ion batteries. *Electrochim. Acta* **232**, 550–560 (2017).

52. Awal, A. & Sain, M. Characterization of soda hardwood lignin and the formation of lignin fibers by melt spinning. *J. Appl. Polym. Sci.* **129**, 2765–2771 (2013).

53. Zhang, R. *et al.* Unlocking the response of lignin structure for improved carbon fiber production and mechanical strength. *Green Chem.* **21**, 4981–4987 (2019).

54. Gellerstedt, G. Softwood kraft lignin: Raw material for the future. *Ind. Crops Prod.* **77**, 845–854 (2015).

55. Eckert, R. C. & Abdullah, Z. Carbon fibers from kraft softwood lignin. (2010).

56. Dong, D. & Fricke, A. L. Intrinsic viscosity and the molecular weight of kraft lignin. *Polymer (Guildf).* **36**, 2075–2078 (1995).

57. Dallmeyer, I., Chowdhury, S. & Kadla, J. F. Preparation and characterization of kraft lignin-based moisture-responsive films with reversible shape-change capability. *Biomacromolecules* **14**, 2354–2363 (2013).

58. Shi, X. *et al.* Impact of lignin extraction methods on microstructure and mechanical properties of lignin-based carbon fibers. *J. Appl. Polym. Sci.* **135**, (2018).

59. Johnson, D. J., Tomizuka, I. & Watanabe, O. The fine structure of lignin-based carbon fibres. **13**, 321–325 (1975).

60. Lundquist, K. Acid degradation of lignin. *Acta Chemica Scandinavica* vol. 27 2597–2606 (1973).

61. Toledano, A., García, A., Mondragon, I. & Labidi, J. Lignin separation and fractionation by ultrafiltration. *Sep. Purif. Technol.* **71**, 38–43 (2010).

62. Bozell, J. J. *et al.* Solvent fractionation of renewable woody feedstocks: Organosolv generation of biorefinery process streams for the production of biobased chemicals. *Biomass and bioenergy* **35**, 4197–4208 (2011).

63. Lara, M. A. *et al.* Black liquor lignin biodegradation by Trametes elegans. *Int. Biodeterior. Biodegrad.* **52**, 167–173 (2003).

64. García, A. *et al.* Characterization of lignins obtained by selective precipitation. *Sep. Purif.*

Technol. **68**, 193–198 (2009).

65. Zhu, W. & Theliander, H. Precipitation of lignin from softwood black liquor: an investigation of the equilibrium and molecular properties of lignin. *BioResources* **10**, 1696–1714 (2015).

66. Ghatak, H. R. Spectroscopic comparison of lignin separated by electrolysis and acid precipitation of wheat straw soda black liquor. *Ind. Crops Prod.* **28**, 206–212 (2008).

67. Nagy, M., Kosa, M., Theliander, H. & Ragauskas, A. J. Characterization of CO2 precipitated Kraft lignin to promote its utilization. *Green Chem.* **12**, 31–34 (2010).

68. van Spronsen, J., Cardoso, M. A. T., Witkamp, G. J., de Jong, W. & Kroon, M. C. Separation and recovery of the constituents from lignocellulosic biomass by using ionic liquids and acetic acid as co-solvents for mild hydrolysis. *Chem. Eng. Process. Process Intensif.* **50**, 196–199 (2011).

69. dos Santos, P. S. B., Erdocia, X., Gatto, D. A. & Labidi, J. Characterisation of Kraft lignin separated by gradient acid precipitation. *Ind. Crops Prod.* **55**, 149–154 (2014).

70. Gilarranz, M. A., Rodriguez, F., Oliet, M. & Revenga, J. A. Acid precipitation and purification of wheat straw lignin. *Sep. Sci. Technol.* **33**, 1359–1377 (1998).

71. Ziesig, R., Tomani, P. & Theliander, H. Production of a pure lignin product Part 2: Separation of lignin from membrane filtration permeates of black liquor. *Cellul. Chem. Technol.* **48**, 805–811 (2014).

72. Jönsson, A. S., Nordin, A. K. & Wallberg, O. Concentration and purification of lignin in hardwood kraft pulping liquor by ultrafiltration and nanofiltration. *Chem. Eng. Res. Des.* **86**, 1271–1280 (2008).

73. Asina, F. *et al.* Biodegradation of lignin by fungi, bacteria and laccases. *Bioresour. Technol.* **220**, 414–424 (2016).

74. Reid, I. D. Biodegradation of lignin. *Can. J. Bot.* **73**, 1011–1018 (1995).

75. Sun, R. C. & Tomkinson, J. Fractional separation and physico-chemical analysis of lignins from the black liquor of oil palm trunk fibre pulping. *Sep. Purif. Technol.* **24**, 529–539 (2001).

76. Li, Q. *et al.* Molecular weight and uniformity define the mechanical performance of lignin-based carbon fiber. *J. Mater. Chem. A* **5**, 12740–12746 (2017).

77. Tomani, P. The lignoboost process. *Cellul. Chem. Technol.* **44**, 53–58 (2010).

78. Kouisni, L., Holt-Hindle, P., Maki, K. & Paleologou, M. The LignoForce System™: A new process for the production of high-quality lignin from black liquor. *Pulp Pap. Canada* **115**, 18–22 (2014).

79. Maradur, S. P. *et al.* Preparation of carbon fibers from a lignin copolymer with polyacrylonitrile. *Synth. Met.* **162**, 453–459 (2012).

80. Zhang, M. & Ogale, A. A. Carbon fibers from dry-spinning of acetylated softwood kraft lignin. *Carbon N. Y.* **69**, 626–629 (2014).

81. Chen, P., Kim, H. S., Kwon, S. M., Yun, Y. S. & Jin, H. J. Regenerated bacterial cellulose/multi-walled carbon nanotubes composite fibers prepared by wet-spinning. *Curr. Appl. Phys.* **9**, e96–e99 (2009).

82. Norberg, I., Nordström, Y., Drougge, R., Gellerstedt, G. & Sjöholm, E. A new method for stabilizing softwood kraft lignin fibers for carbon fiber production. *J. Appl. Polym. Sci.* **128**, 3824–3830 (2013).

83. Ruiz-Rosas, R. *et al.* The production of submicron diameter carbon fibers by the electrospinning of lignin. *Carbon N. Y.* **48**, 696–705 (2010).

84. Ding, R., Wu, H., Thunga, M., Bowler, N. & Kessler, M. R. Processing and characterization of low-cost electrospun carbon fibers from organosolv lignin/polyacrylonitrile blends. *Carbon N. Y.* **100**, 126–136 (2016).

85. Dallmeyer, I., Lin, L. T., Li, Y., Ko, F. & Kadla, J. F. Preparation and Characterization of Interconnected, Kraft Lignin-B ased Carbon Fibrous Materials by Electrospinning. *Macromol. Mater. Eng.* **299**, 540–551 (2014).

86. Brazinsky, I., Williams, A. G. & LaNieve, H. L. The dry spinning process: Comparison of theory with experiment. *Polym. Eng. Sci.* **15**, 834–841 (1975).

87. Zhang, M. & Ogale, A. A. Effect of temperature and concentration of acetylated-lignin solutions on dry-spinning of carbon fiber precursors. *J. Appl. Polym. Sci.* **133**, (2016).

88. Jin, J. & Ogale, A. A. Carbon fibers derived from wet-spinning of equi-component lignin/polyacrylonitrile blends. *J. Appl. Polym. Sci.* **135**, 1–9 (2018).

89. Jia, Z., Lu, C., Liu, Y., Zhou, P. & Wang, L. Lignin/polyacrylonitrile composite hollow fibers prepared by wet-spinning method. *ACS Sustain. Chem. Eng.* **4**, 2838–2842 (2016).

90. Tan, L., Chen, H., Pan, D. & Pan, N. Investigating the spinnability in the dry-jet wet spinning of PAN precursor fiber. *J. Appl. Polym. Sci.* **110**, 1997–2000 (2008).

91. Olsson, C., Sjöholm, E. & Reimann, A. Carbon fibres from precursors produced by dry-jet wet-spinning of kraft lignin blended with kraft pulps. *Holzforschung* **71**, 275–283 (2017).

92. Baker, D. A., Gallego, N. C. & Baker, F. S. On the characterization and spinning of an organic-purified lignin toward the manufacture of low-cost carbon fiber. *J. Appl. Polym. Sci.* **124**, 227–234 (2012).

93. Reneker, D. H. & Yarin, A. L. Electrospinning jets and polymer nanofibers. *Polymer (Guildf).* **49**, 2387–2425 (2008).

94. Baji, A., Mai, Y. W., Wong, S. C., Abtahi, M. & Chen, P. Electrospinning of polymer nanofibers: effects on oriented morphology, structures and tensile properties. *Compos. Sci. Technol.* **70**, 703–718 (2010).

95. Teng, N. Y., Dallmeyer, I. & Kadla, J. F. Incorporation of multiwalled carbon nanotubes into electrospun softwood Kraft lignin-based fibers. *J. Wood Chem. Technol.* **33**, 299–316 (2013).

96. Yang, C., Jia, Z., Guan, Z. & Wang, L. Polyvinylidene fluoride membrane by novel electrospinning system for separator of Li-ion batteries. *J. Power Sources* **189**, 716–720 (2009).

97. Su, C. *et al.* Fabrication of a novel nanofibers-covered hollow fiber membrane via continuous electrospinning with non-rotational collectors. *Mater. Lett.* **204**, 8–11 (2017).

98. Dabirian, F. & Hosseini, S. A. Novel method for nanofibre yarn production using two differently charged nozzles. *Fibres Text. East. Eur.* **74**, 45–47 (2009).

99. Katta, P., Alessandro, M., Ramsier, R. D. & Chase, G. G. Continuous electrospinning of aligned polymer nanofibers onto a wire drum collector. *Nano Lett.* **4**, 2215–2218 (2004).

100. Kishan, A. P. *et al.* Fabrication of macromolecular gradients in aligned fiber scaffolds using a combination of in-line blending and air-gap electrospinning. *Acta Biomater.* **56**, 118–128 (2017).

101. Lee, H., Yoon, H. & Kim, G. Highly oriented electrospun polycaprolactone micro/nanofibers prepared by a field-controllable electrode and rotating collector. *Appl. Phys. A Mater. Sci. Process.* **97**, 559–565 (2009).

102. Thomas, V. *et al.* Mechano-morphological studies of aligned nanofibrous scaffolds of polycaprolactone fabricated by electrospinning. *J. Biomater. Sci. Polym. Ed.* **17**, 969–984

(2006).

103. Pan, H., Li, L., Hu, L. & Cui, X. Continuous aligned polymer fibers produced by a modified electrospinning method. *Polymer (Guildf).* **47**, 4901–4904 (2006).

104. Theron, A., Zussman, E. & Yarin, A. L. Electrostatic field-assisted alignment of electrospun nanofibres. *Nanotechnology* **12**, 384–390 (2001).

105. Shuakat, M. N. & Lin, T. Direct electrospinning of nanofibre yarns using a rotating ring collector. *J. Text. Inst.* **107**, 791–799 (2016).

106. Heidari, I., Mashhadi, M. M. & Faraji, G. A novel approach for preparation of aligned electrospun polyacrylonitrile nanofibers. *Chem. Phys. Lett.* **590**, 231–234 (2013).

107. Zernetsch, H. *et al.* Electrospinning and mechanical properties of polymeric fibers using a novel gap-spinning collector. *Fibers Polym.* **17**, 1025–1032 (2016).

108. Wu, Y., Carnell, L. A. & Clark, R. L. Control of electrospun mat width through the use of parallel auxiliary electrodes. *Polymer (Guildf).* **48**, 5653–5661 (2007).

109. Yang, D., Lu, B., Zhao, Y. & Jiang, X. Fabrication of aligned fibrous arrays by magnetic electrospinning. *Adv. Mater.* **19**, 3702–3706 (2007).

110. Kim, J. I., Kim, J. Y. & Park, C. H. Fabrication of transparent hemispherical 3D nanofibrous scaffolds with radially aligned patterns via a novel electrospinning method. *Sci. Rep.* **8**, 1–13 (2018).

111. Tong, H. W. & Wang, M. A novel technique for the fabrication of 3D nanofibrous scaffolds using simultaneous positive voltage electrospinning and negative voltage electrospinning. *Mater. Lett.* **94**, 116–120 (2013).

112. Mi, S. *et al.* A novel electrospinning setup for the fabrication of thickness-controllable 3D scaffolds with an ordered nanofibrous structure. *Mater. Lett.* **160**, 343–346 (2015).

113. Liu, Y., He, J. H. & Yu, J. Y. Bubble-electrospinning: A novel method for making nanofibers. *J. Phys. Conf. Ser.* **96**, (2008).

114. Varesano, A., Carletto, R. A. & Mazzuchetti, G. Experimental investigations on the multi-jet electrospinning process. *J. Mater. Process. Technol.* **209**, 5178–5185 (2009).

115. Tang, S., Zeng, Y. & Wang, X. Splashing needleless electrospinning of nanofibers. *Polym. Eng. Sci.* **50**, 2252–2257 (2010).

116. Zuo, W. *et al.* Experimental study on relationship between jet instability and formation of beaded fibers during electrospinning. *Polym. Eng. Sci.* **45**, 704–709 (2005).

117. Liu, Y. Q., He, C. H., Li, X. X. & He, J. H. Fabrication of beltlike fibers by electrospinning. *Polymers (Basel).* **10**, 1–9 (2018).

118. Fong, H., Chun, I. & Reneker, D. H. Beaded nanofibers formed during electrospinning. **40**, 4585–4592 (1999).

119. Koombhongse, S., Liu, W. & Reneker, D. H. Flat polymer ribbons and other shapes by electrospinning. *J. Polym. Sci. Part B Polym. Phys.* **39**, 2598–2606 (2001).

120. Kadla, J. F. *et al.* Lignin-based carbon fibers for composite fiber applications. *Carbon N. Y.* **40**, 2913–2920 (2002).

121. Mit-Uppatham, C., Nithitanakul, M. & Supaphol, P. Ultrafine electrospun polyamide-6 fibers: Effect of solution conditions on morphology and average fiber diameter. *Macromol. Chem. Phys.* **205**, 2327–2338 (2004).

122. Zhang, C., Yuan, X., Wu, L., Han, Y. & Sheng, J. Study on morphology of electrospun poly(vinyl alcohol) mats. *Eur. Polym. J.* **41**, 423–432 (2005).

123. Rutledge, G. C. & Fridrikh, S. V. Formation of fibers by electrospinning. *Adv. Drug Deliv. Rev.* **59**, 1384–1391 (2007).

124. Yuan, X. Y., Zhang, Y. Y., Dong, C. & Sheng, J. Morphology of ultrafine polysulfone fibers prepared by electrospinning. *Polym. Int.* **53**, 1704–1710 (2004).
125. Kong, L. & Ziegler, G. R. Quantitative relationship between electrospinning parameters and starch fiber diameter. *Carbohydr. Polym.* **92**, 1416–1422 (2013).
126. Heikkilä, P. & Harlin, A. Parameter study of electrospinning of polyamide-6. *Eur. Polym. J.* **44**, 3067–3079 (2008).
127. Deitzel, J. M., Kleinmeyer, J., Harris, D. E. A. & Tan, N. C. B. The effect of processing variables on the morphology of electrospun nanofibers and textiles. *Polymer (Guildf).* **42**, 261–272 (2001).
128. Kilic, A., Oruc, F. & Demir, A. Effects of polarity on electrospinning process. *Text. Res. J.* **78**, 532–539 (2008).
129. De Vrieze, S. *et al.* The effect of temperature and humidity on electrospinning. *J. Mater. Sci.* **44**, 1357 (2009).
130. Zargham, S., Bazgir, S., Tavakoli, A., Rashidi, A. S. & Damerchely, R. The effect of flow rate on morphology and deposition area of electrospun nylon 6 nanofiber. *J. Eng. Fabr. Fibers* **7**, (2012).
131. Dallmeyer, I., Ko, F. & Kadla, J. F. Correlation of elongational fluid properties to fiber diameter in electrospinning of softwood kraft lignin solutions. *Ind. Eng. Chem. Res.* **53**, 2697–2705 (2014).
132. Rodd, L. E., Scott, T. P., Cooper-White, J. J. & McKinley, G. H. Capillary break-up rheometry of low-viscosity elastic fluids. *Appl. Rheol.* **15**, 12–27 (2005).
133. Aslanzadeh, S. *et al.* Electrospinning of colloidal lignin in poly(ethylene oxide) N, N-dimethylformamide solutions. *Macromol. Mater. Eng.* **301**, 401–413 (2016).
134. Luo, C. J., Stride, E. & Edirisinghe, M. Mapping the influence of solubility and dielectric constant on electrospinning polycaprolactone solutions. *Macromolecules* **45**, 4669–4680 (2012).
135. Braun, J. L., Holtman, K. M. & Kadla, J. F. Lignin-based carbon fibers: Oxidative thermostabilization of kraft lignin. *Carbon N. Y.* **43**, 385–394 (2005).
136. Cho, M., Karaaslan, M. A., Renneckar, S. & Ko, F. Enhancement of the mechanical properties of electrospun lignin-based nanofibers by heat treatment. *J. Mater. Sci.* **52**, 9602–9614 (2017).
137. Cho, M., Karaaslan, M., Chowdhury, S., Ko, F. & Renneckar, S. Skipping oxidative thermal stabilization for lignin-based carbon nanofibers. *ACS Sustain. Chem. Eng.* **6**, 6434–6444 (2018).
138. Cao, J., Xiao, G., Xu, X., Shen, D. & Jin, B. Study on carbonization of lignin by TG-FTIR and high-temperature carbonization reactor. *Fuel Process. Technol.* **106**, 41–47 (2013).
139. Aslanzadeh, S., Ahvazi, B., Boluk, Y. & Ayranci, C. Carbon fiber production from electrospun sulfur free softwood lignin precursors. *J. Eng. Fabr. Fibers* **12**, (2017).
140. Kim, H. H., Kim, M. J., Ryu, S. J., Ki, C. S. & Park, Y. H. Effect of fiber diameter on surface morphology, mechanical property, and cell behavior of electrospun poly(ε-caprolactone) mat. *Fibers Polym.* **17**, 1033–1042 (2016).
141. Wang, S. X., Yang, L., Stubbs, L. P., Li, X. & He, C. Lignin-derived fused electrospun carbon fibrous mats as high performance anode materials for lithium ion batteries. *ACS Appl. Mater. Interfaces* **5**, 12275–12282 (2013).
142. Dallmeyer, I., Ko, F. & Kadla, J. F. Electrospinning of technical lignins for the production of fibrous networks. *J. Wood Chem. Technol.* **30**, 315–329 (2010).

143. Youe, W. J., Lee, S. M., Lee, S. S., Lee, S. H. & Kim, Y. S. Characterization of carbon nanofiber mats produced from electrospun lignin-g-polyacrylonitrile copolymer. *Int. J. Biol. Macromol.* **82**, 497–504 (2016).

144. Lai, C. *et al.* Free-standing and mechanically flexible mats consisting of electrospun carbon nanofibers made from a natural product of alkali lignin as binder-free electrodes for high-performance supercapacitors. *J. Power Sources* **247**, 134–141 (2014).

145. Paterakis, P. G., Korakianiti, E. S., Dallas, P. P. & Rekkas, D. M. Evaluation and simultaneous optimization of some pellets characteristics using a 33 factorial design and the desirability function. *Int. J. Pharm.* **248**, 51–60 (2002).

146. Rakić, T., Kasagić-Vujanović, I., Jovanović, M., Jančić-Stojanović, B. & Ivanović, D. Comparison of full factorial design, central composite design, and box-behnken design in chromatographic method development for the determination of fluconazole and its impurities. *Anal. Lett.* **47**, 1334–1347 (2014).

147. Bezerra, M. A., Santelli, R. E., Oliveira, E. P., Villar, L. S. & Escaleira, L. A. Response surface methodology (RSM) as a tool for optimization in analytical chemistry. *Talanta* **76**, 965–977 (2008).

148. Ferreira, S. L. C. *et al.* Box-Behnken design: An alternative for the optimization of analytical methods. *Anal. Chim. Acta* **597**, 179–186 (2007).

149. Ghosh, T., Ngo, T.-D., Kumar, A., Ayranci, C. & Tang, T. Cleaning carbohydrate impurities from lignin using Pseudomonas fluorescens. *Green Chem.* **21**, 1648–1659 (2019).

150. Ding, R., Wu, H., Thunga, M., Bowler, N. & Kessler, M. R. Processing and characterization of low-cost electrospun carbon fibers from organosolv lignin/polyacrylonitrile blends. *Carbon N. Y.* **100**, 126–136 (2016).

151. Hotaling, N. A., Bharti, K., Kriel, H. & Simon, C. G. DiameterJ: A validated open source nanofiber diameter measurement tool. *Biomaterials* **61**, 327–338 (2015).

152. Aslanzadeh, S., Ahvazi, B., Boluk, Y. & Ayranci, C. Morphologies of electrospun fibers of lignin in poly(ethylene oxide)/N, N-dimethylformamide. *J. Appl. Polym. Sci.* **133**, (2016).

153. Myers, R. H., Montgomery, D. C. & Anderson-Cook, C. M. *Response surface methodology: process and product optimization using designed experiments*. (John Wiley & Sons, 2016).

154. Megelski, S., Stephens, J. S., Chase, D. B. & Rabolt, J. F. Micro-and nanostructured surface morphology on electrospun polymer fibers. *Macromolecules* **35**, 8456–8466 (2002).

155. Baumgarten, P. K. Electrostatic spinning of acrylic microfibers. *J. Colloid Interface Sci.* **36**, 71–79 (1971).

156. Inagaki, M., Yang, Y. & Kang, F. Carbon nanofibers prepared via electrospinning. *Adv. Mater.* **24**, 2547–2566 (2012).

157. Fridrikh, S. V, Jian, H. Y., Brenner, M. P. & Rutledge, G. C. Controlling the fiber diameter during electrospinning. *Phys. Rev. Lett.* **90**, 144502 (2003).

158. Zhu, M., Zuo, W., Yu, H., Yang, W. & Chen, Y. Superhydrophobic surface directly created by electrospinning based on hydrophilic material. *J. Mater. Sci.* **41**, 3793–3797 (2006).

159. Wong, S. C., Baji, A. & Leng, S. Effect of fiber diameter on tensile properties of electrospun poly(ε-caprolactone). *Polymer (Guildf).* **49**, 4713–4722 (2008).

160. Kai, D., Jiang, S., Low, Z. W. & Loh, X. J. Engineering highly stretchable lignin-based electrospun nanofibers for potential biomedical applications. *J. Mater. Chem. B* **3**, 6194–

6204 (2015).